STRUCTURAL AND STRATIGRAPHIC CONTROLS ON MESAVERDE RESERVOIR PERFORMANCE: RULISON FIELD, GARFIELD COUNTY, COLORADO

by

Marin Matesic

A thesis submitted to the Faculty and the Board of Trustees of the Colorado School of Mines in partial fulfillment of the requirement for the degree of Master of Science (Geology)

Golden, Colorado

Date 1/24/07

Signed: _____

Marin Matesic

Approved: _____

Dr. Neil F. Hurley

Thesis Advisor

Golden, Colorado

Date 1/24/07

_____

Dr. John D. Humphrey

Acting Department Head

Department of Geology and

Geological Engineering

ABSTRACT

Rulison field in the Piceance basin is a continuous gas accumulation. The field produces gas from low-permeability (microdarcy range) sandstones of the Mesaverde Group. Three image logs (RWF 542-20, RWF 523-20, RMV 60-17) were used to characterize structural and stratigraphic features in fluvial sandstones and shales of the lower Williams Fork Formation. Faults and fractures are one of the main controls on production in tight-gas sandstone reservoirs like Rulison. In order to optimize future development of the field, it was important to describe and understand the location of the faulted and intensively fractured zones.

Maximum present-day horizontal stress (SHmax) has been determined from the analysis of borehole breakouts in caliper logs and compared with interpretations in the image logs. Analyses indicate that the regional SHmax orientation is N70^{o}W, with local variations.

Drilling induced fractures have the same orientation (N70^{o}W) as natural open fractures. The open natural fractures are solely developed in the sandstones and this was the main criterion for their recognition. The dip of the open fractures averages 75^{o}.

Two sets of resistive fractures are oriented N30^{o}W and N60^{o}E. The third, least numerous set of resistive fractures is parallel to the orientation of SHmax, suggesting that

it was created in the same stress regime as the drilling induced or natural open fractures. Average dip of resistive fractures is 35^{o}.

Most of the imaged intervals in 2 out of 3 wells show the presence of gas seeps. There was no definitive relationship observed between faults, fractures, sandstone beds, and gas seeps. Higher mud weights in one well correspond to reduced gas-seep density. The quantity of gas seeps is a function of mud weight. Gas-seep interpretation must be approached with caution and used as a qualitative indicator of gas presence.

Two fault zones and 18 faults were interpreted in both dip-domain analyses and borehole image logs for wells RWF 542-20, RWF 523-20 and RMV 60-17. Two sets of resistive fractures parallel the strike of the faults interpreted. This suggests that faulted zones of enhanced permeability are accompanied by fractures of the same orientation. All of the orientations of structural elements such as stress, fractures, and faults show a good match with a left-lateral kinematic model. Faults and two sets of resistive fractures could be explained as Riedel conjugate-shear fractures.

In the vicinity of the RWF 542-20 well, there is a fault interpreted in seismic data. A succession of similarity (coherency) depth slices shows that the fault has a strike of $N30^{o}W$ and is nearly vertical. A vertical profile through the slow-shear (S22) similarity volume through the RWF 542-20 well shows anomalies at the locations of the faults picked in the image log. This might be an indicator of a structurally altered zone or a zone of enhanced permeability. The seismic-scale fault is not visible in the image log.

Only the strikes and dips of structural features on different scales of investigation are comparable.

The best wells, in terms of estimated ultimate recovery, are regularly spaced away from the seismic-interpreted fault (approximately 600 ft, 200 m). The wells located directly on top of the fault have relatively lower production because of two possible reasons. First, wells might penetrate relatively small reservoir compartments, which were quickly drained of gas. Second, the zones might have excessive permeability, which causes partial leakage of gas and relatively poor gas production.

TABLE OF CONTENTS

LIST OF FIGURES

LIST OF TABLES

ACKNOWLEDGMENTS

The completion of any graduate degree program represents an accomplishment of the candidate and the support of many people. I sincerely express my appreciation to various people and organizations.

I gratefully thank my advisor, Dr. Neil F. Hurley, for his superior guidance, appropriate suggestions, and generous contribution of time. I offer sincere thanks to my other committee members Dr. Thomas L. Davis and Dr. John B. Curtis. I acknowledge each individual as a master in his field, and express my appreciation for their valuable suggestions.

This project would not have been possible without financial support in the form of student grants and scholarships from the following organizations: Reservoir Characterization Project (RCP) at the Colorado School of Mines (CSM), Geology and Geological Engineering Department at CSM, ConocoPhillips SPIRIT Scholars Program, the Center for Petrophysics (CENPET) at CSM, Harry C. Kent Scholarship, and the Society of Independent Professional Earth Scientists (SIPES) Foundation.

I gratefully acknowledge Janine Carlson for helping me with the workstation. I would like to thank Charlie Rourke, who was always there to help in administration, thesis work, and so many other things. I am indebted to Lesley Evans for data support

and suggestions. A special note of thanks goes to Jerry Cuzella for showing me the outcrops at Coal Canyon, Colorado. I benefited greatly from discussions with Jim Emme, Roger Reinmiller, Herman Homann and Robert Weimer regarding this project and would like to thank them for their time. I am grateful to the Colorado School of Mines (CSM) professors, staff and students. I appreciate fellow Reservoir Characterization Project (RCP) members for their constructive comments and useful suggestions.

My experience at CSM was made more enjoyable by the support of my friends gained during my graduate study. Hopefully, our friendship will continue in the future.

Last but not least, I would like to express my gratitude for the constant source of encouragement from my family and friends back home in Croatia, and Bay of Kotor, Montenegro.

For my parents.

CHAPTER 1

INTRODUCTION

Rulison field in the Piceance basin is a continuous gas accumulation. The field produces gas from low-permeability (microdarcy range) sandstones of the Mesaverde Group. Recent estimates suggest that the Piceance basin contains between 20 and 40 TCF of gas in place (USGS, 2003; Potential Gas Committee, 2003). The unit of interest in this study is the Williams Fork Formation, which formed in a coastal and fluvial floodplain environment. The Williams Fork is underlain by the Iles Formation and overlain by the Ohio Creek Member of the Mesaverde Group, and represents part of a shoreline progradational sequence. The Williams Fork Formation is characterized principally as a meandering fluvial system, where most of the sand bodies were deposited as point bars and overbank deposits during the lateral migration of rivers.

The point bar units are stacked and form composite meander-belt sandstone reservoirs. The main gas-bearing zone includes stacked sandstone bodies that are highly lenticular with typical lateral extents of 500-800 ft (152-244 m) (Cumella and Ostby, 2003) and very low-permeability that ranges from 5 to 80 μD. In addition, internal permeability barriers such as accretionary bedding and scour surfaces are present (Cumella and Ostby, 2003). Well-to-well correlation of such sand bodies does not yield

definitive results, and connectivity is questionable due to the existence of 60 or more reservoirs (point bars) per well. Conventional P-wave seismic data are not able to locate individual channel sands.

Besides facies control, there is a structural component of production. The fault and fracture system has been documented to have a major role in migration of gas from the deeper part of the basin (Cumella 2006; Jansen 2005). Sandstones within the Mesaverde are extensively fractured, solely in the sandstone and siltstone lithologies. Fractures terminate at the lithologic boundaries (shales), with no continuity of reservoirs (Lorenz, 2003). Subtle fracture networks exist in sandstones that control gas migration and typically correspond to good well performance. Different types of structural features (e.g., fractures, borehole breakouts, faults) and stratigraphic features (e.g., base of gas seeps) are observed in the image logs.

1.1. Research Objectives

There are three main objectives in this study:

(1) Interpret structural elements from borehole image and caliper logs. Determine the present-day stress orientation from borehole breakouts. Quantitatively describe fractures and faults which are generally of a sub-seismic scale.

(2) Interpret the base of gas seeps to help determine qualitatively more productive intervals. Explore the origin of the gas production in the well and its relation to the stratigraphic and structural features.

(3) Integrate those results with seismic data to help resolve complex reservoir issues at the Rulison field.

1.2. Study Area and Data Set

The study area is located at the Rulison field in the Piceance basin in northwest Colorado. The basin, one of the major Rocky mountain foreland basins, covers an area of 18,700 km^2 (7,255 mi^2) (Figure 1.1). The basin trends northwest-southeast and is approximately 160 km (100 mi) long and 64 to 80 km (40 to 50 mi) wide (Spencer, 1989). On the western margin of the basin, the Douglas Creek Uplift separates it from the geologically similar Uinta basin. The Rulison field is located in southern portion of the Piceance basin, close to Grand Valley, Parachute and Mamm Creek natural gas fields.

Interpretation of 3 borehole image logs is central to the study. All three imaged wells are located inside the Reservoir Characterization Project area shown in Figure 1.2 (FMI wells: RMV 60-17, RWF 523-20, EMI well: RWF 542-20). An additional log (EMI well RWF 441-20) will be included in this research, using the reports of the

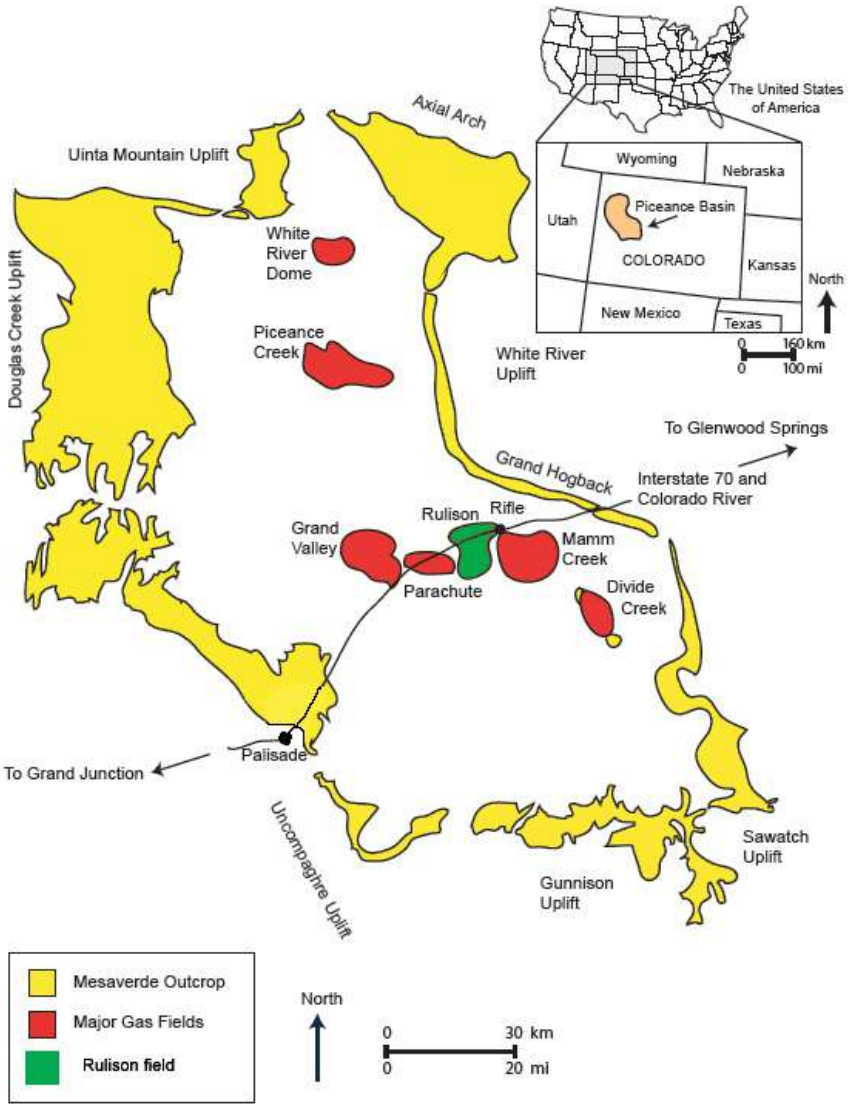

Figure 1.1. The study area is located at the Rulison field in the Piceance basin in northwest Colorado. Major gas fields produce from the Williams Fork Formation of the Mesaverde Group. Modified from Hoak and Klawitter (1997).

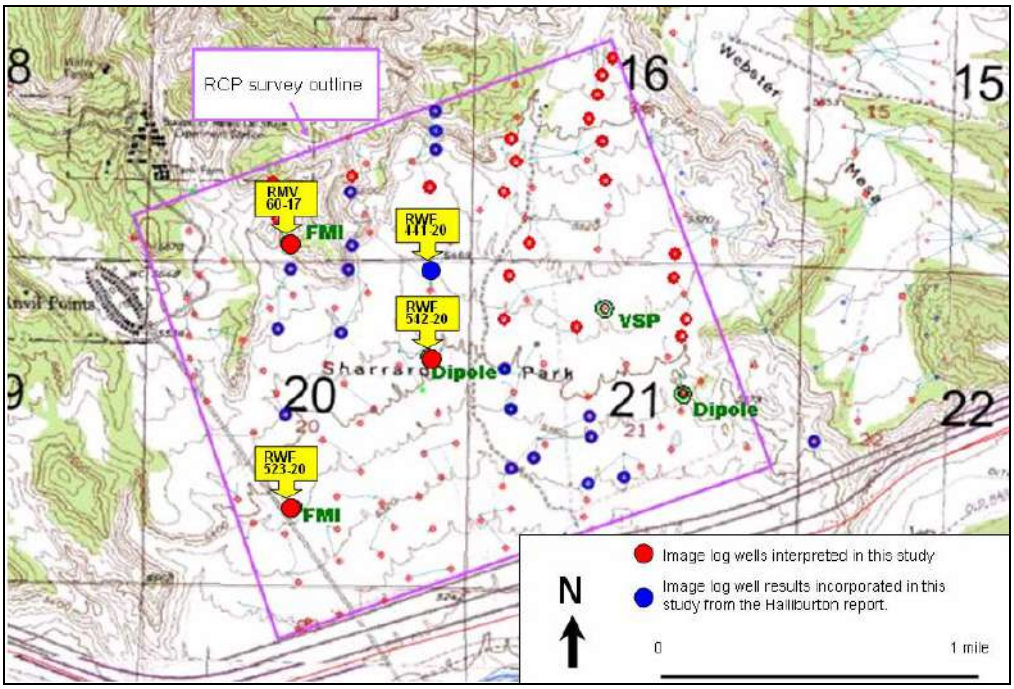

Figure 1.2. Location map of image log wells (RWF 542-20, RWF 523-20, RMV 60-17 and RWF 441-20) in Rulison field. These wells occur in T6S-R94W. Wells are located inside the Reservoir Characterization Project (RCP) survey.

interpretation from Halliburton Company. The imaged interval for well RWF 542-20 spans from 4000 to 8000 ft measured depth. The imaged interval for well RWF 523-20 spans from 5500 to 8000 ft measured depth. Finally, the imaged interval for well RMV 60-17 spans from 5500 to 8000 ft measured depth. All of the imaged intervals targeted the main productive interval in Lower Williams Fork Formation.

The image logs have been loaded into a Silicon Graphics workstation with Review/ Recall interpretation software.

1.3. Previous Work

There have been numerous publications about regional stratigraphy in the Piceance basin, such as Johnson et al. (1986 and 1989), Hettinger and Kirschbaumm (2004), Patterson et al. (2003), Lorenz (1985), and others.

Studies that put emphasis on the structural component in the same region were written by Cumella and Ostby (2003), Koepsell et al. (2003), Lorenz (2003), and Gomez et al. (2003).

Cumella and Ostby (2003) used 3D seismic data to interpret a series of faults in the Rulison area. They indicated left-lateral transpressional structural style. The first set of faults showed a northwest trend (N45^{o}W), near-vertical dip, and left-lateral slip. The

second set, with a north-northwest trend (N20^{o}W), had dips of 30 to 60 degrees, and showed reverse character.

Koepsell et al. (2003) described a method of characterizing image logs in the Piceance basin. Their study showed that the Iles and Williams Fork Formations have enhanced productivity with the presence of the natural fracturing. Maximum principal stress orientation varies from ENE to ESE.

Lorenz (2003) found that fractures strike between WNW-ESE and WSW-ENE in the Piceance basin. Fracture systems were labeled as the most promising targets for gas production, although they also introduce potential water problems.

Gomez et al. (2003) quantified fracture intensity in the Piceance basin using five microfracture data sets from 117 ft (35 m) of subhorizontal Cretaceous Cozzete Sandstone core from the Slant Hole Completion Test well, which was drilled as part of a U.S. Department of Energy project to evaluate tight gas sandstones in the Piceance basin. The authors noticed that subsidiary northwestward and northeastward fracture strike trends were also present.

The Rulison gas field is the present object of research of the Reservoir Characterization Project (RCP, phases X and XI) at the Colorado School of Mines, Golden, Colorado. The majority of the most recent work has been done by the members of the research group of phase X and XI: Rojas (2005), Kusuma (2005), Jansen (2005), Higgins (2006), Green (2006), Keighley (2006), and Rumon (2006).

Jansen (2005) analyzed P and S wave seismic data to identify and delineate fault and fracture zones in the Rulison survey area. He suggested that wrench faulting occurred in the field as a result of strike-slip deformation.

Higgins (2006) related stress, strength and pressure to create a geomechanical model in the Rulison field. She estimated rock strength from logs at Rulison field.

Several other students have been working in the same area. Ellison (2004) modeled heterogeneities within a fluvial point-bar deposit using outcrop and LIDAR data in the Williams Fork Formation. Her flow simulation showed that heterogeneity caused various fluid-flow anomalies. Vargas (2004) characterized fluvial sandstones and modeled their static connectivity.

Panjaitan (2006) described the sand-body dimensions in outcrop and subsurface in the Lower Williams Fork Formation. He observed different types of fluvial sand bodies (e.g. point bars and crevasse splays) without describing the structural elements like fractures and faults.

This study is a logical continuation of research in the RCP area, which targets the structural component of the sand bodies and is complementary to previous work focused on stratigraphic descriptions.

1. 4. Research Contributions

- The present-day in situ stress orientation (SHmax) determined from borehole breakouts and drilling induced fractures at Rulison field is N70^{o}W with local variations.
- Drilling induced fractures have the same orientation as natural open fractures. The dip of the open fractures averages about 75^{o}. The open natural fractures are solely developed in the sandstones, and this was the main criteria used for their recognition.
- Two sets of resistive fractures are oriented N30^{o}W and N60^{o}E. The third, least numerous set of resistive fractures, shows the orientation of SHmax. This suggests that it was created in the same stress regime as the drilling induced or natural open fractures. Average dip of resistive fractures is 35^{o}.
- Most of the imaged intervals in 2 out of 3 wells show the presence of gas seeps. There was no definitive relationship between faults, fractures, sandstone beds, and gas seeps. Higher mud weights in one well correspond to reduced gas-seep density. The quantity of gas seeps is a function of mud weight. Gas-seep interpretation must be approached with caution, and used as a qualitative indicator of gas presence.
- Two fault zones and 18 faults were interpreted in both dip-domain analyses and image logs for wells RWF 542-20, RWF 523-20 and RMV 60-17. Two sets of

resistive fractures are oriented parallel to the strike of the faults interpreted. This suggests that faulted zones of enhanced permeability are accompanied by fractures of the same orientation. All of the orientations of the structural elements such as stress, fractures, and faults show a good match with a left-lateral kinematic model. Faults and two sets of resistive fractures could be explained as Riedel conjugate-shear fractures.

- In the vicinity of the RWF 542-20 well, there is a fault interpreted in the seismic data. A succession of depth slices used in the interpretation starts 946 ft below the Cameo horizon encountered in the RWF 542-20 well, and ends 150 ft above the mentioned horizon. The fault has a strike of N30^{o}W and is nearly vertical. The vertical slow-shear (S22) similarity volume through the RWF 542-20 well shows anomalies at the locations of the faults picked in the image log. This might be an indicator of a structurally altered zone or a zone of enhanced permeability. The seismic-scale fault is not visible in the image log. Only the strikes and dips of structural features on different scales of investigation are comparable.
- The best wells, in terms of estimated ultimate recovery (EUR), are regularly spaced away from the seismic-interpreted fault (approximately 600 ft, 200m). The wells located directly on top of the fault have relatively lower production because of two possible reasons. First, wells might penetrate relatively small reservoir compartments which quickly drained the gas. Second, the zones might have excessive permeability, which causes partial leakage of gas and relatively inferior

gas production. Furthermore, the RMV 60-17 and RWF 542-20 wells, as the relatively better producers of the image-log wells, show two sets of resistive fractures striking 65^{o} and 340^{o}, respectively. The RWF 523-20 well has the lowest EUR, absence of gas seeps, 2 fault zones, and just one resistive fracture interpreted.

CHAPTER 2

GEOLOGIC BACKGROUND

The Piceance basin is an example of a Rocky Mountain foreland basin. Natural gas is produced mainly from Cretaceous sandstones. This discussion of the geologic setting of the basin has been modified from previous work by Ellison (2004), Vargas (2004), and Panjaitan (2006).

2.1. Stratigraphy

During the Sevier Orogeny, the late Cretaceous Rocky Mountain foreland basin was flooded by marine waters to form the Western Interior Seaway. Sediments from the Sevier Orogeny were deposited on alluvial fans, and graded progressively into braid-plain, coastal-plain, deltaic, shoreline, and offshore environments within the Mesaverde Group (Johnson, 1989; Yurewicz et al., 2003). The Mesaverde Group represents the final regressive period of the Western Interior Seaway.

The basal members of the upper Cretaceous Mesaverde Group are the Castlegate, Sego, and Iles Formations. In the southern Piceance basin, the Iles Formation shows a

complex intertonguing with the marine Mancos Shale (Hettinger and Kirschbaum, 2002). The Iles Formation is subdivided into the Corcoran, Cozzette, and Rollins Sandstone members (Figure 2.1), which were deposited in inner-shelf, deltaic and lower coastal-plain settings (Cole and Cumella, 2003). Overlying the Rollins Sandstone, there is a coal-bearing interval known as the Cameo-Wheeler Zone. This forms the lower part of the Williams Fork Formation and was deposited in a coastal-plain setting by meandering streams in a fluvial environment (Johnson, 1986).

The Williams Fork Formation has an average thickness between 1,100 and 1,600 m (3,600 and 5,155 ft), thinning to the west to about 360 m (1,200 ft). The thinning has been attributed to regional Laramide erosion of the overlying intervals, including the Ohio Creek Conglomerate (Patterson et al., 2003) and the Wasatch Formation (Hettinger and Kirschbaum, 2002). In addition, thinning has been attributed to variation in subsidence rate across the basin (Hettinger and Kirschbaum, 2002).

In the southwestern part of the Piceance basin, the Williams Fork is subdivided into informal members based on lithology differences. The lower third of the Williams Fork is a low net-to-gross interval with approximately 30 to 60% sandstone, which dominantly consists of mudrock and coal. It is known as the sand–poor interval. The upper portion has a net-to-gross ratio between 50 to 80%, with subordinate mudrock and no coal, and is known as the sand-rich interval (Cole and Cumella, 2003).

The Wasatch Formation, which overlies the Mesaverde Group, was deposited in a fluvial environment. Laramide tectonics caused the regional unconformity, which

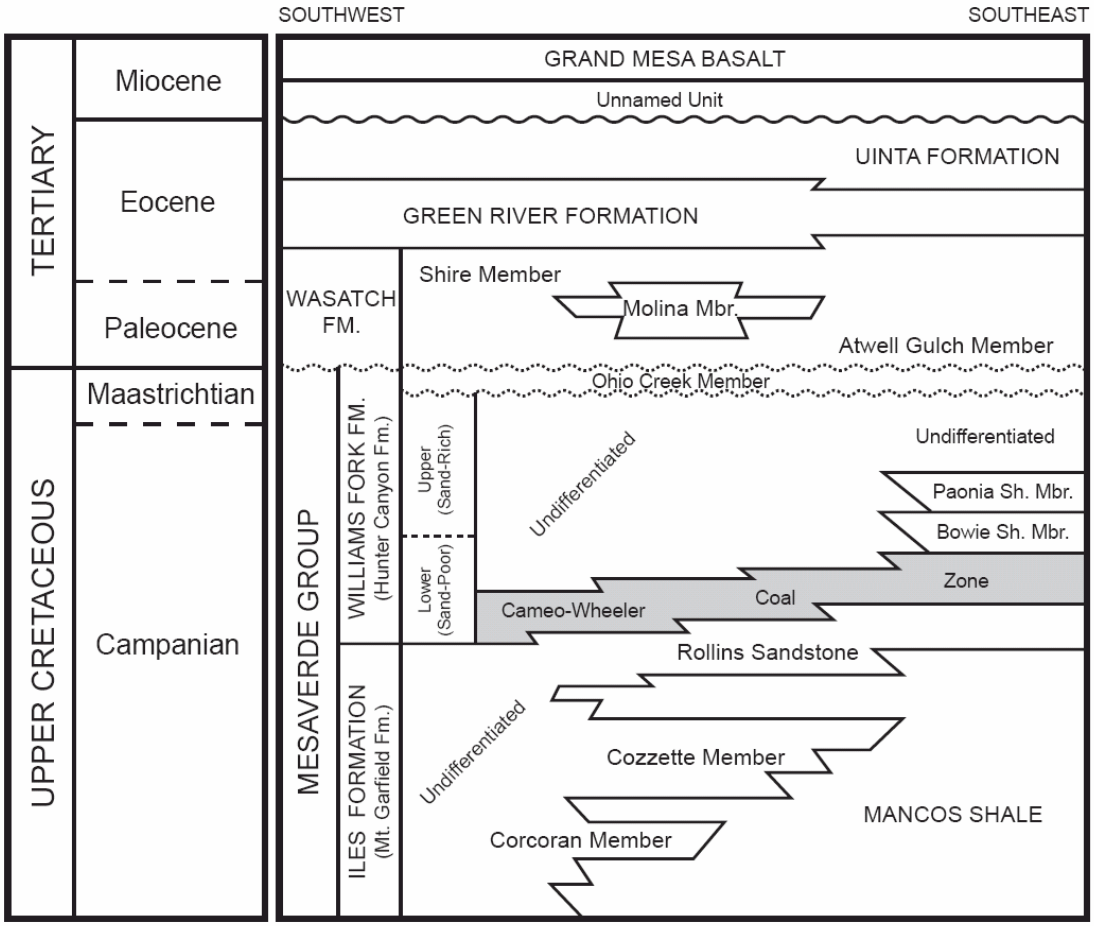

Figure 2.1. Stratigraphic nomenclature used in the Piceance basin. Modified from Cole and Cumella (2003).

separates the Cretaceous and Tertiary deposits. The Tertiary Wasatch, Green River, and Uinta Formations are exposed in the basin due to erosion over the past 30 million years. Figure 2.2 shows a typical log and stratigraphic subdivision in Rulison field based on the RWF 542-20 gamma ray log of the imaged interval.

2.2. Regional Structure

During the Late Cretaceous (Late Campanian to Maastrichtian), the central part of North America was covered by the Western Interior Seaway. Located to the west of the seaway, a thrust belt complex (known as the Sevier Orogeny) was the primary source of sediment for the basin (Figure 2.3). The thrust belt activity increased during the late Campanian and caused progressive movement of the shoreline to the east (Johnson, 1989).

During the Laramide Orogeny, which began during the Campanian and continued through to the Eocene (Tweto, 1975), the foreland basin was divided into intermontane basins, such as the Piceance basin in Colorado and the Uinta basin in Utah. A major episode of deformation occurred during the early stages of the Laramide Orogeny, which is characterized by thrusting along the eastern margin of the basin. The thrust system is underlain by a decollement that developed due to mechanically weak evaporites in the Middle Pennsylvanian section (Grout and Verbeek, 1992).

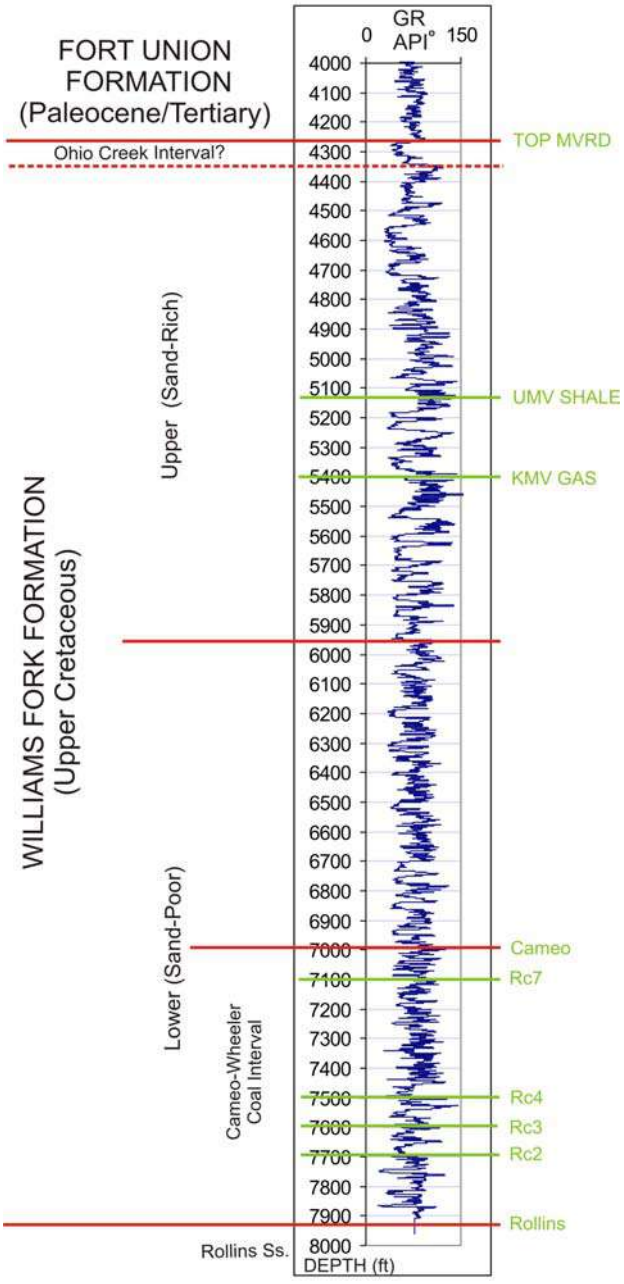

Figure 2.2. Marker beds in the RWF 542-20 study well. Marker depths (green text) are courtesy of Williams Corp. RC2, 3, 4 and 7 are coal beds. Depth is in feet. Abbreviations: GR=gamma ray; MVRD= Mesaverde; UMV= Upper Mesaverde; KMV= Cretaceous Mesaverde.

Figure 2.3. Western Interior Seaway during early Maastrichtian (Late Cretaceous). Present-day North America outline is shown (black line). From Gill and Cobban (1973) modified by Panjaitan (2006). Abbreviation: PB=Piceance Basin.

Today, the Piceance basin covers an area of over 6000 mi^2 (15540 km^2). It is bounded by the Uinta Mountain Uplift on the northwest, the Axial Arch on the north, the White River Uplift on the east, the Elk Mountains and Wasatch Uplift on the southeast, the Gunnison Uplift and San Juan volcanic field on the south, the Uncompahgre Uplift on the southwest, and the Douglas Creek Arch on the west (Figure 2.4). The basin is a northwest-southeast trending elongate basin that dips gently on the western flank and is steeply dipping to overturned on the eastern flank. Geologic structures such as monoclines, synclines and anticlines generally have the same NW-SE trend.

2.3. Local Structural Setting

Based on information from a 3-D seismic survey and production data in the northeast part of Rulison field, there is a direct relationship between basement-controlled structures and the fracture distribution within the Williams Fork Formation (Hoak and Klawitter, 1997). This critical relationship is based on the parallelism between production contours, shallower subsurface structure, and the basement-fault orientation (Figure 2.5) (Hoak and Klawitter, 1997). The low-permeability reservoir has enhanced production when natural fractures are present (Lorenz and Finley, 1991; Hoak and Klawitter, 1997; Cumella and Ostby, 2003). In this field, small thrusts, related to deeper basement structures, terminate up-section in the coals and fluvial sandstones of Mesaverde

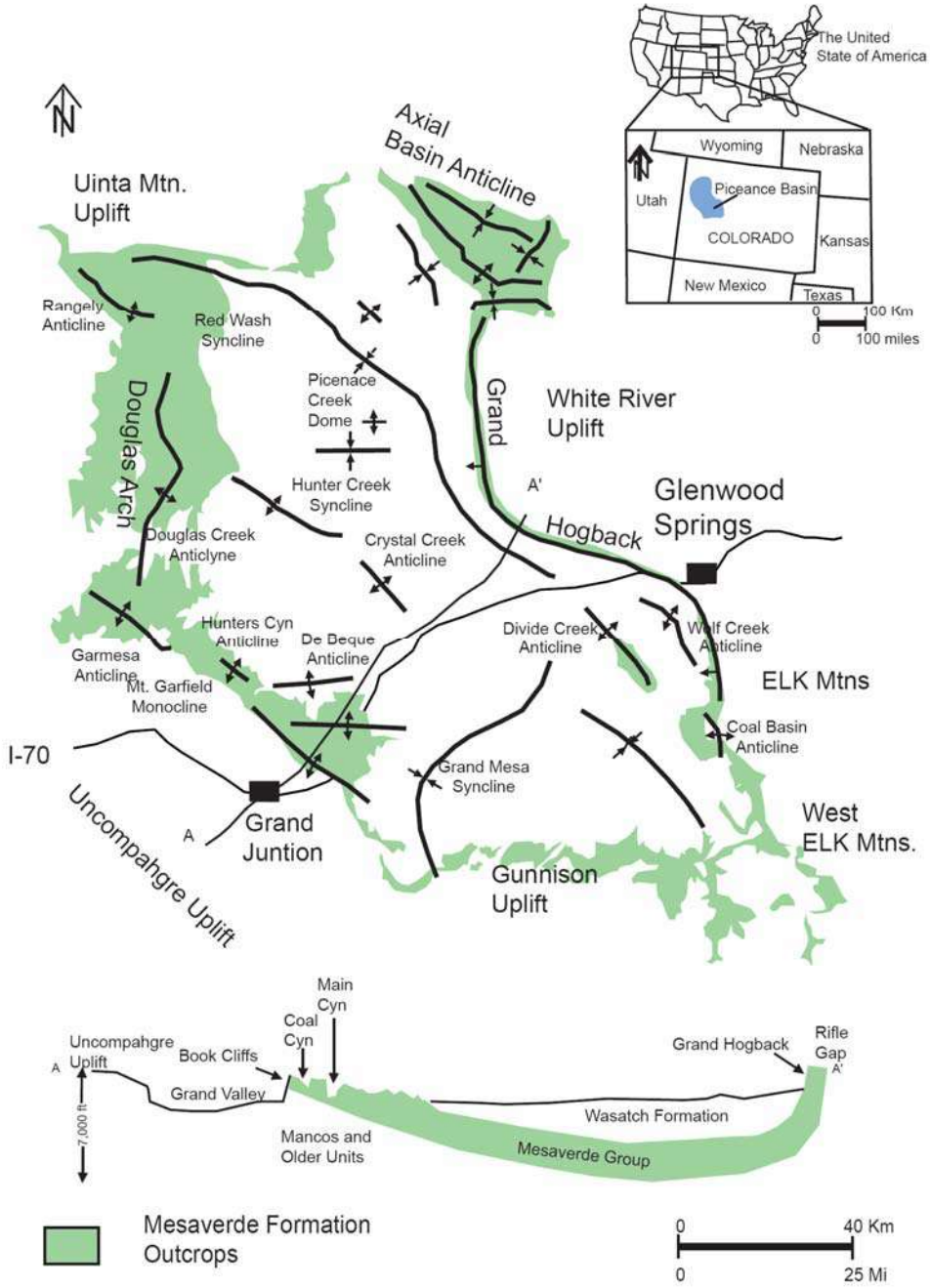

Figure 2.4. Main structural features of the Piceance basin. The structural cross section is diagrammatic. Modified from Cole and Cumella (2003).

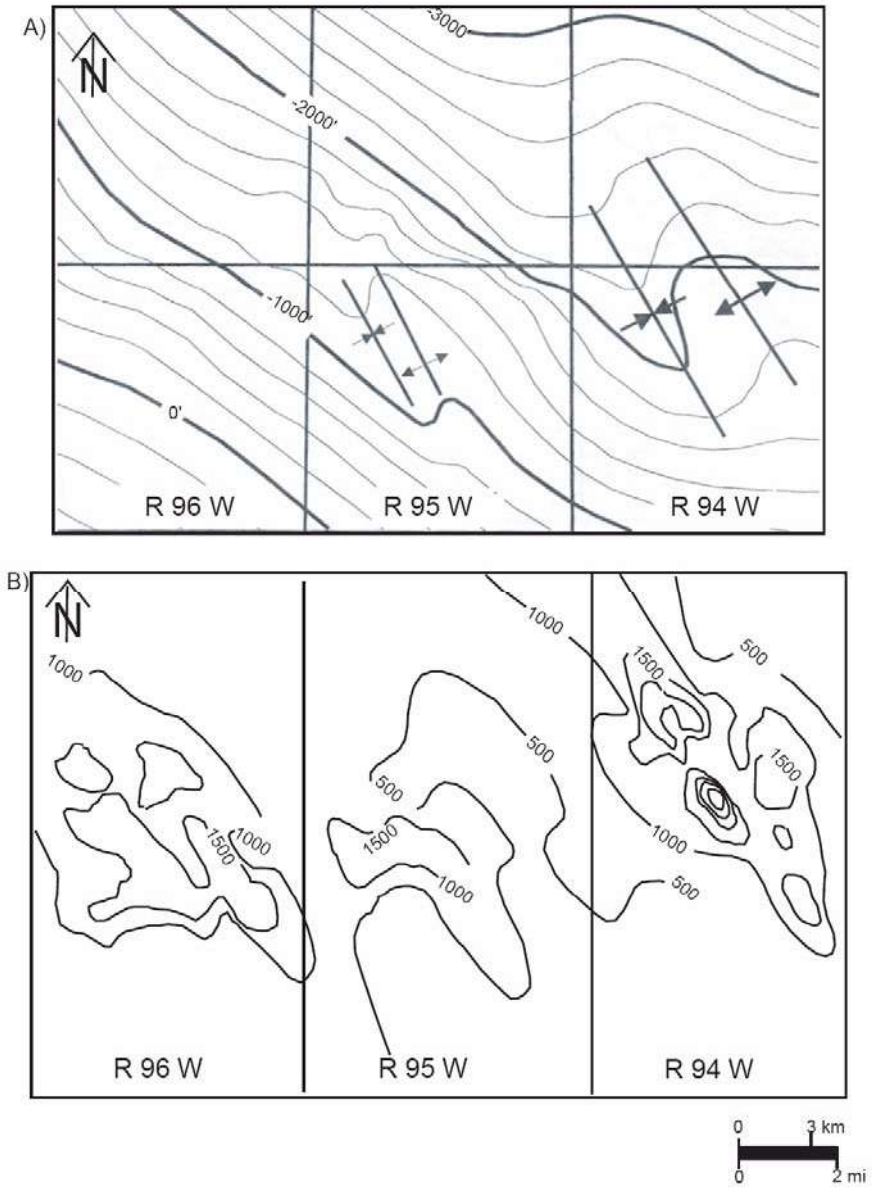

Figure 2.5. Comparison between (A) Rollins structure map and (B) estimated ultimate recoverable (EUR) data for the Grand Valley-Parachute-Rulison fields. Areas of enhanced production in Rulison and Parachute fields directly overlie the areas where local folding is more pronounced. Contour interval is 200 ft for the Rollins structure map. Contour and posted data in MMCF in the EUR map. Approximate location of the Rulison field is on the right side of the maps (R 94 W). Modified from Hoak and Klawitter (1997).

Formation (Figure 2.6). The faults are simpler in the Frontier-Dakota level and become increasingly complex in the Iles through Cameo intervals where faults bifurcate. Logically, at the tip-line terminations of the faults, fracture permeability is greatly enhanced. It is likely that the natural fractures that enhance permeability are related to the splays (Cumella and Ostby, 2003). In Grand Valley, Parachute, and especially in Rulison field, the zones of enhanced production (thrusts, faults) trend northwest, and are parallel to the deeply seated structures.

The study by Cumella and Ostby (2003) has suggested that wrench tectonics is the dominant structural style of the northwest-trending features. The left-lateral, transpressional structural style was proposed from interpretation of 3-D seismic data in the Piceance basin. The first set of faults is northwest-trending (N45^{o}W), near-vertical, and has left-lateral slip. The second set is north-northwest trending (N20^{o}W), has a dip of 30 to 60 degrees, and has reverse character. Cumella and Ostby (2003) explained that east-west Laramide compression produced left-lateral slip along pre-existing northwest-trending faults.

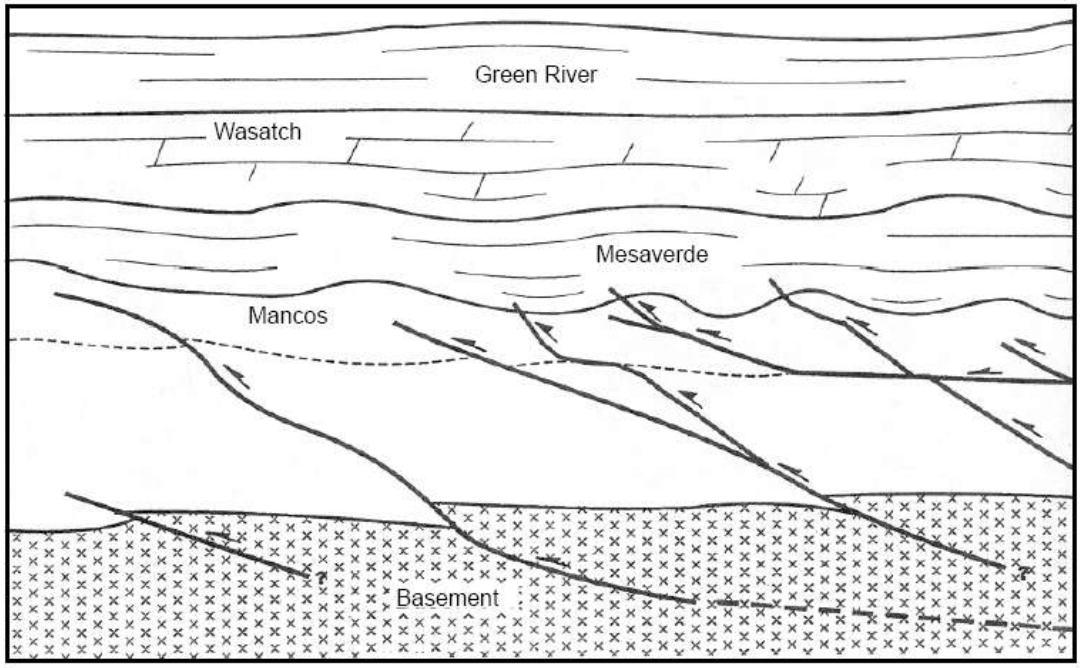

Figure 2.6. Schematic illustration of the multiple detachment surfaces interpreted in the eastern and central Piceance basin. Modified from Hoak and Klawitter (1997).

2.4 Petroleum System

Upper Cretaceous rocks of the Piceance basin form an unconventional petroleum system, which is of economic importance in the western United States. It is considered a basin-centered gas system, characterized by regionally pervasive gas accumulations, abnormal reservoir pressures, and low permeabilities (Law, 2002). Recent estimates suggest that the Piceance basin contains between 566 billion and 1.13 trillion m^3 (20 and 40 tcf) of recoverable gas (USGS, 2003; Potential Gas Committee, 2003). Production occurs mainly from fractured, low-matrix permeability (0.1 to 2 μD) sandstones of the Lower Williams Fork Formation (Cumella and Ostby, 2003). This low permeability is the result of authigenic clays, carbonate cement, and quartz overgrowths which occurred during a period of intense regional diagenesis (Johnson, 1989; Kuuskraa et al., 1997).

Yurewicz et al. (2003) studied the source rocks and hydrocarbon generation in the northern Piceance basin using outcrop and core data. Their results indicate three main sources: 1) marine shales within the Mancos Shale and Mesaverde Group, 2) coal seams within the Iles and Williams Fork Formations, and 3) non-marine shales within the Iles and Williams Fork Formations. The largest volume of gas was generated from the Cameo coal interval within the Mesaverde Group. Timing of gas generation coincides with maximum burial of the reservoir interval during the Oligocene Epoch (33.7 to 23.8 Ma) (Payne et al., 2000). The dominant trapping mechanism is stratigraphic, related to the

stacking of fluvial sand bodies surrounded by floodplain mudstones, although structural-stratigraphic traps are also present (Spencer, 1989).

CHAPTER 3

BOREHOLE IMAGE INTERPRETATION

3.1. Data Available

The RWF 542-20, RWF 523-20 and RMV 60-17 borehole image logs have been analyzed for sedimentary and structural features. Sedimentary features include interpretation of bed boundaries, cross bedding, scour surfaces, soft-sediment deformation and gas seeps. Structural features include drilling induced fractures, natural fractures (open, resistive), borehole breakouts and faults. The RWF 441-20 well was interpreted by Patrick Garrow (Halliburton image log interpreter). The rose diagrams from his report were used to support the interpretation of the three mentioned wells.

The gamma ray log is used to define shale beds, which are used for the structural dip-domain analysis. Two types of dip-domain analyses were performed: cumulative dip plots and dip azimuth vector plots.

3.1.1. EMI Borehole Image Logs

The imaged interval for the RWF 542-20 well spans from 4000 to 8000 ft measured depth, is focused on the Williams Fork Formation, and encompasses the main productive interval between the UMV shale and Cameo coal tops. Approximately 4000 ft (1200 m) of image log has been interpreted. The RWF 441-20 image log was recorded in the productive zone between the UMV shale and Cameo coal tops, from 3941 to 7962 ft.

3.1.2. FMI Borehole Image Logs

The imaged interval for the RWF 523-20 well spans from 5500 to 8000 ft measured depth. The main focus is on the productive interval in the Williams Fork Formation. The interval of interest is roughly between the top of the Rollins Member and the UMV shale marker. Finally, the imaged interval for the RMV 60-17 well spans from 5500 to 8000 ft measured depth. Again, the image log focus is on the productive interval of the Williams Fork Formation, between the UMV shale and RC2A markers.

3.2. Physical Principles of Resistivity Image Logs

Borehole imagery is one type of open-hole log that provides high-resolution data for improved reservoir characterization. As the name reveals, the electrical borehole image tool gives an electrical "picture" of the borehole. The tool obtains an image by measuring electric resistivity contrast between different parts of the rock and fluids close to the borehole wall.

Electrical borehole imaging tools emerged from the electrical dipmeters. Figure 3.1 shows the tool configuration and basic principles behind dipmeter logs. In essence, borehole imaging tools are sophisticated dipmeters. Like the dipmeter, the imaging tool has microresistivity electrodes arranged around the wellbore on pads that are pressed against the borehole wall. The number of electrodes changes from a few in a dipmeter to a complex array of electrodes on multiple pads in electrical borehole-imaging tools (Figure 3.2). Electrodes (buttons) induce current into the formation. After current interacts with the formation, the signal is measured and then turned into the "map" of rock resistivity at the borehole face. More conductive material is assigned darker tones (brown) and more resistive material is light colored (yellow) (Figure 3.3). Areal coverage of the borehole face is a function of the width of the electrode arrays, number of pads, and borehole diameter. In general, 40 to 80% of the borehole face is imaged in typical boreholes (Hurley, 2004). Unimaged parts of the borehole appear as blank strips between pads (Figure 3.3). Because the image log display would be difficult to examine in the

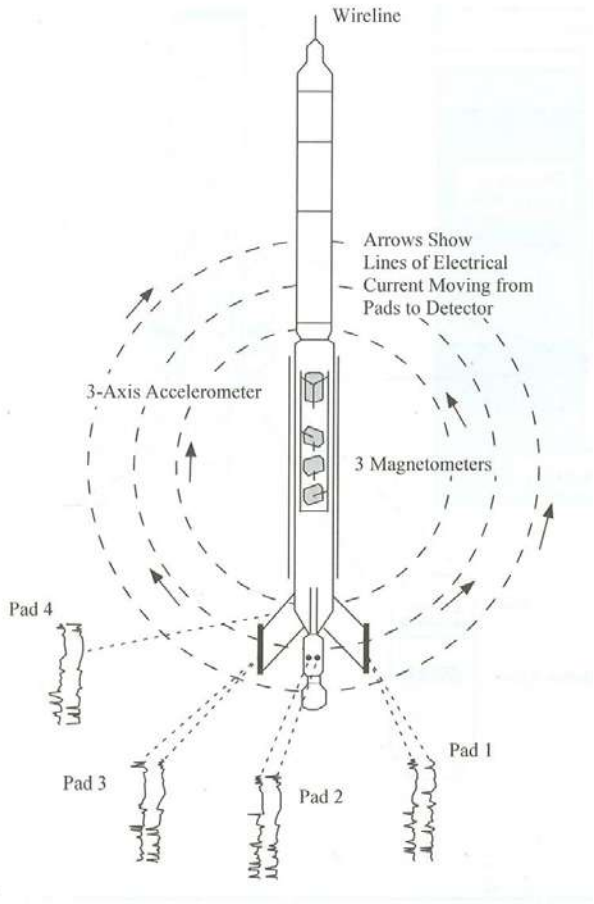

Figure 3.1. Basic principles of electrical dipmeter tools are illustrated by this diagram of Schlumberger's SHDT (Stratigraphic High Resolution Dipmeter Tool), which became commercially available in 1982. Two measuring electrodes on each of four pads generate eight electrode traces, as shown at the bottom. Magnetometers measure borehole deviation. Accelerometers record high-frequency tool-speed variations which occur as the tool is being run. Formation dip is computed from planes that are fit through correlative peaks and troughs on the speed-corrected electrode traces. Caliper logs record borehole diameter between pads 1 and 3 and between pads 2 and 4. After Höcker et al. (1990).

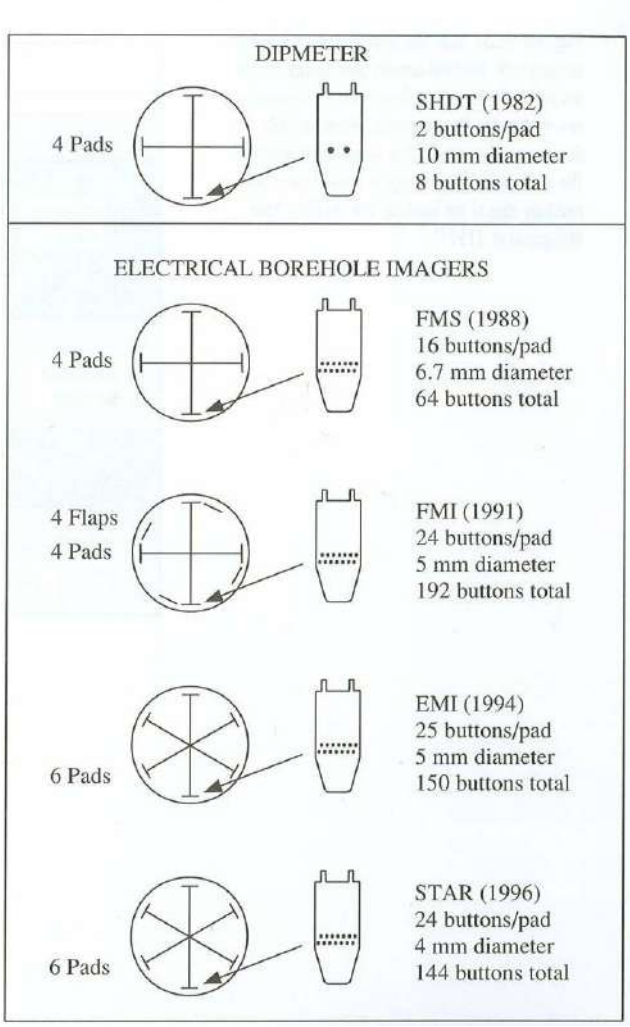

Figure 3.2. Schematic illustration of pad and electrode configuration for one dipmeter and all of the common electrical borehole-imaging tools. After Hurley (2004).

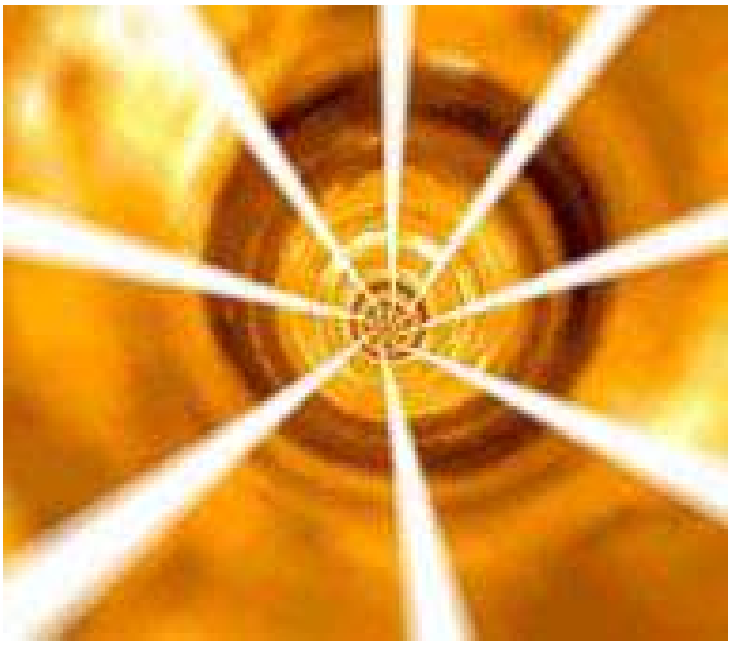

Figure 3.3. More conductive material is assigned darker tones (brown) and more resistive material is light colored (yellow). Unimaged parts of the borehole appear as blank strips between pads. From Schlumberger FMI brochure website.

form of cylinder, it is common to split the borehole along true north. The image resembles an unrolled cylindrical photograph of the borehole wall (Figure 3.4). Planar features that intersect the borehole appear as sine waves (Figure 3.5).

Borehole data can be displayed as either static or dynamic images. Static images are created when one contrast setting is applied to the entire well, whereas dynamic images have variable contrast. Some of the subtle features are better viewed in the dynamic mode.

Generally, borehole images are used to:

- Characterize fracture and fault systems.
- Interpret stratigraphic discontinuities.
- Quantify pay in thin-bed packages.
- Interpret environments of deposition.
- Resolve sandstone-body geometry and paleocurrent orientation.

Today, most of the service companies have tools constructed on the same principles. For this study the borehole image logs from Schlumberger's Formation MicroImager™ (FMI) and Halliburton's Electric Micro Imager™ (EMI) tool were used.

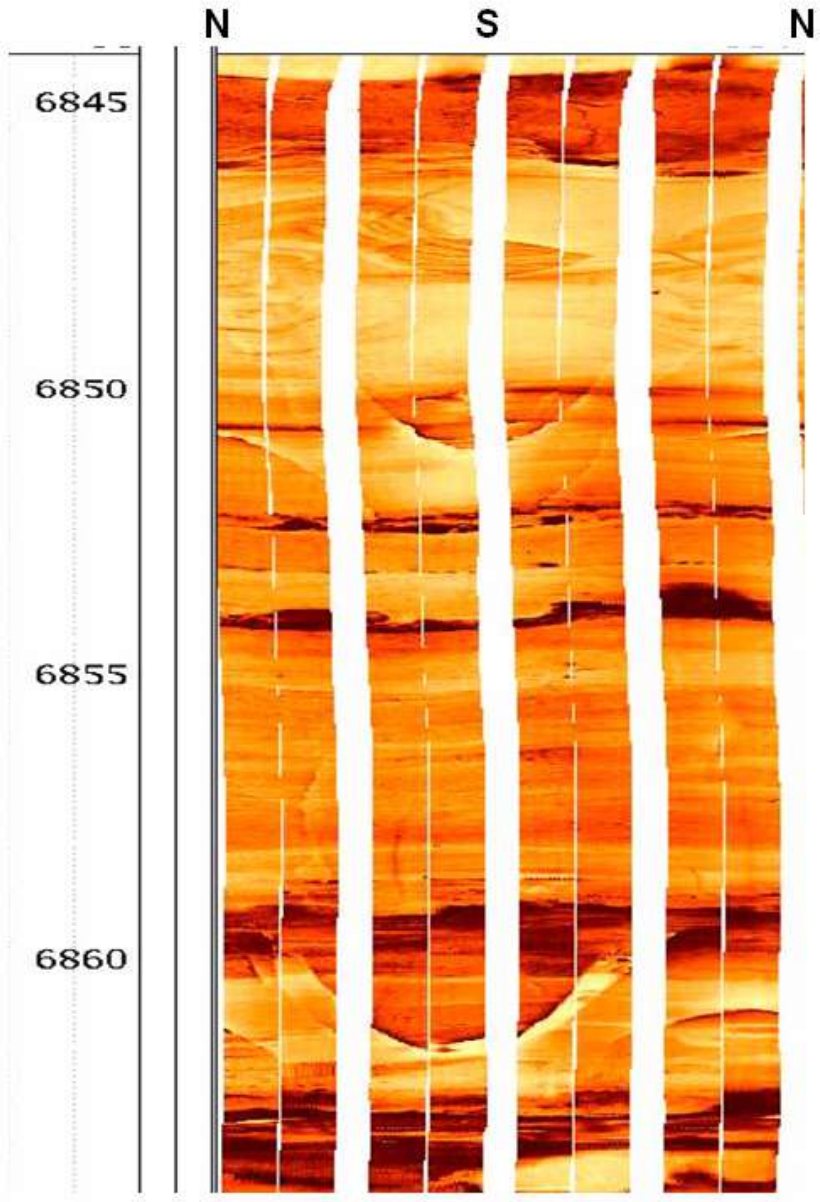

Figure 3.4. The image resembles an unrolled cylindrical photograph of the borehole wall. Notice the eight tracks created by the pads of the FMI tool. Image taken in the RWF 523-20 well. Vertical scale in feet.

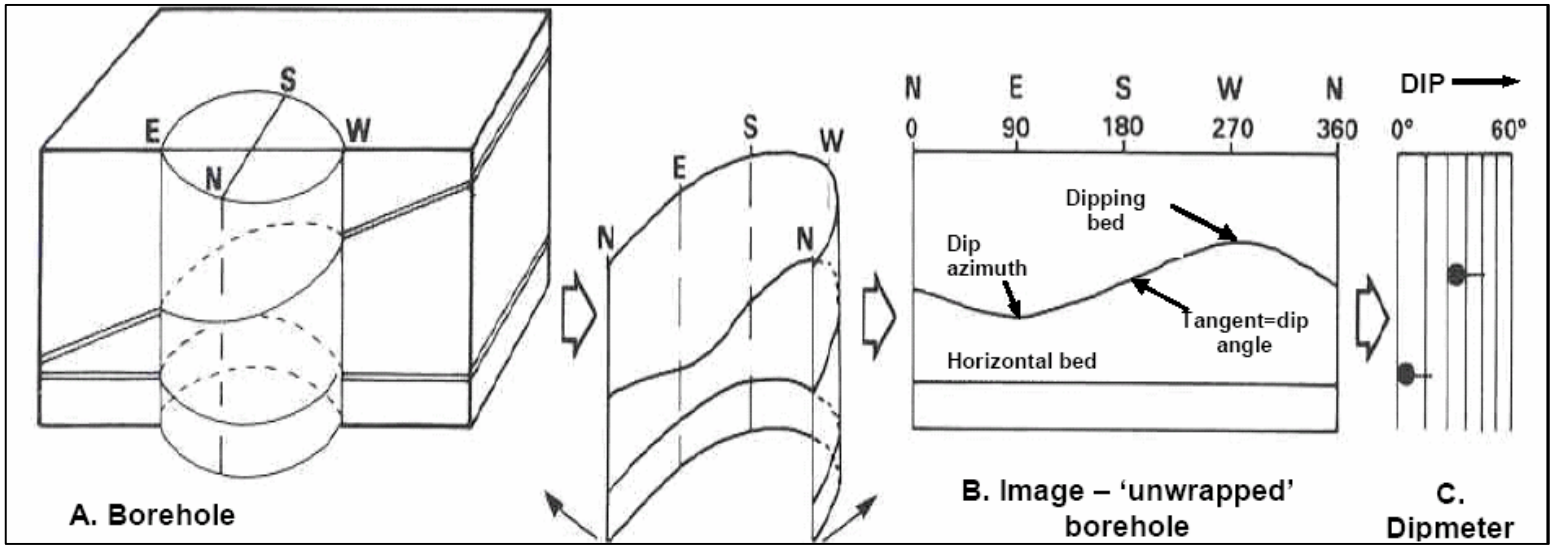

Figure 3.5. Borehole-image displays. The images from borehole (A) are presented on a flat surface (screen or hard copy plot) by "unwrapping" onto a vertical depth grid and horizontal grid of compass bearing. (B) The horizontal and vertical surfaces are unchanged but dipping surfaces become represented by a sinusoid or sine wave. (C) Dip and azimuth from sine wave is represented on a dipmeter tadpole plot. Modified from Rider (1996).

3.3. FMI Tool Specifications

The Formation MicroImager (Figure 3.6) is a high-resolution microresistivity logging device introduced in 1991 by Schlumberger, which evolved from the Formation MicroScanner (FMS). The vertical resolution of the FMI is 0.2 in (0.5 cm) (Allen et al., 1988). The tool has four orthogonal pads and four flap pads. Each pad has 24 button electrodes for a total of 192 electrodes. The tool has 2 electrical current components. The high-resolution component detects resistivity variations in the formation directly facing each button. The variation of resistivity values in front of each individual button creates the high-resolution image. The low-resolution component is modulated by the resistivity interval between the upper and lower pads (Schlumberger web site, 2006). Depending on the diameter of the hole, the pads cover approximately 80% of the borehole wall.

3.4. EMI Tool Specifications

In 1994, Halliburton introduced the EMI Electrical Micro Imaging tool, a microresistivity imaging device featuring six arms (Figure 3.7). During logging, the six pads extend to make contact with the borehole wall at the desired downhole intervals. An electrical current flows from the pads into the surrounding rock then upward in the well bore to return at the top of the tool. Six pads contain a total of 150 calibrated

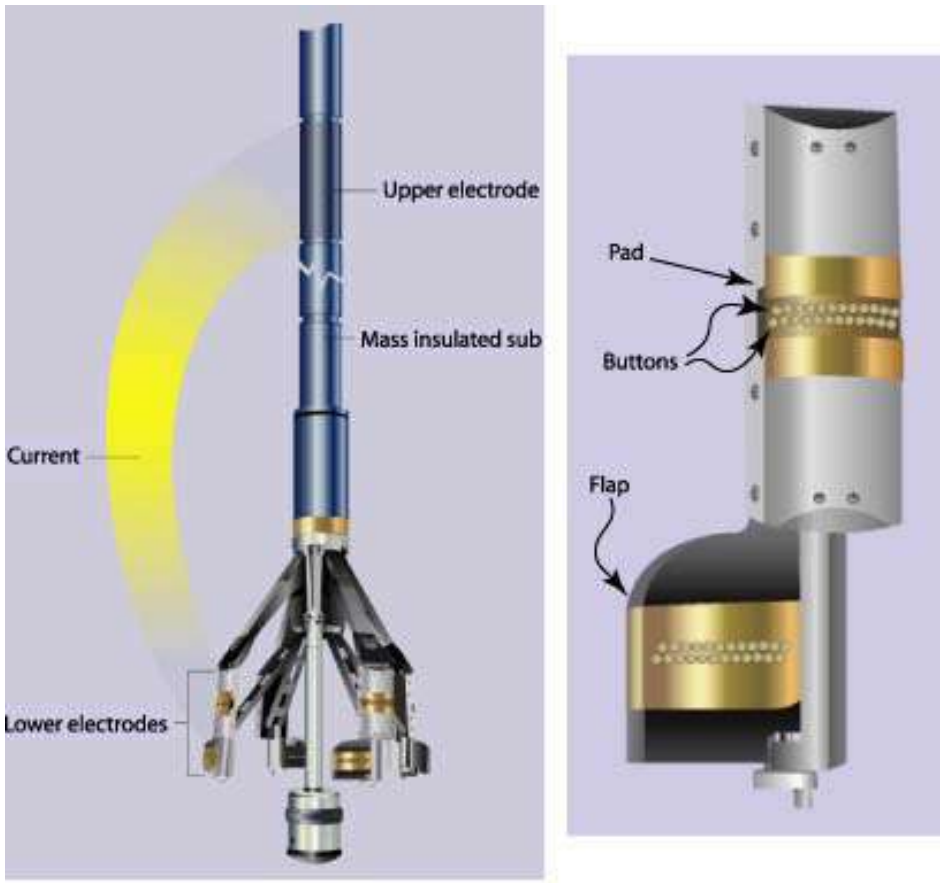

Figure 3.6. The Schlumberger FMI tool. At left, the tool is shown in an open position with the pads fully extended. The diagram on the left shows how the alternating current flows from each electrode button in the pad or flap through the formation to the upper electrode. The diagram on the right is a close-up of the pad (upper right) and flap (lower left). The electrode buttons can be seen on the assembly. The pad is considered the primary electrode and the flap is considered the secondary or auxiliary electrode. (After Schlumberger FMI brochure site).

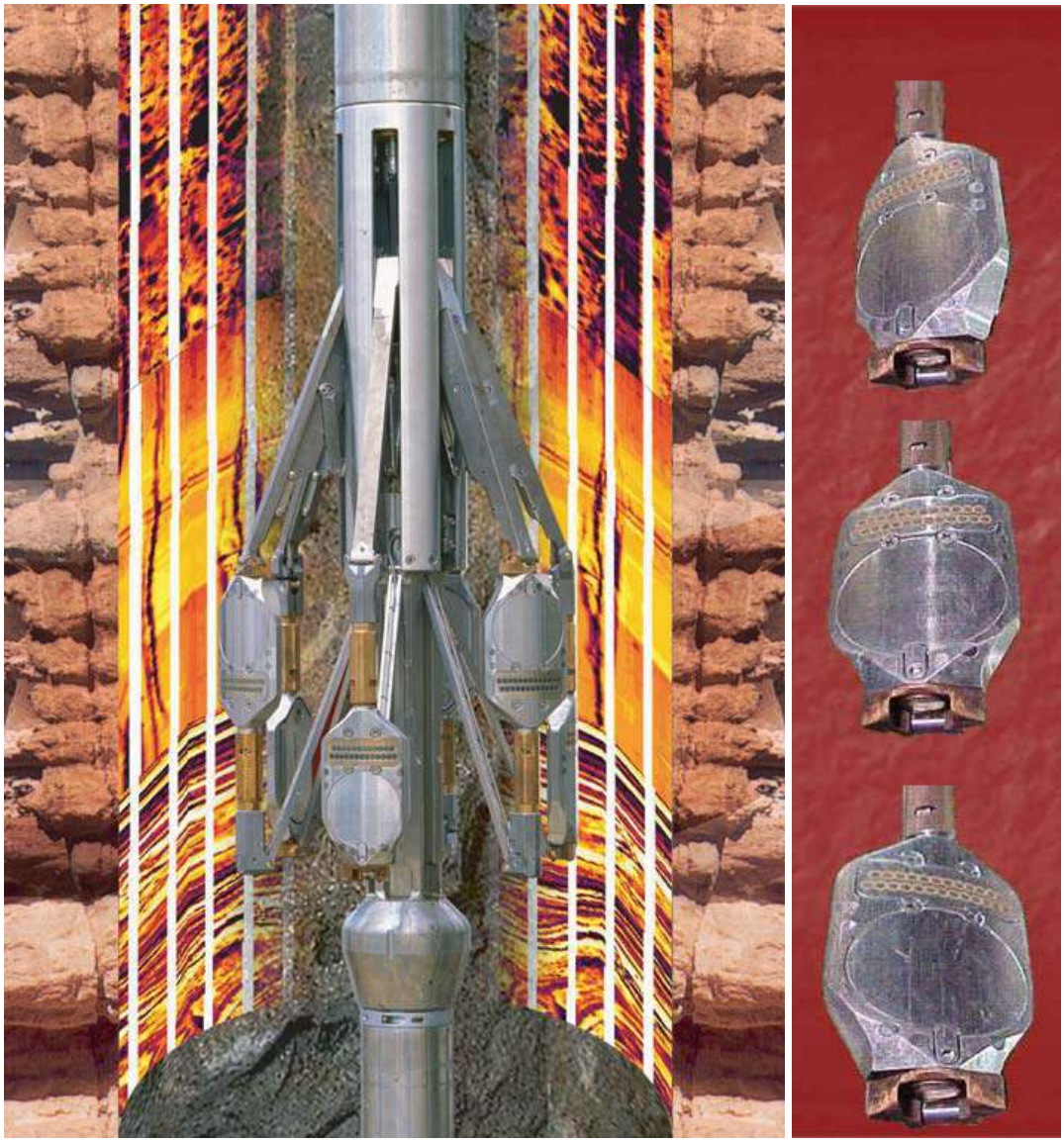

Figure 3.7. The Halliburton EMI tool. At left, the tool is shown in an open position with the 6 pads fully extended. The right portion of the image is a close-up of the pads (After Halliburton EMI brochure site).

microresistivity sensors. The 150 curves generated by the tool are processed at a sampling rate of 120 samples per ft, or one sample per 0.1 in (0.25 cm) (vertical resolution). With the help of the imaging software, the processed electromagnetic signal is then visualized like a cohesive, color-coded "map" of the borehole wall.

Relative wall coverage depends on the borehole diameter. The six pads provide average radial coverage of 60% around the borehole (Halliburton web site 2006).

3.5. Image Log Processing

Raw image data was processed using Recall/Review software by Janine Carlson. The overall image quality is good, although there are intervals that have streaked images and out-of-phase pads (Figure 3.8). The image is streaked when the tool travels too fast for it to properly record the image or when mud or debris builds up on the pads (Minton, 2002). The fast movement of the tool results when it releases after sticking in response to increased tension on the wireline. Out-of-phase pads occur due to sticking and jostling of the flaps and possibly disruptions of the accelerometer.

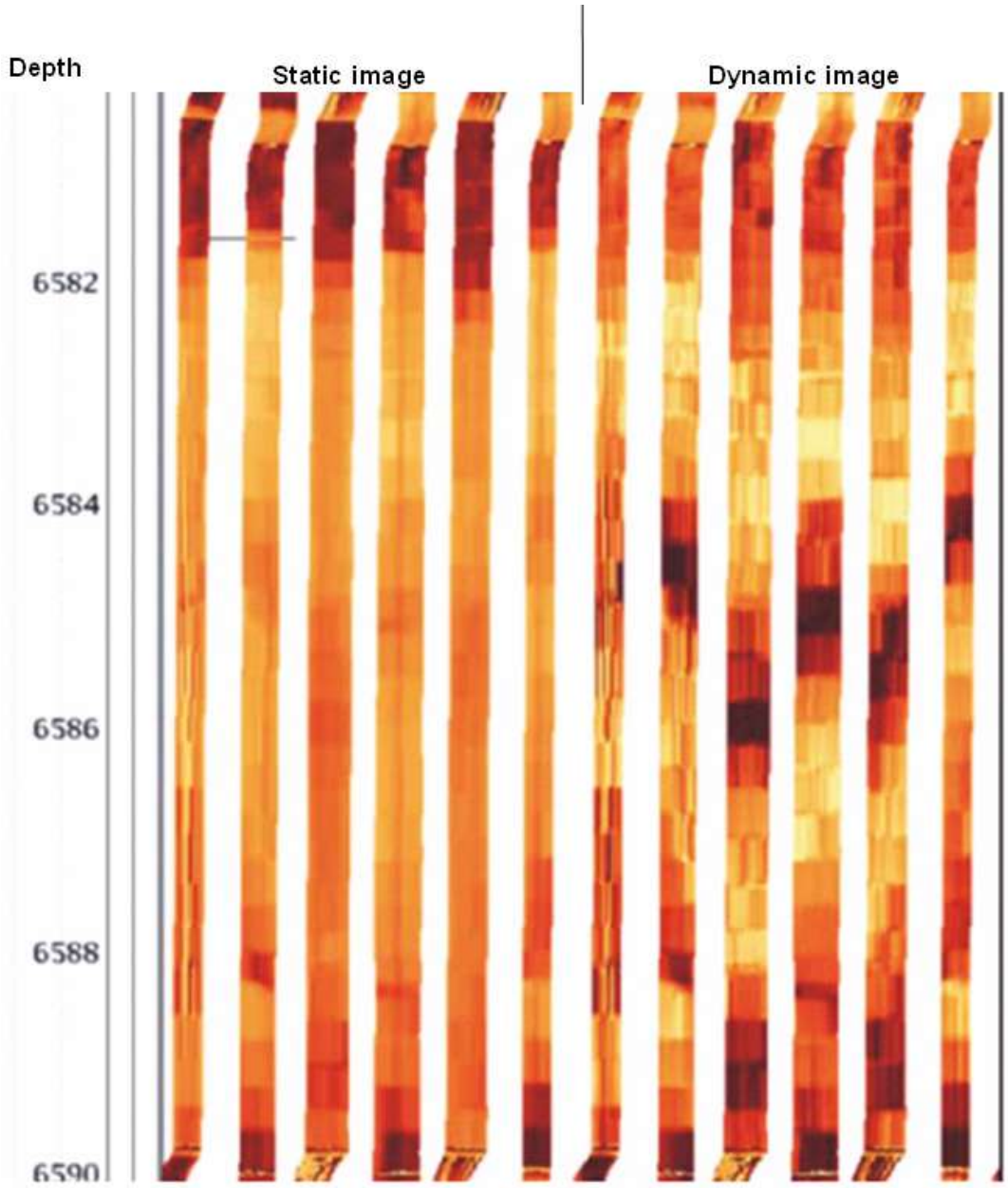

Figure 3.8. EMI image from RWF 542-20 showing out-of-phase pads which make interpretation difficult. Depth scale is in feet.

3.6. Methods of Borehole Image Log Interpretation

The RWF 542-20, RWF 523-20 and RMV 60-17 borehole image logs have been analyzed for sedimentary and structural features.

3.6.1. Sedimentary Features

Sedimentary features include interpretation of bed boundaries, cross bedding, scour surfaces, soft-sediment deformation and gas seeps. To interpret a planar feature, one fits a sine wave to the feature on the static or dynamic image. Every picked sine wave has information of dip and azimuth represented with a tadpole (Figure 3.5). Appendix A contains the interpreted features in the EMI and FMI logs.

Bed Boundary is the most abundant feature, picked on the high-contrast boundary of resistive (bright color) and non-resistive (dark color) beds (Figure 3.9). The feature was interpreted in conjunction with the gamma ray log. Next to every tadpole of the bed boundary there is a GR value attached. Later, the GR value of the bed boundary was used to apply a cutoff value. All beds with value higher than 80 API units (shales) were used for the dip-domain analyses.

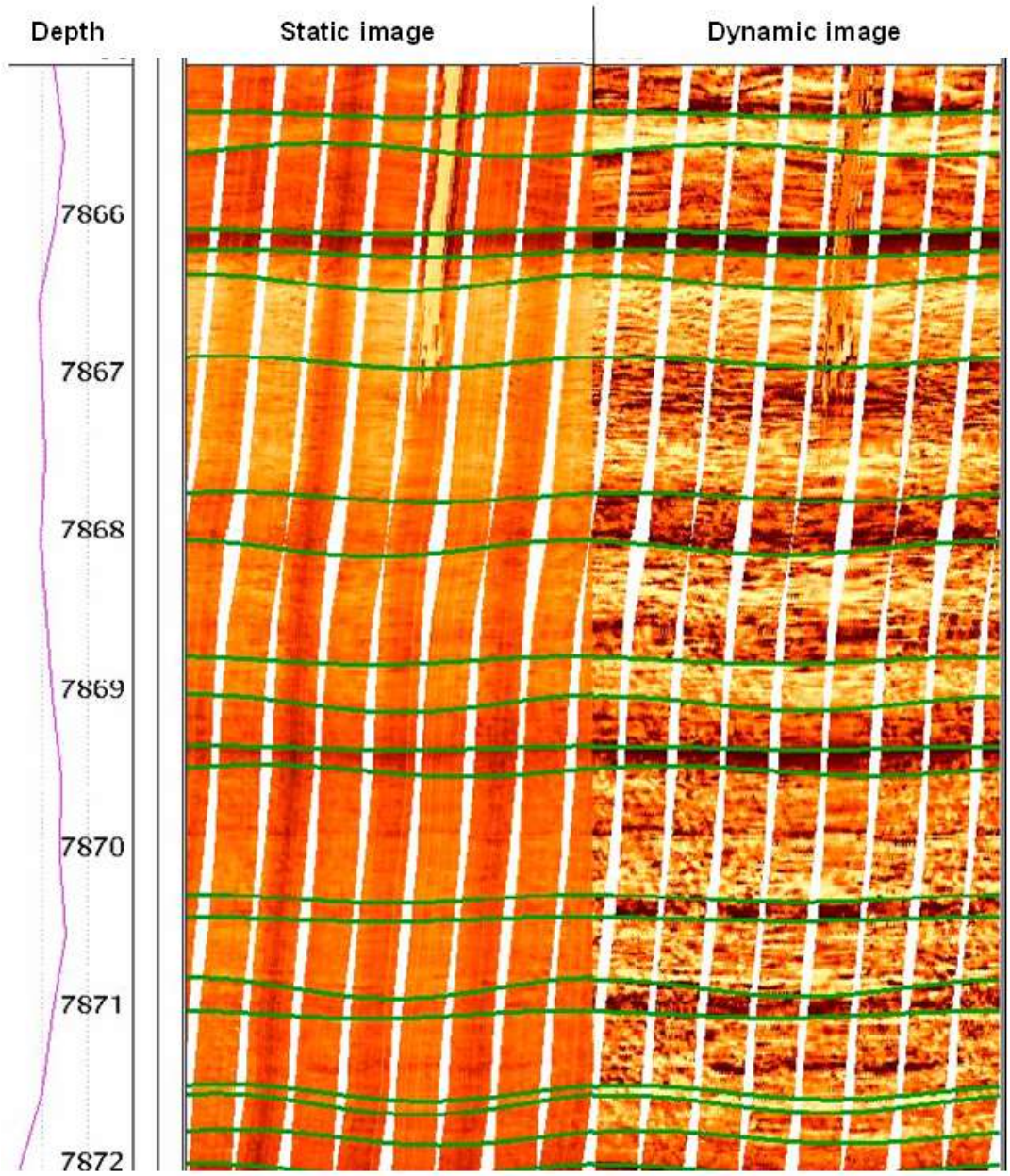

Figure 3.9. Image of bed boundaries in the RMV 60-17 well. The boundaries are picked on the boundary of resistive (bright color, sand) and non-resistive (dark color, shale) beds. Depth scale is in feet.

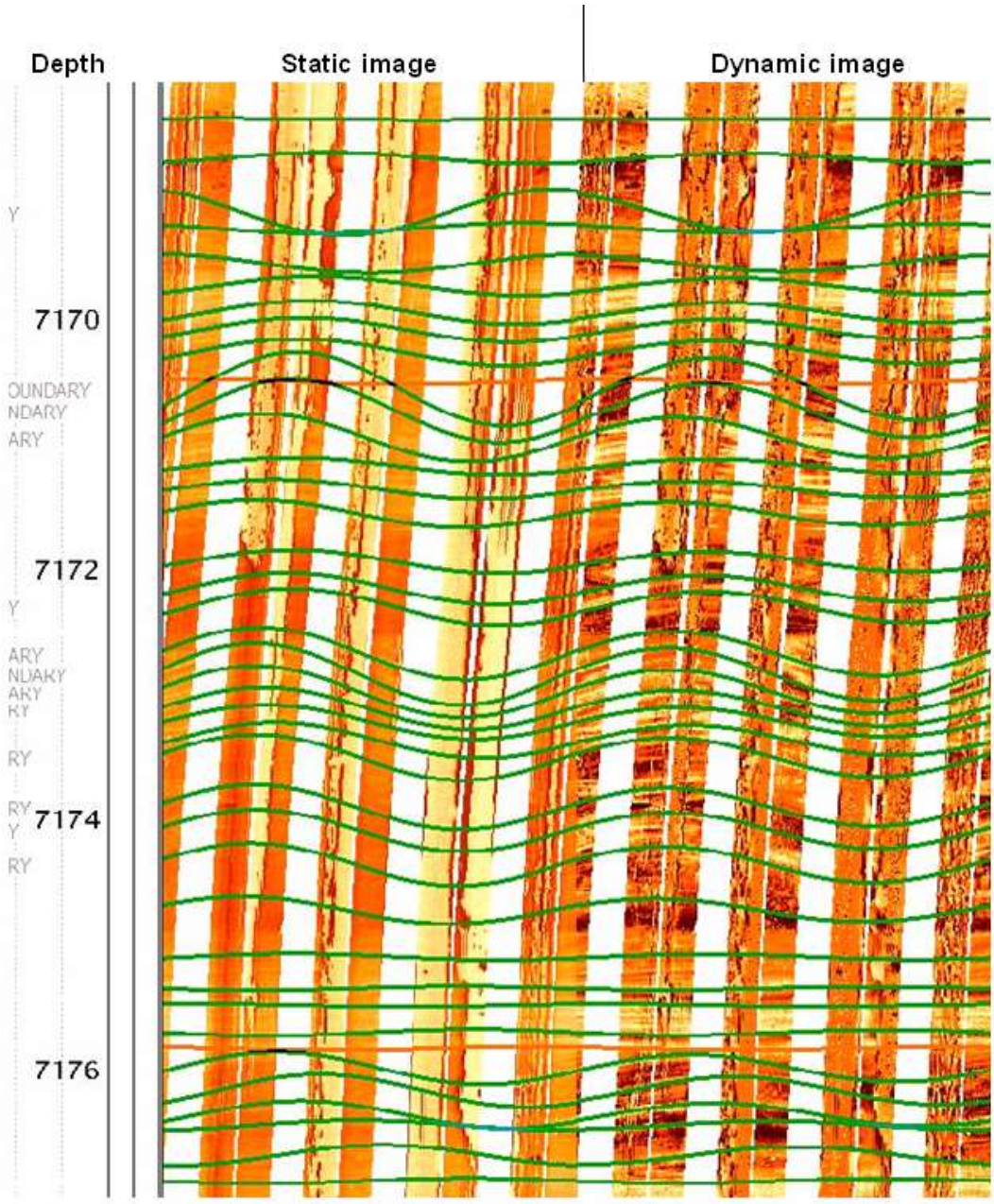

Figure 3.10. Image of a cross bedding in the RMV 60-17 well. There is a contrast in dip magnitude (green sine wave magnitude) between different sets of beds. Orange sine waves represent associated scour surfaces. Depth scale is in feet.

Cross bedding is a characteristic of sandstone intervals (Figure 3.10). This category commonly has an angular relationship with the underlying or overlying beds. Oriented tadpoles with dips greater than 5^{o} are interpreted as cross beds. In sand bodies, they usually occur as troughs and as lateral accretion surfaces, commonly associated with scour surfaces. The sine waves are picked both in static and dynamic images.

Scour surfaces are distinct features because of their truncation of underlying laminations or bedding (Figure 3.11). Two types of scouring exist in the examined wells. Internal scouring within sand bodies is associated with cross beds; basal channel scouring surfaces are commonly associated with rip-up clasts and carbonaceous plant debris. The clasts appear as dark-colored irregular features (Figure 3.12).

Soft-sediment deformation is an irregular feature which cannot easily be fitted with sine waves (Figure 3.13). Their geometry usually resembles slump folds, accompanied by probable water escape-features, with limbs steeply inclined. Soft-sediment deformations are intervals which usually disrupt cross beds.

Gas seeps are "bubbling" shapes picked with horizontal planes, determining a depth at which it occurs (Figure 3.14). Gas in the image logs obscures structural and stratigraphic features. One phenomenon associated with gas is that the bubble of gas is stuck under the tool pad and dragged along the borehole wall. Also, the bubble under the pad can obscure the shallower gas seep base and lead to a false interpretation about the quantities of gas. Another important factor is the mud weight. Overbalanced drilling and formation damage can cause gas to not flow into the well during drilling and during

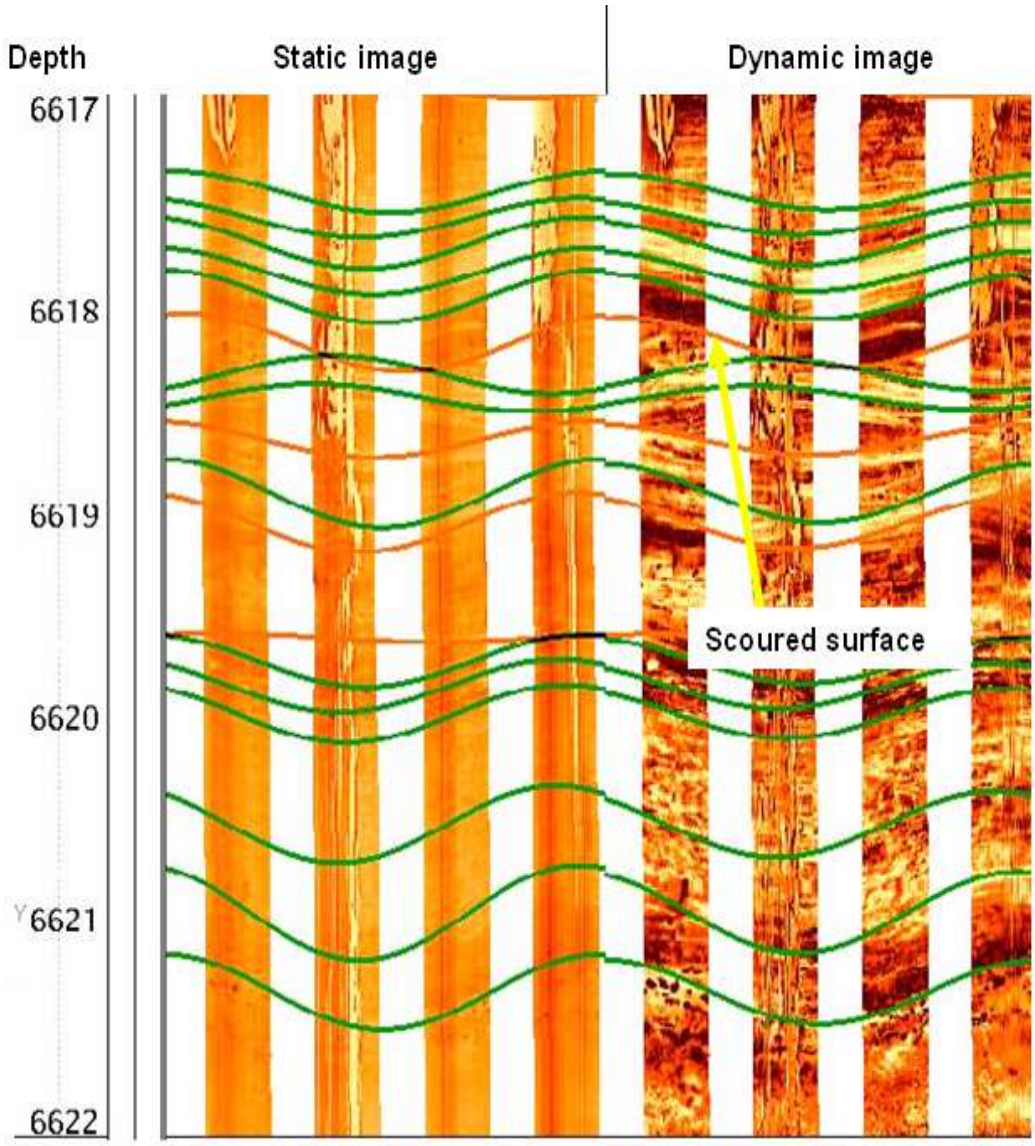

Figure 3.11. Image of a scoured surface in the RMV 60-17 well (orange sine wave). The underlying bed has been truncated by scoured surface. The depth scale is in feet.

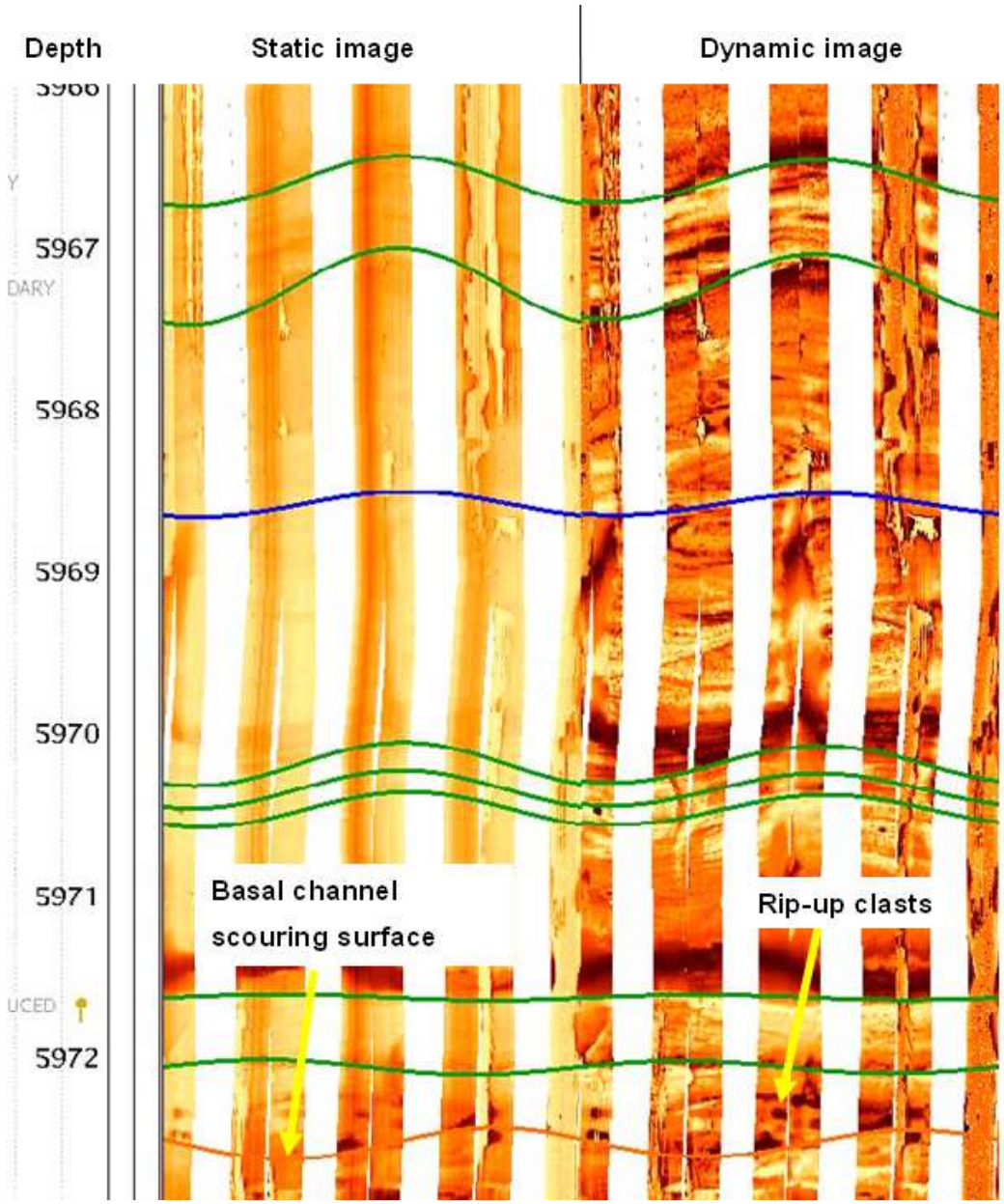

Figure 3.12. Basal channel surface which relates to scouring of the underlying bed in the RWF 523-20 well. The basal scour is associated with rip-up clasts within the sand body. Depth scale is in feet.

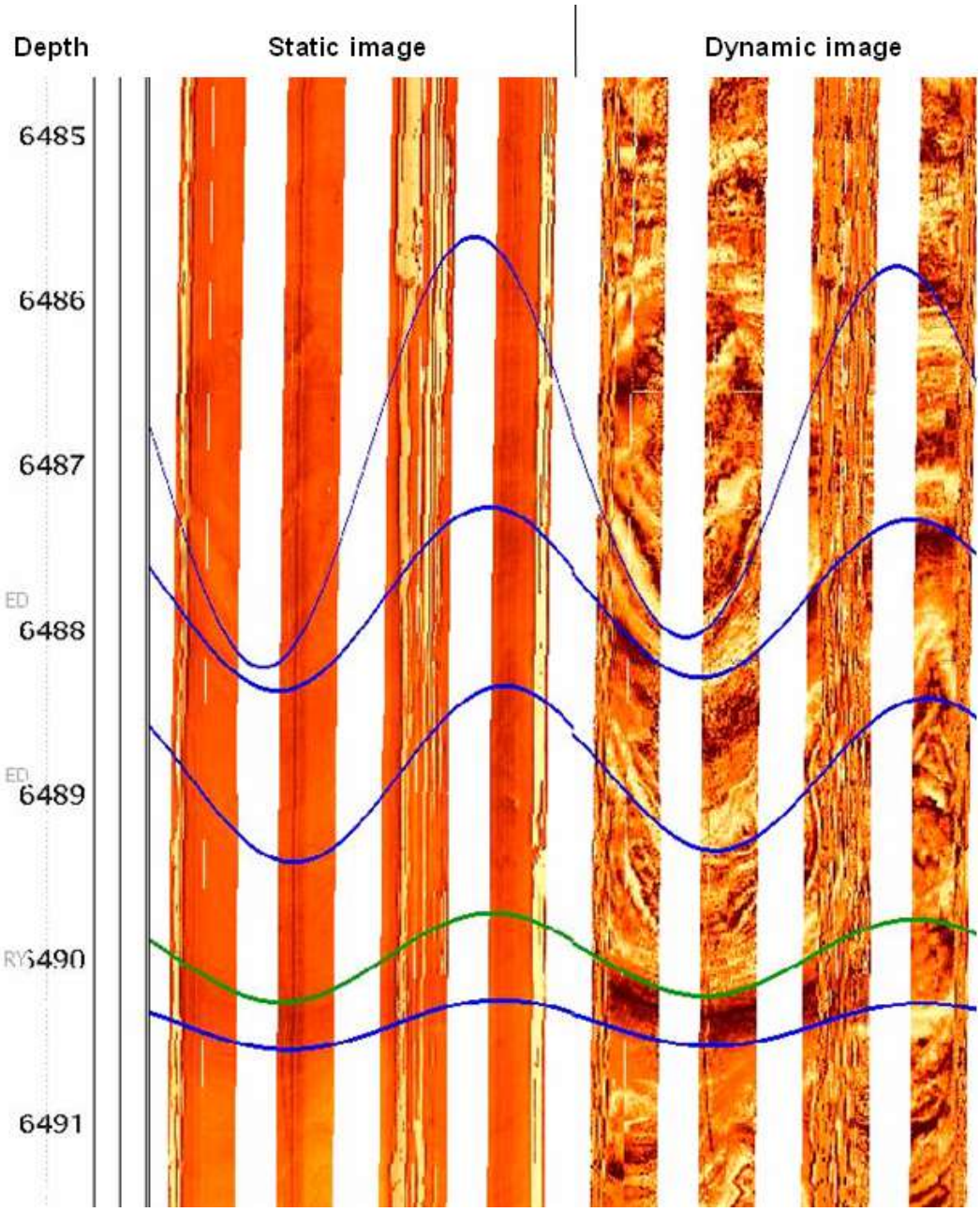

Figure 3.13. Example of soft-sediment deformation in the RWF 523-20 well (blue sine waves). Depth scale is in feet.

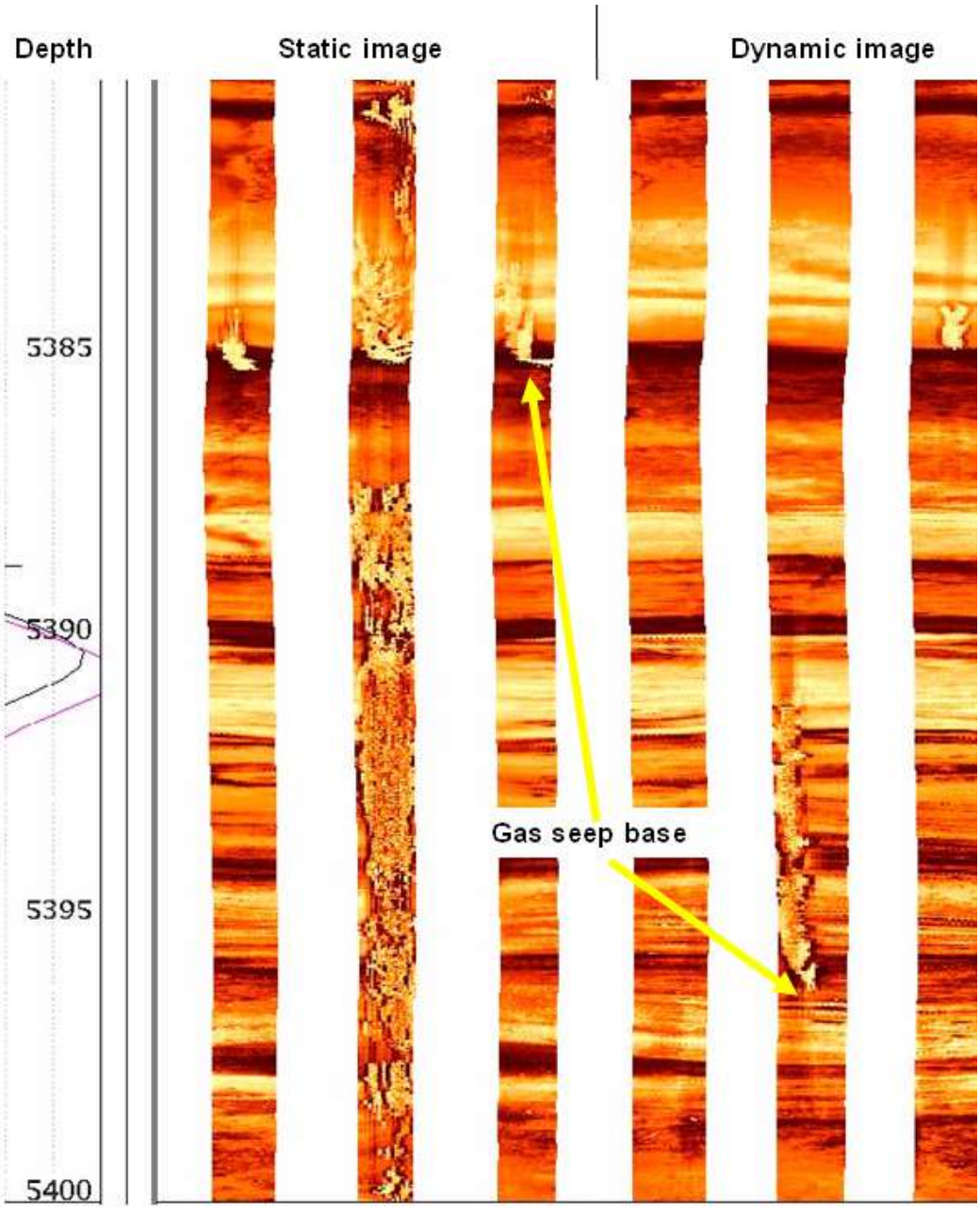

Figure 3.14. Image of gas seeps in the RWF 542-20 well. The gas seep base is the point at which the "bubbling" feature starts to occur. Depth scale is in feet.

image logging. Because of the mentioned factors, gas-seep base interpretation has to be approached with caution, and used as a qualitative indicator of gas presence.

3.6.2. Structural Features

This section shows examples of manually picked structural features such as borehole breakouts, fractures (drilling induced, open, healed), faults and microfaults. Like the sedimentary features, they are fitted with sine waves which give information concerning dip and azimuth.

Borehole breakouts, which form during or shortly after the drilling process, are hole elongations resulting from stress concentrations in a nonuniform stress field (Springer, 1987). They tend to form at the azimuth of the least principle horizontal stress. The resistivity images enable the identification of borehole breakouts in which they are seen as two parallel dark lines, separated by 180^{o} (Figure 3.15).

Fractures in this study are represented by two major groups: induced and natural. Induced fractures, caused by drilling processes, are always open and have connections to the borehole wall. Drilling conditions force borehole fluid into the fractures and the fluid in the fractures creates resistivity contrasts with the adjacent rocks. In resistivity imaging, the induced fractures are displayed in darker colors (Figure 3.16). They tend to form both

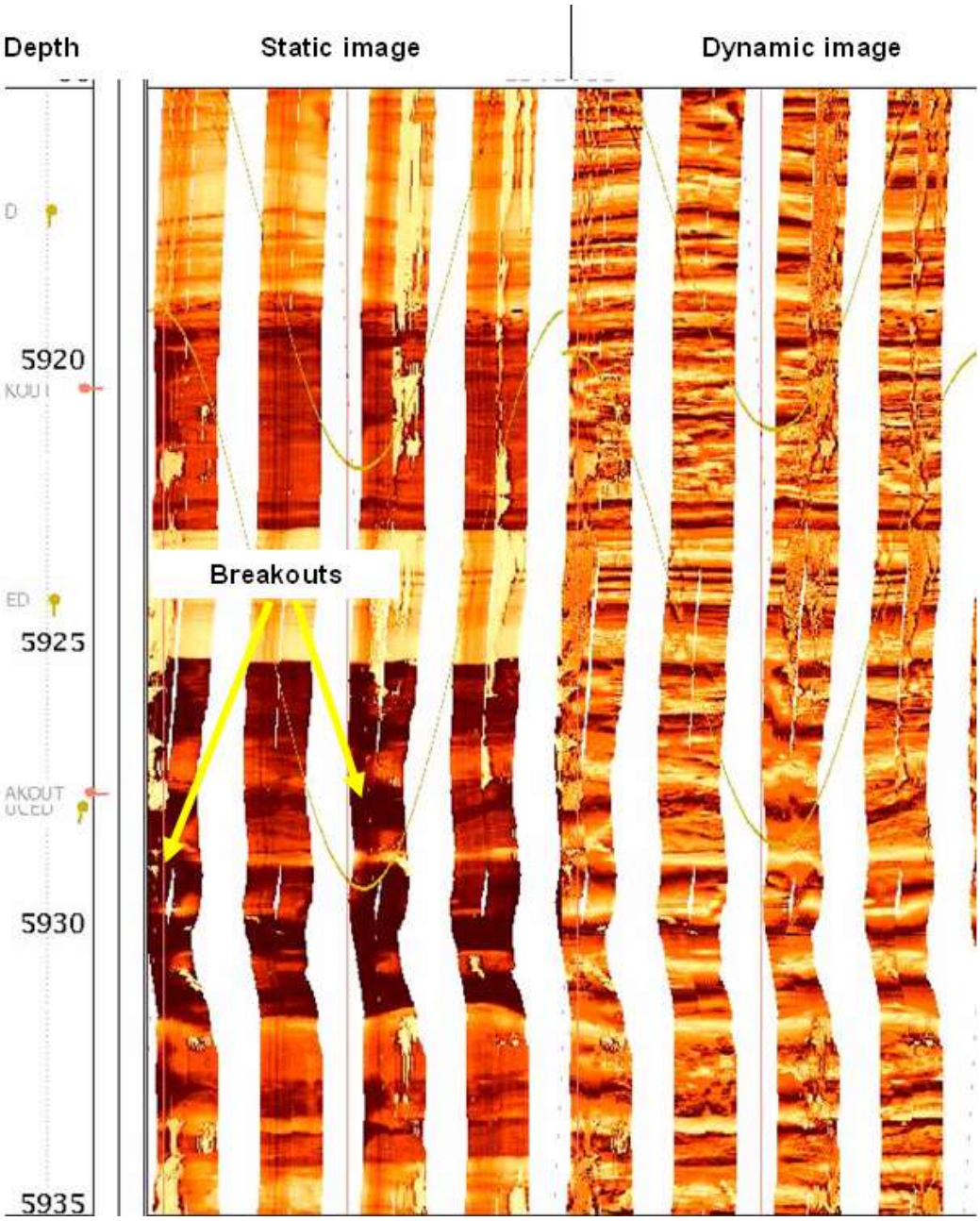

Figure 3.15. An example of borehole breakout (depth range: 5925 to 5935 ft) zone in the RWF 523-20 well. They are seen as two parallel dark lines, separated by 180^{o}. Depth scale is in feet.

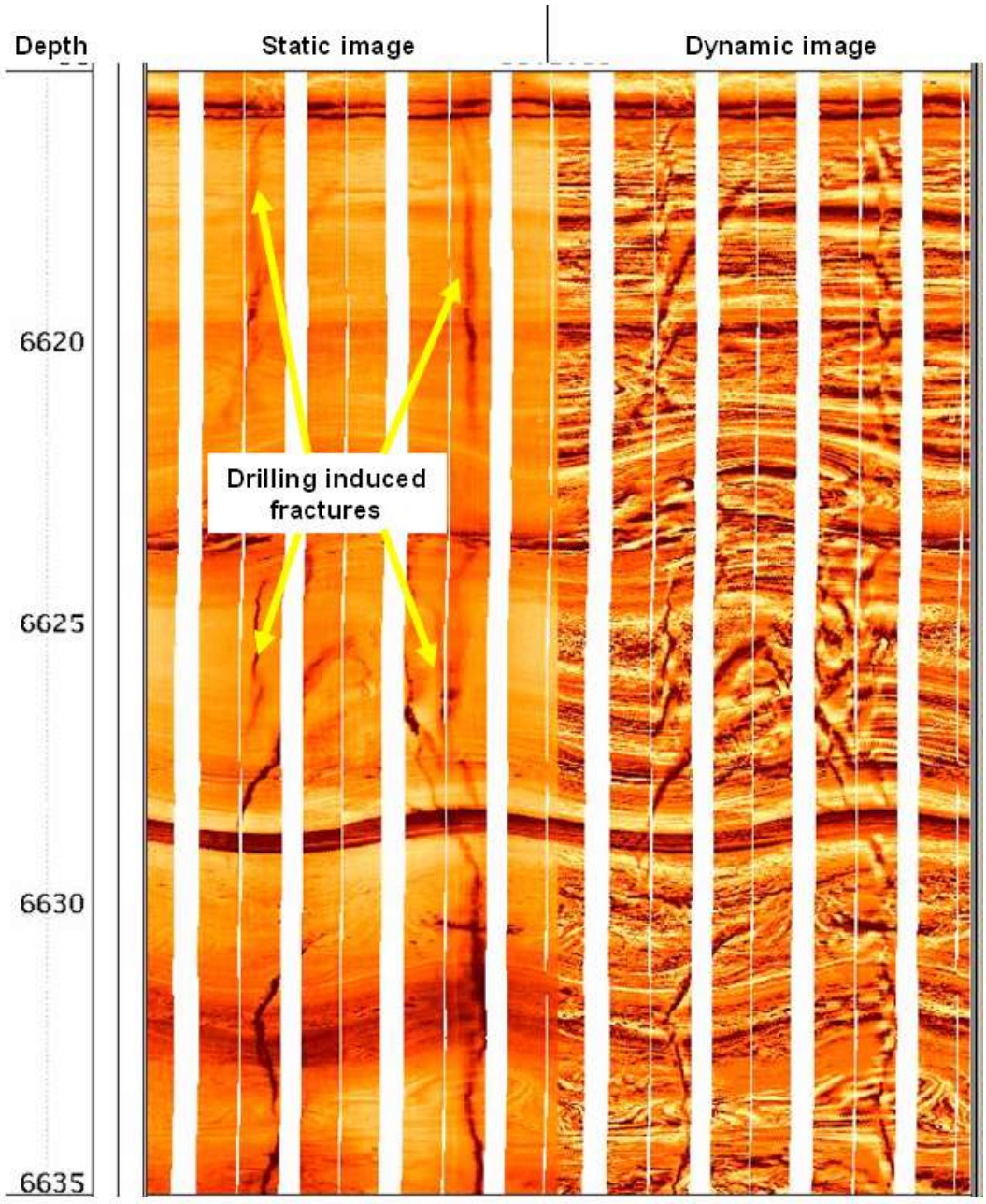

Figure 3.16. An example of drilling induced fractures from RMV 60-17 well. Drilling fluid in the fractures creates resistivity contrast with the adjacent rock. Therefore, these features are seen dark in color. Depth scale is in feet.

in sand bodies and shales, their direction is 90° offset from borehole breakouts and their dip angle is between 80^{o} and 90^{o} (almost vertical).

On the other hand, natural fractures can be either open or healed. Open fractures also have connection to the borehole wall; they are solely developed in sandstoneintervals and can have various orientations with respect to borehole breakouts (Figure 3.17). Sometimes, it was difficult to make a distinction between induced and natural open fractures because the stress orientation has not changed in the geologic history of the Piceance basin. Thus, natural open fractures could have been overprinted with induced fractures. Healed fractures are recognized as light-colored (resistive) sine-wave features with generally low dips (less than 60^{o}) (Figure 3.18). The fact that they are resistive features comes from the phenomena of the infill mineralization of the natural open fractures during geologic history.

Faults (Figure 3.19) show discontinuity between features on the opposite side of the fitted sine waves. They are similar to the scour surfaces in the image logs. Dips of more than 30^{o} helped distinguish them from scours or any other sedimentological features. Microfaults are a subgroup of faults which show offset on the scale of cm (Figure 3.20).

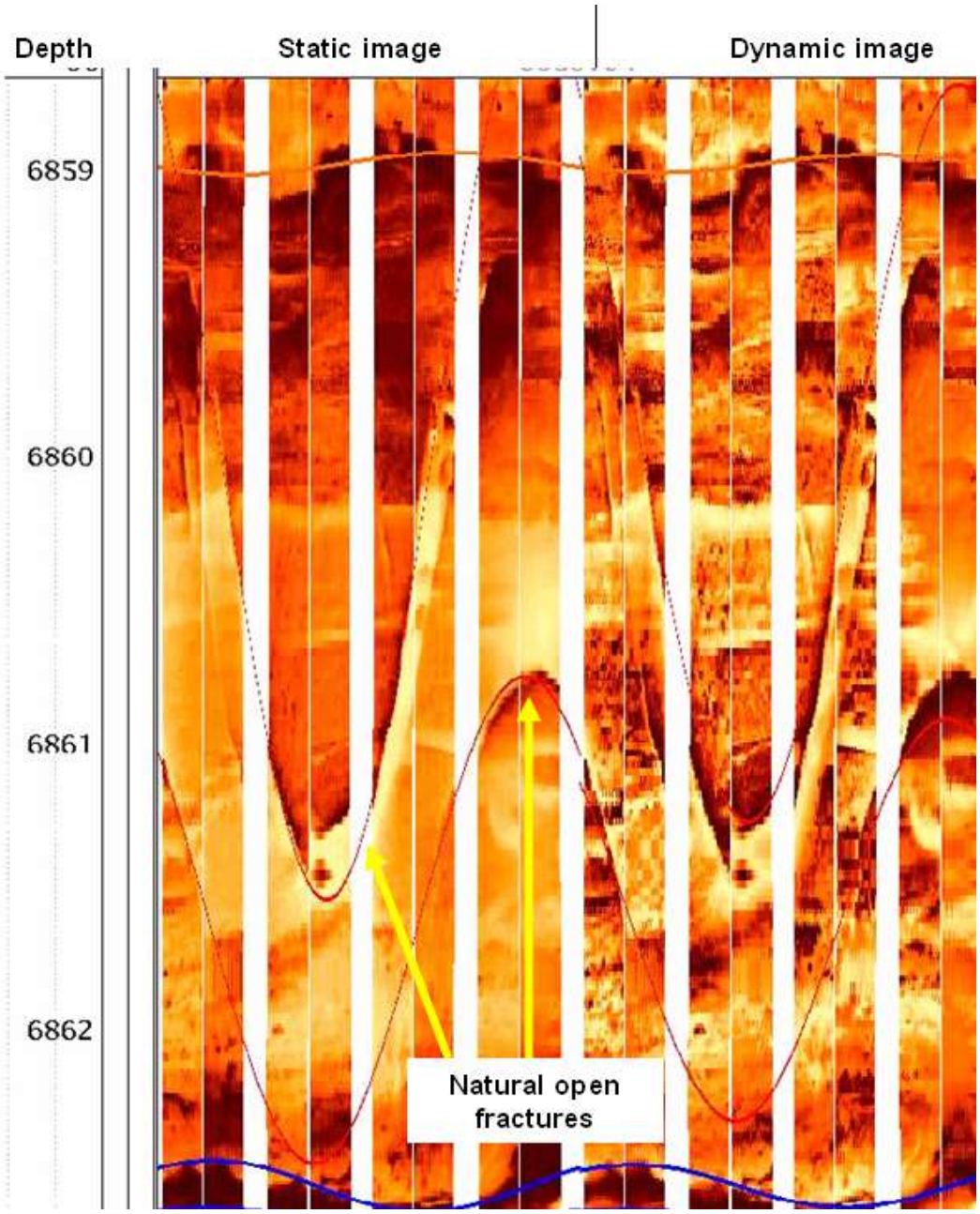

Figure 3.17. An example of open fractures from RMV 60-17 well. Drilling fluid in the fractures creates resistivity contrast with the adjacent rock. Therefore, these features are seen as darker in color. They are solely developed in sandstone intervals. Depth scale is in feet.

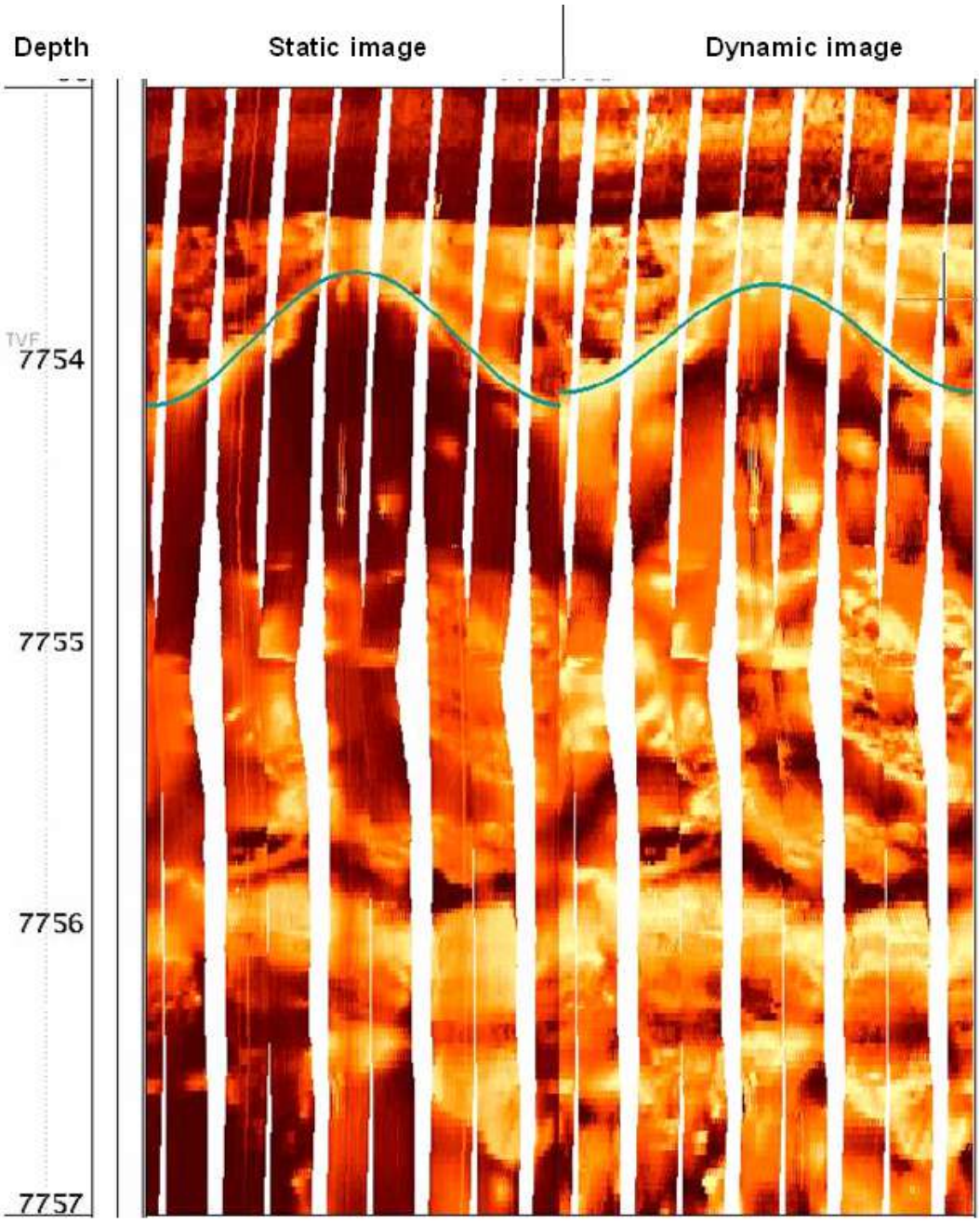

Figure 3.18. An example of a healed fracture from the RMV 60-17 well. Fracture filling is more resistive than surrounding rock and it appears as light-colored sine wave (fitted with blue-green sine wave). Depth scale is in feet.

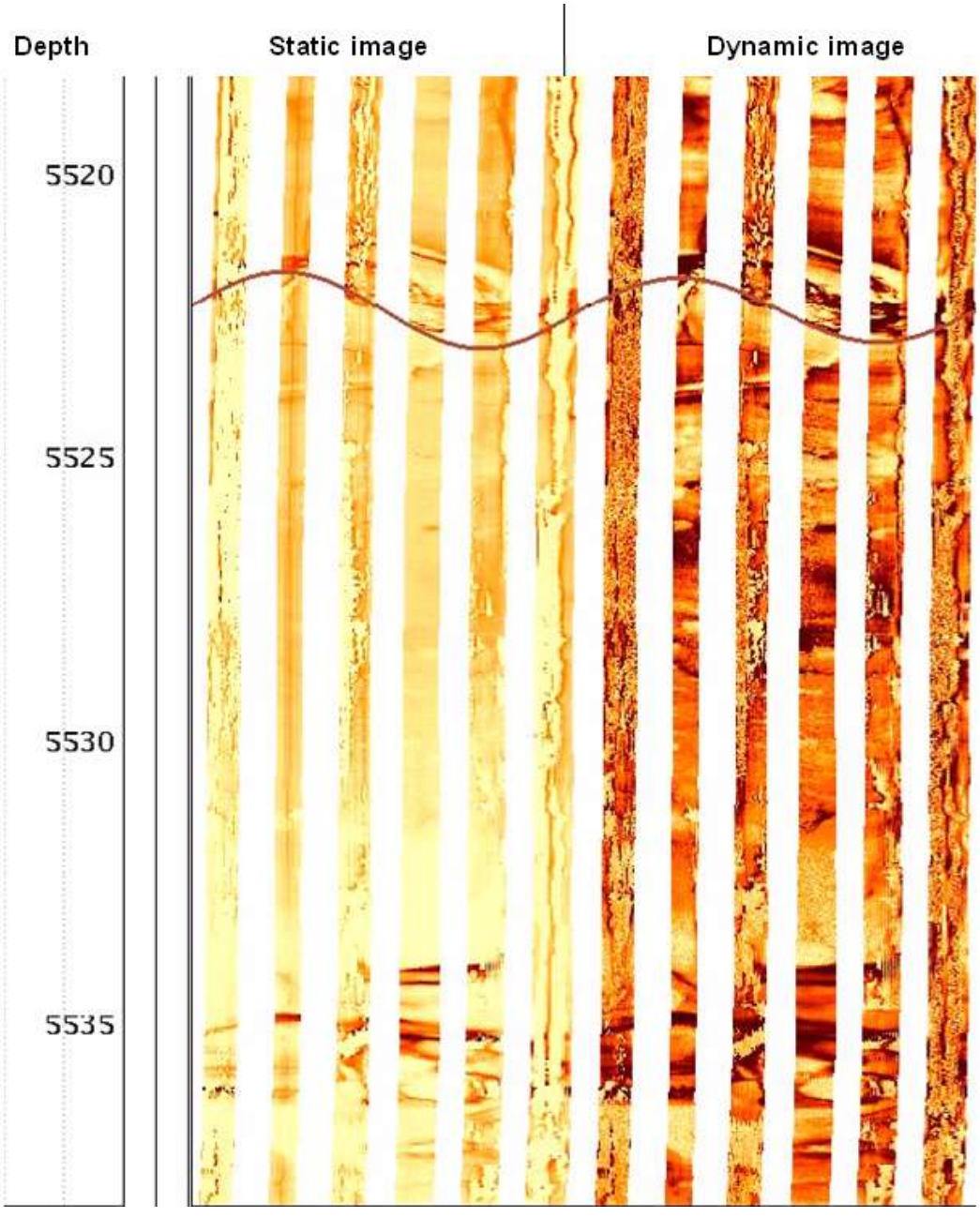

Figure 3.19. An example of fault in the RWF 542-20 well. The brown sine wave represents interpretation of fault surface. Depth scale is in feet.

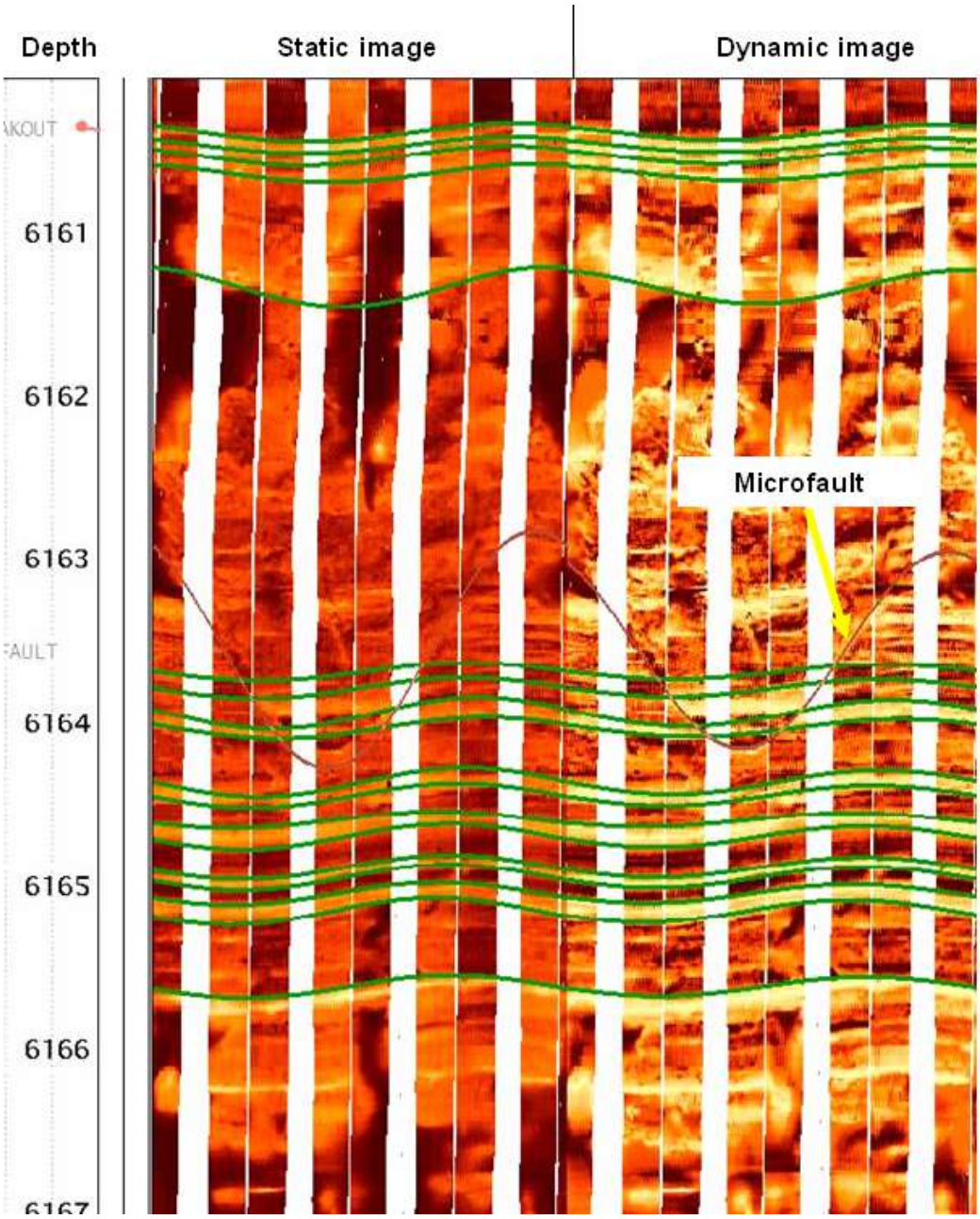

Figure 3.20. An example of microfault in the RWF 523-20 well. The brown sine wave represents interpretation of the fault surface. Notice the vertical offset of approximately 2 in (5 cm). Depth scale is in feet.

CHAPTER 4

PRESENT-DAY STRESS ANALYSIS

Borehole breakouts (Figure 4.1), which form during or shortly after the drilling process, are hole elongations that result from stress concentrations in a nonuniform stress field (Springer, 1987). Breakout elongation is defined in a plane orthogonal to the borehole axis, and it parallels the direction of minimum principal compressive stress (SH_{min}) (Knight, 1999). Breakouts are formed by failure along two pairs of conjugate shear fractures, which form tangential to the borehole circumference (Figure 4.2). An elongation points to the direction of SH_{min} (Zheng et al., 1989).

Induced fractures tend to form parallel to the maximum horizontal stress field, i.e., parallel to SH_{max} (±30°) (Figure 4.3). They occur when the drilling pressure and mud weight exceed the least compressive stress and the wellbore undergoes tensile failure. Figure 4.4 illustrates the relationship of the borehole breakout and drilling induced fracture orientations in a borehole.

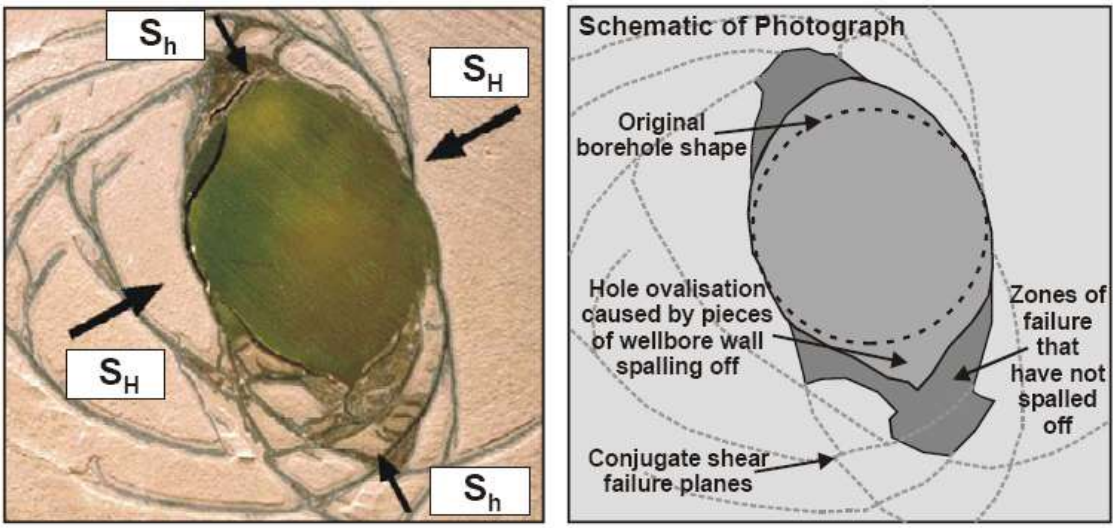

Figure 4.1. Results of a hollow cylinder lab test simulating borehole breakout. Intersection of conjugate shear failure planes results in enlargement of the cross-sectional shape of the wellbore. SH and Sh refer to the orientations of maximum and minimum horizontal stress, respectively. Reinecker et al., (2003).

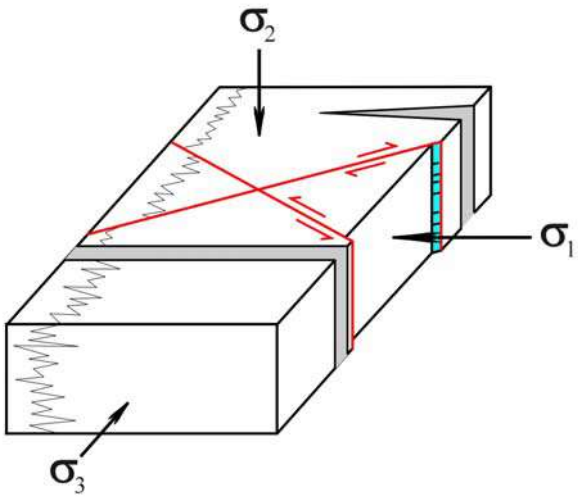

Figure 4.2. Breakouts are formed by failure along two pairs of conjugate shear fractures, which form tangential to the borehole circumference. Abbreviations: σ_1= maximum stress, σ_3= minimum stress, σ_2= intermediate stress.

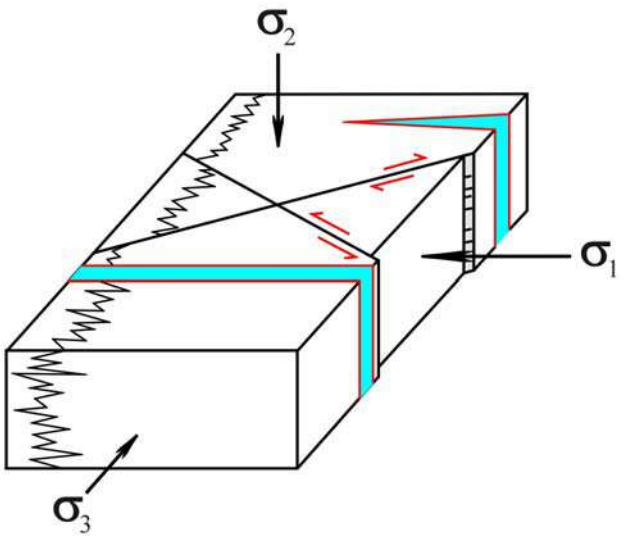

Figure 4.3. Fractures (blue) open parallel to σ_{hmax}. Abbreviations: σ_1= maximum stress, σ_3= minimum stress, σ_2= intermediate stress.

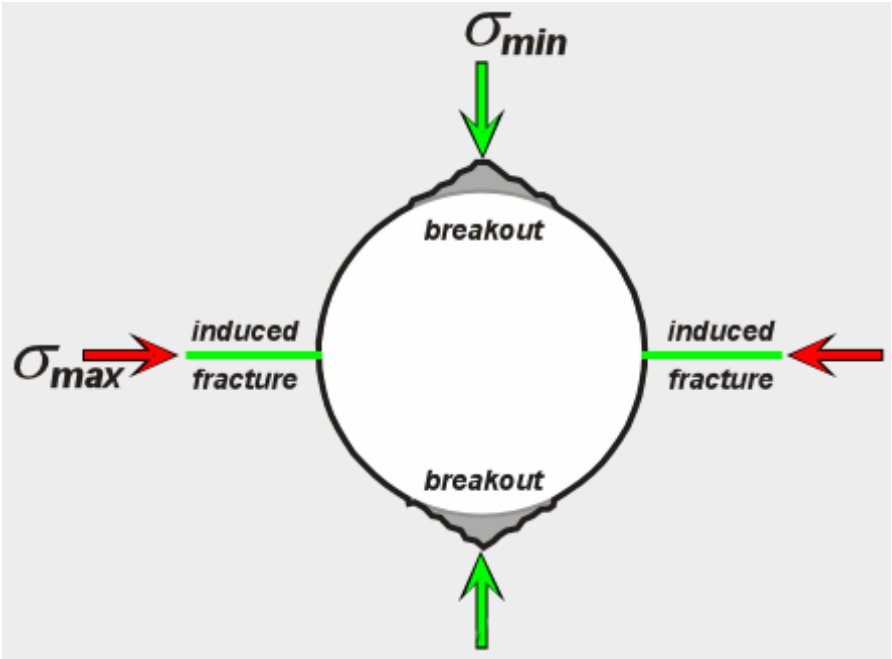

Figure 4.4. Wellbore-perpendicular cross section shows breakouts, induced fractures, maximum and minimum present-day stress field. (From www.naturalfractures.com).

4.1. Regional Tectonic Stress and Fracture Orientation

The tectonic evolution of the Piceance basin indicates that basement faulting, produced by extensional tectonics during the Precambrian and Pennsylvanian, and from Laramide compressional tectonics (southwest directed shortening), has influenced the structural anisotropy, state of stress, and major fault system in the basin (Kuuskraa et al., 1997). A basement structure reactivated during southwest-directed regional shortening generated the dominant regional deformation and structures in the southeastern basin, including the subtle Rulison anticline and the main fault and fracture systems (Kuuskraa et al., 1997). Uplift and slight west-northwest and east-west compression has affected the basin during the Holocene to present (Kuuskraa et al., 1997).

Figure 4.5 shows the present-day stress orientation in Rulison area from the World Stress Map Project (Reinecker 2005). Koepsell et al. (2003) stated that in the southern part of the Piceance basin, maximum principal stress orientation varies from ENE to ESE. Variations in maximum principal stress orientation in vertical wells were determined from borehole image logs.

Several authors studied the fracture orientation in the region. Lorenz and Finley (1991) stated that the natural fractures have a west-northwest or east-west regional orientation oblique to the production trends (northwest).

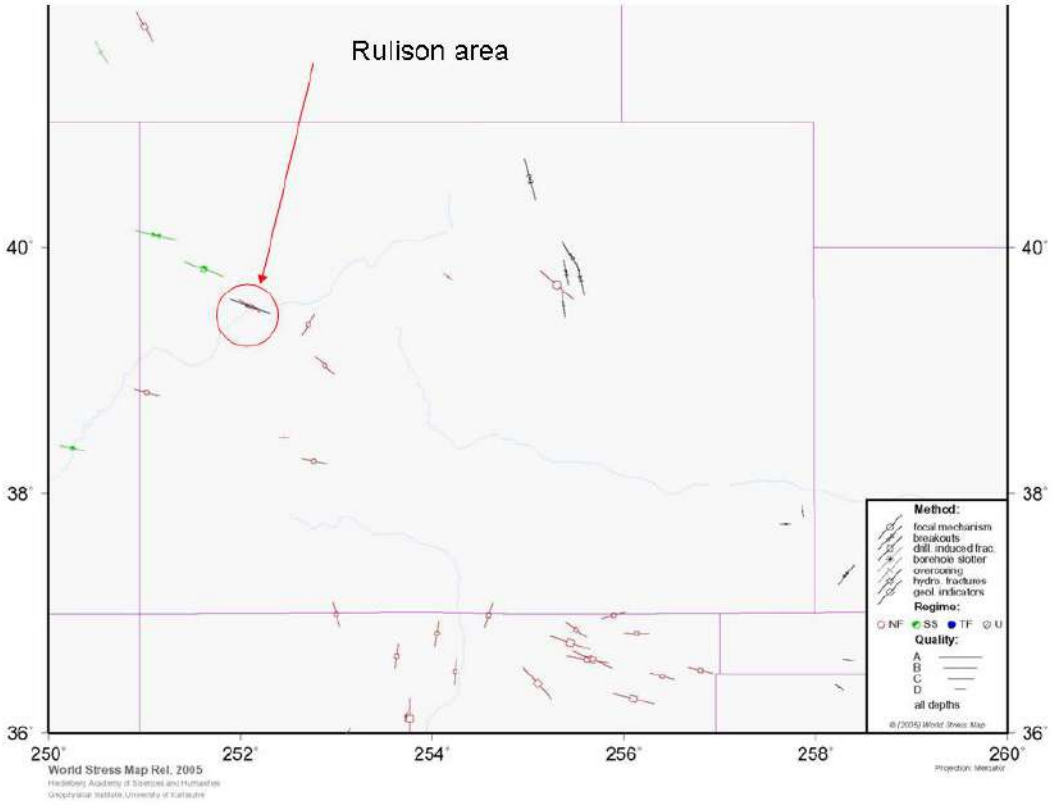

Figure 4.5. Present-day stress orientation in the area of Rulison field. Stress map of Colorado State, modified from Reinecker et al. (2005).

Kuuskraa et al. (1997) noticed a series of N30W and N60E fractures prominent in Rulison field. The N30W and N60E subvertical fracture orientations are associated with larger-scale faults, joints, and fractures that enhance permeability. Kuuskraa et al. (1999) described a regionally pervasive system of fluid and stress induced micro-fractures, oriented N80^{o}W at the MWX site, that provide matrix permeability in sand bodies of a few micro-darcies.

Lorenz (2003) interpreted the natural fracture system in the Piceance basin. Fractures strike parallel to the principal maximum stress orientation, with strikes varying between WNW-ESE and WSW-ENE.

Gomez et al. (2003) examined fractures on the microfracture (fractures observed with magnification more than 10x) and macrofracture (observed with unaided eye) level. The dominant microfracture strike, which coincides with macrofractures, was west-northwest. Some subsets of the microfracture data suggested that subsidiary northwestward and northeastward trends were also present.

Published natural fracture orientations can be summarized into three main orientations. Generally, an E-W extensional fracture set is parallel to the maximum present-day stress, which in the Piceance basin locally varies from WNW-ESE to WSW-ENE. The second set shows strikes of N30^{o}W, roughly parallel to the main structural and production trend. The third set of natural fractures has N60^{o}E strikes.

4.2. Methods of Analysis

First, in situ stress orientations were determined by borehole breakout analysis of caliper logs. Second, those results were compared with borehole breakouts interpreted in image logs.

4.2.1. Caliper Logs

In situ stress orientations were determined by borehole breakout analysis of oriented four (FMI) and six (EMI) armed caliper logs. The following steps were performed for each well in order to identify breakout zones at Rulison field:

1) Numeric log data (C13, C24, C36, DEVI, HAZI, P1AZ) were resampled to a one-foot interval.

2) Intervals for which the logging tool was freely rotating were removed from the data set. This was determined from plots of the P1AZ curve, where the curve was changing and not stabilized.

3) Intervals for which elongation was equal or less than 0.25 in (0.63 cm) were viewed as zones of "NO ELONGATION" and were eliminated from the data set. This was determined by looking at the difference between C13, C24 (and C36).

4) WASHED-OUT ZONES were eliminated from the data set. A washout is the zone for which the smallest caliper is 1 in (2.5 cm) or more larger than the bit size.

5) Intervals for which elongation might have been due to MECHANICAL KEYSEATING were eliminated from the data set. Keyseats were detected by comparing P1AZ to HAZI. If any value of P1AZ was within +- 10^o of HAZI, or a 90^o (60^o) increment of HAZI, the zone was eliminated as a possible keyseat. This is because elongation is in the direction of the hole azimuth.

6) Elongations remaining after this process of elimination were identified as breakouts and classified as to whether C13, C24 (or C36) were the directions of elongation. The present-day maximum horizontal in situ stresses (sH max) were defined as those orientations perpendicular to the borehole elongation direction (Figures 4.6 to 4.9).

4.2.2. Image Logs

The resistivity images enable the identification of borehole breakouts. In images, they are seen as two parallel dark lines, separated by 180^o (Figure 4.10).

Induced fractures, which are caused by drilling processes, are always open and have connections to the borehole wall. As mentioned above, they are oriented parallel to the SH_{max} orientation, or 90^o from breakouts (Figure 4.11). They form along the whole

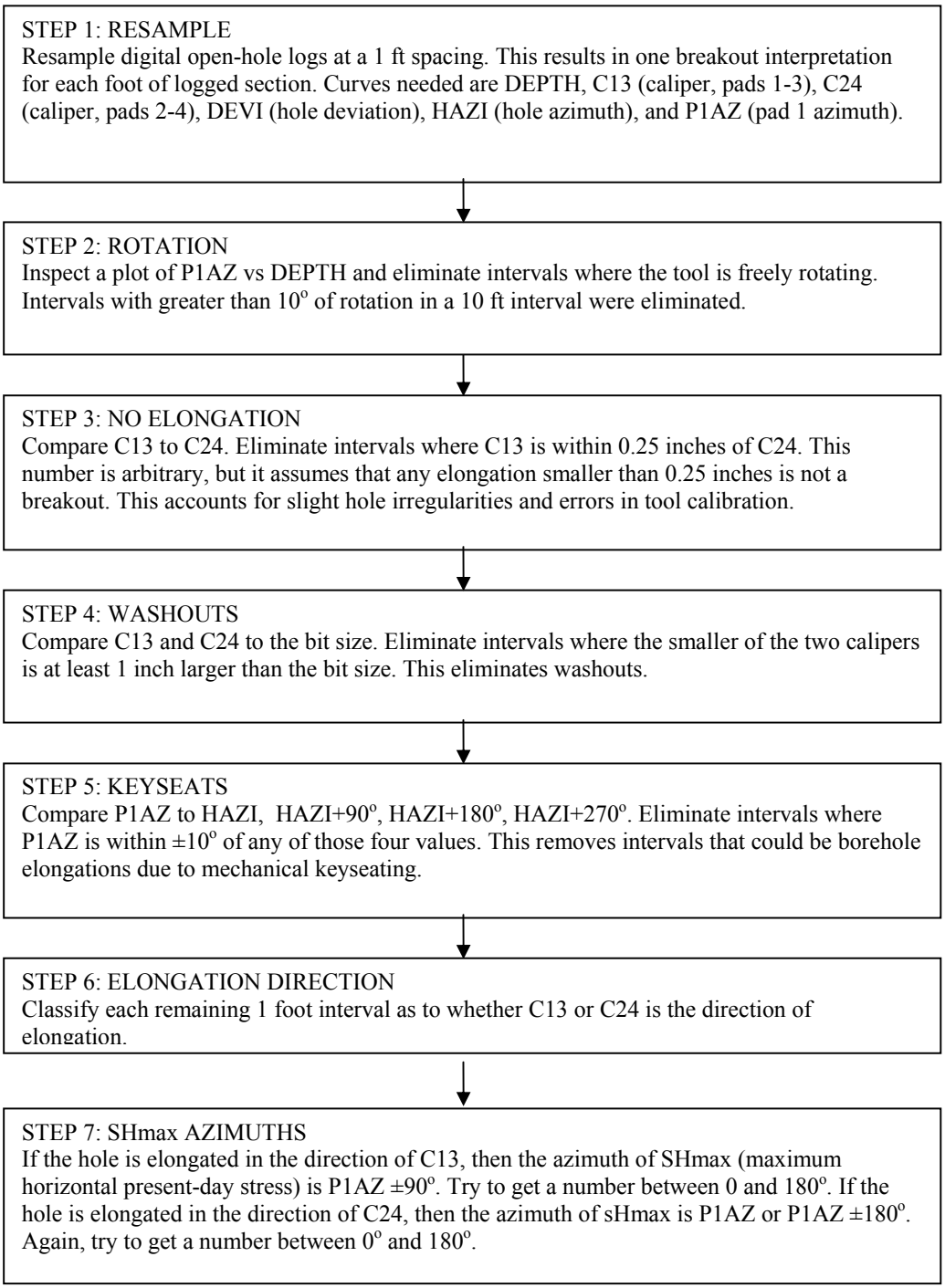

Figure 4.6. Flow chart shows the procedure used for borehole-breakout interpretation with 4-arm calipers.

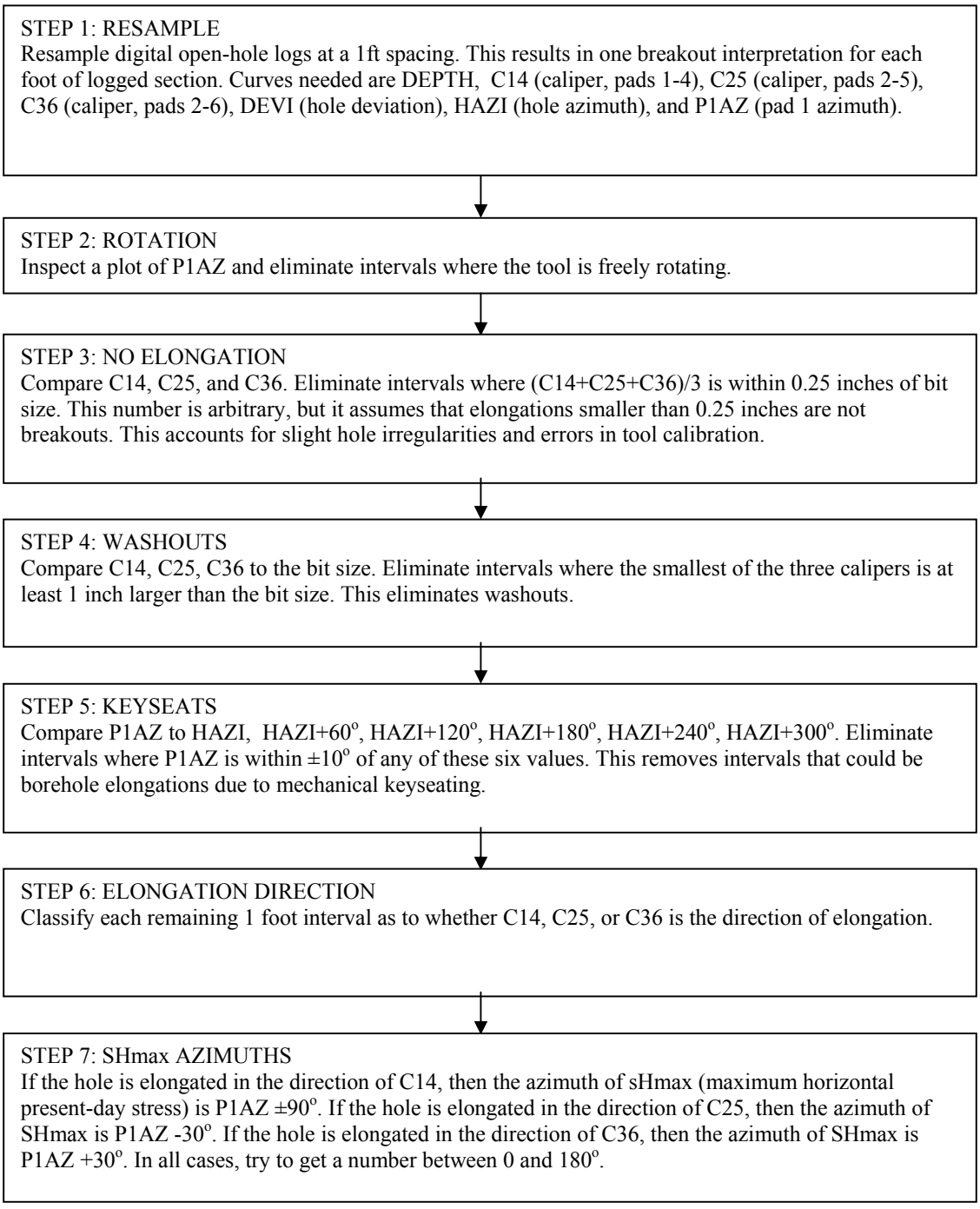

Figure 4.7. Flow chart shows the procedure used for borehole-breakout interpretation with 6-arm calipers.

Case 1: in gauge hole
with no breakout.

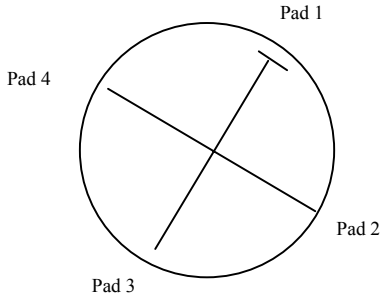

Case 2: Hole with breakout in the C13
direction. SHmax = P1AZ ±90$^{o.}$

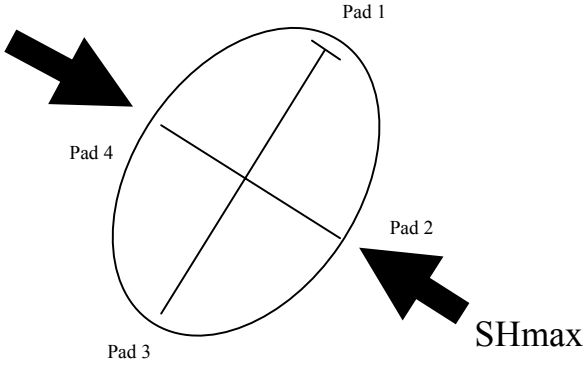

Case 3: Hole with breakout in the C24
direction. SHmax = P1AZ ±180^{o}

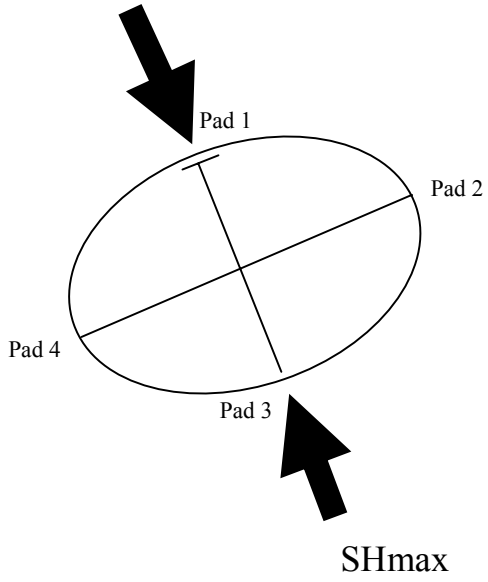

Figure 4.8. Schematic diagram shows how to determine the orientation of maximum horizontal in situ stress (SHmax) from elongation direction and pad 1 azimuth (P1AZ) for the 4-arm dipmeter.

Case 1: in gauge hole with no breakout.

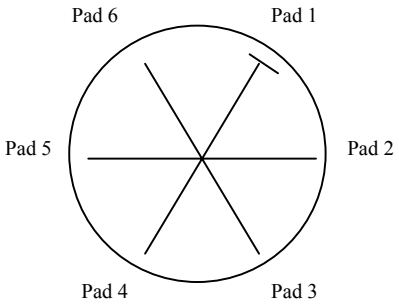

Case 2: Hole with breakout in the C14 direction. SHmax = P1AZ ±90°.

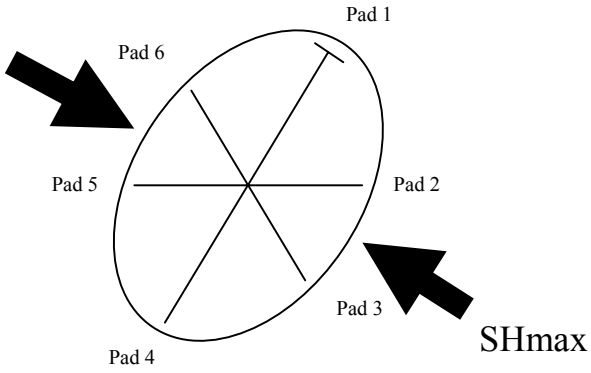

Case 3: Hole with breakout in the C25 direction. SHmax = P1AZ -30°.

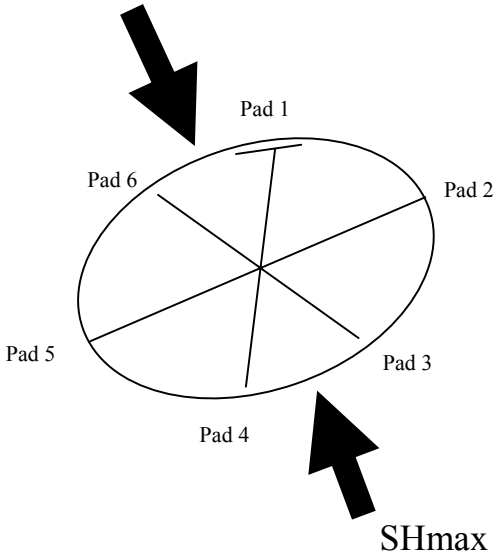

Case 4: Hole with breakout in the C36 direction. SHmax = P1AZ + 30°.

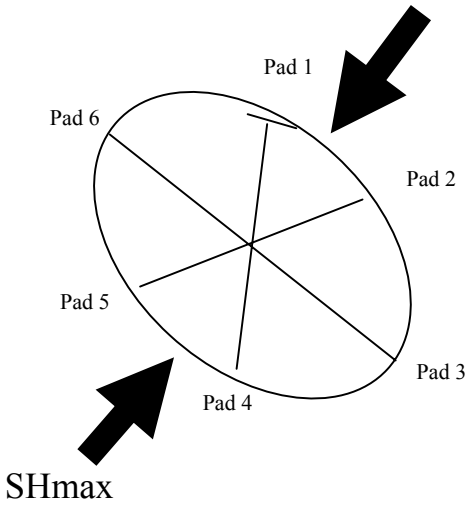

Figure 4.9. Schematic diagram shows how to determine the orientation of maximum horizontal in situ stress (SHmax) from elongation direction and pad 1 azimuth (P1AZ) for the 6-arm dipmeter.

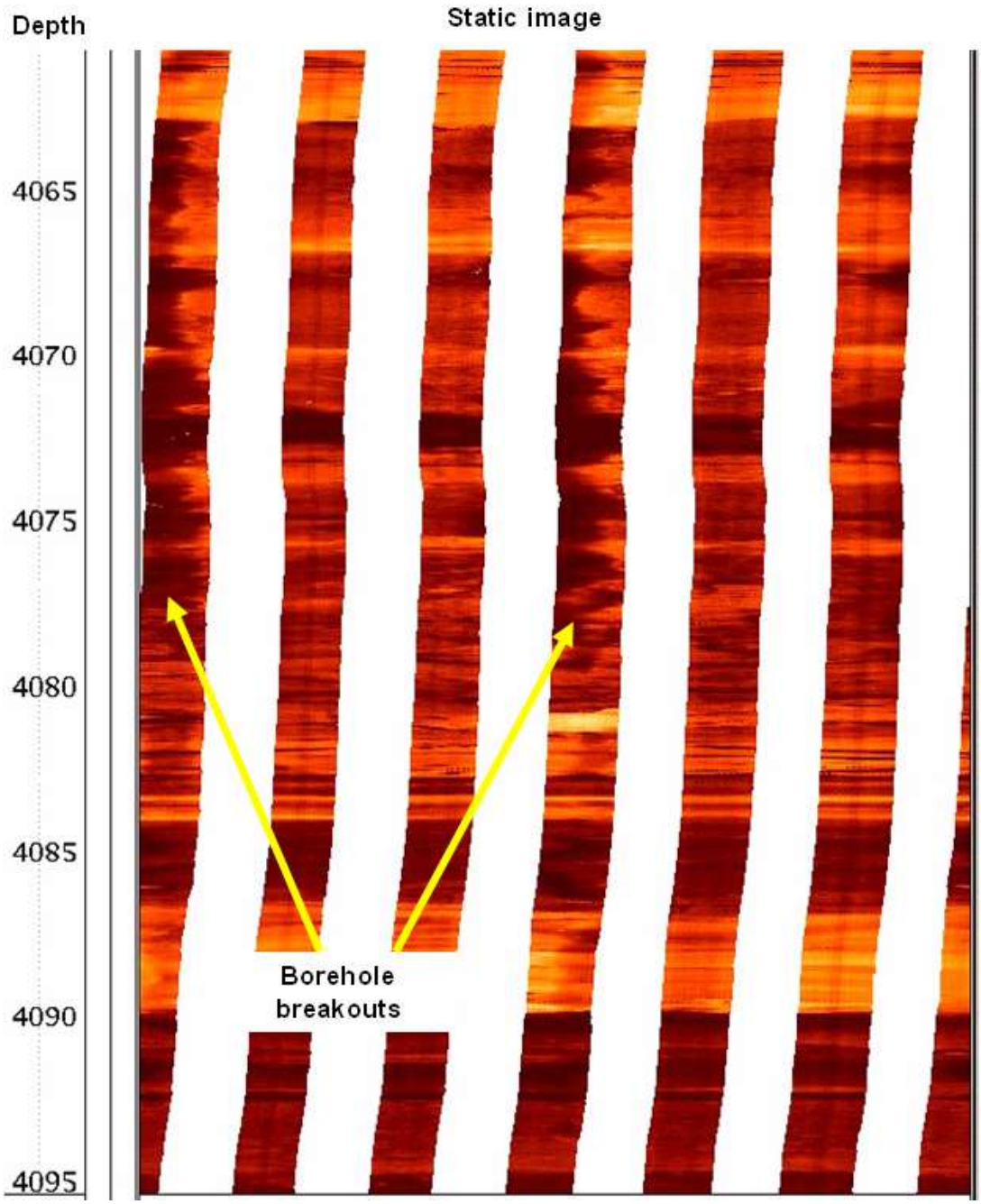

Figure 4.10. An example of borehole breakout from the RWF 542-20 well. Note two parallel dark lines, separated by 180^{o}. Depth scale in feet.

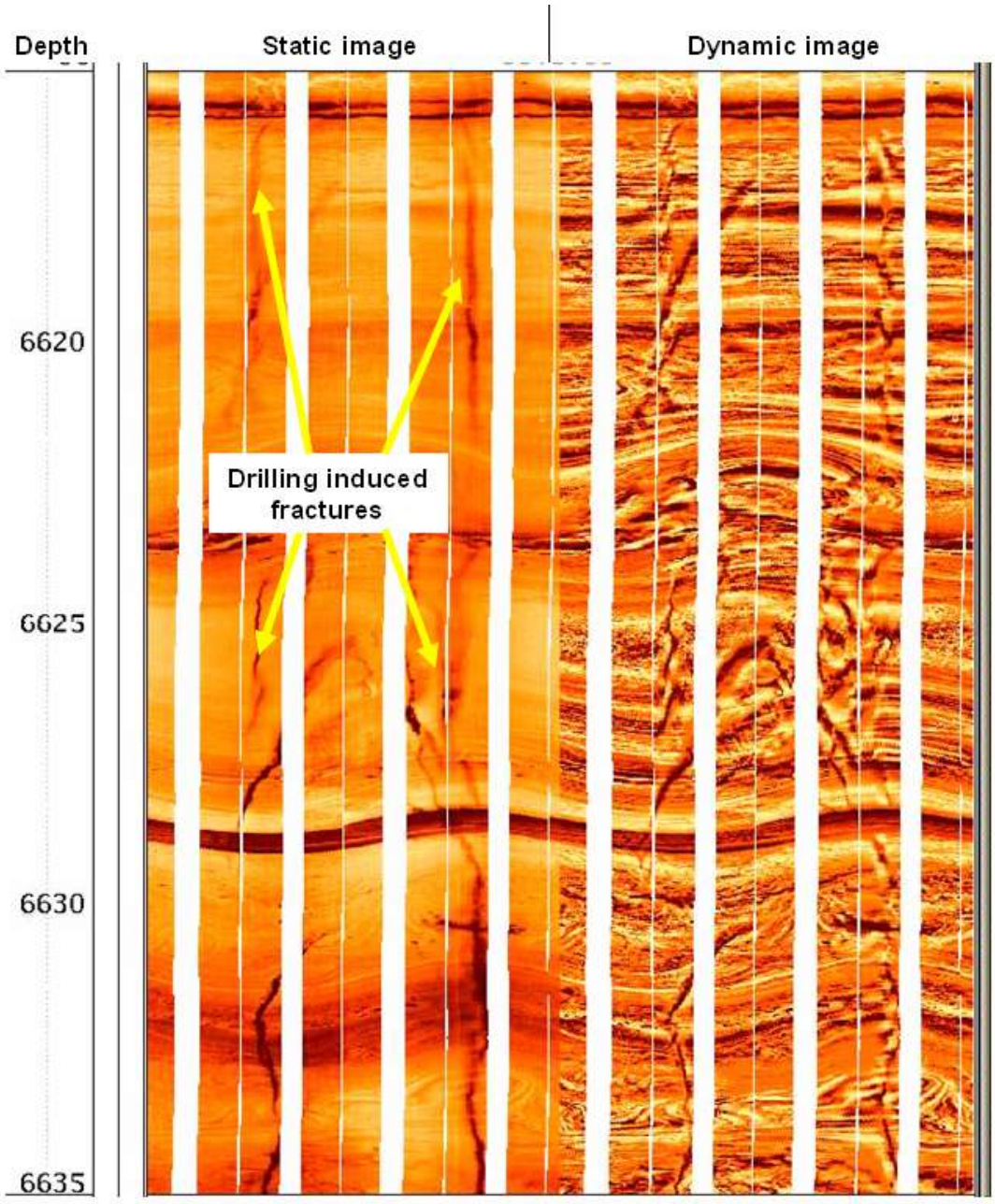

Figure 4.11. An example of drilling induced fractures from RMV 60-17 well. Drilling fluid in the fractures creates resistive contrast with the adjacent rock. Therefore, these features are seen dark in color. Depth scale is in feet.

interval, crossing shale sand boundaries. Their dip angle is nearly 90^{o}, that is, almost vertical. Strike azimuth rose diagrams for borehole breakouts and drilling induced fractures were computed to determine the maximum stress orientation.

4.3. Results

Figures 4.12 to 4.14 show the diagrams of GR vs. azimuth plots of SHmax interpreted both from caliper and image logs. Figures 4.15 to 4.17 show the rose diagrams for strike azimuth of induced fractures and SHmax for borehole breakouts in the 3 wells. The mean direction of SHmax is roughly EW. The direction of induced fractures has 90^{o} offset and they confirm the same SHmax orientation.

In the RWF 542-20 well, caliper interpreted breakouts do not show a depth match with those interpreted in the images. On the other hand, there is a good match in SHmax orientation for the different depths. The RWF 523-20 well has a good match of the three breakout intervals in the image and caliper logs. There are six breakouts in the RMV 60-17 well, confirmed with image and caliper interpretation. Excel tables and all results of interpretation are shown in Appendix B.

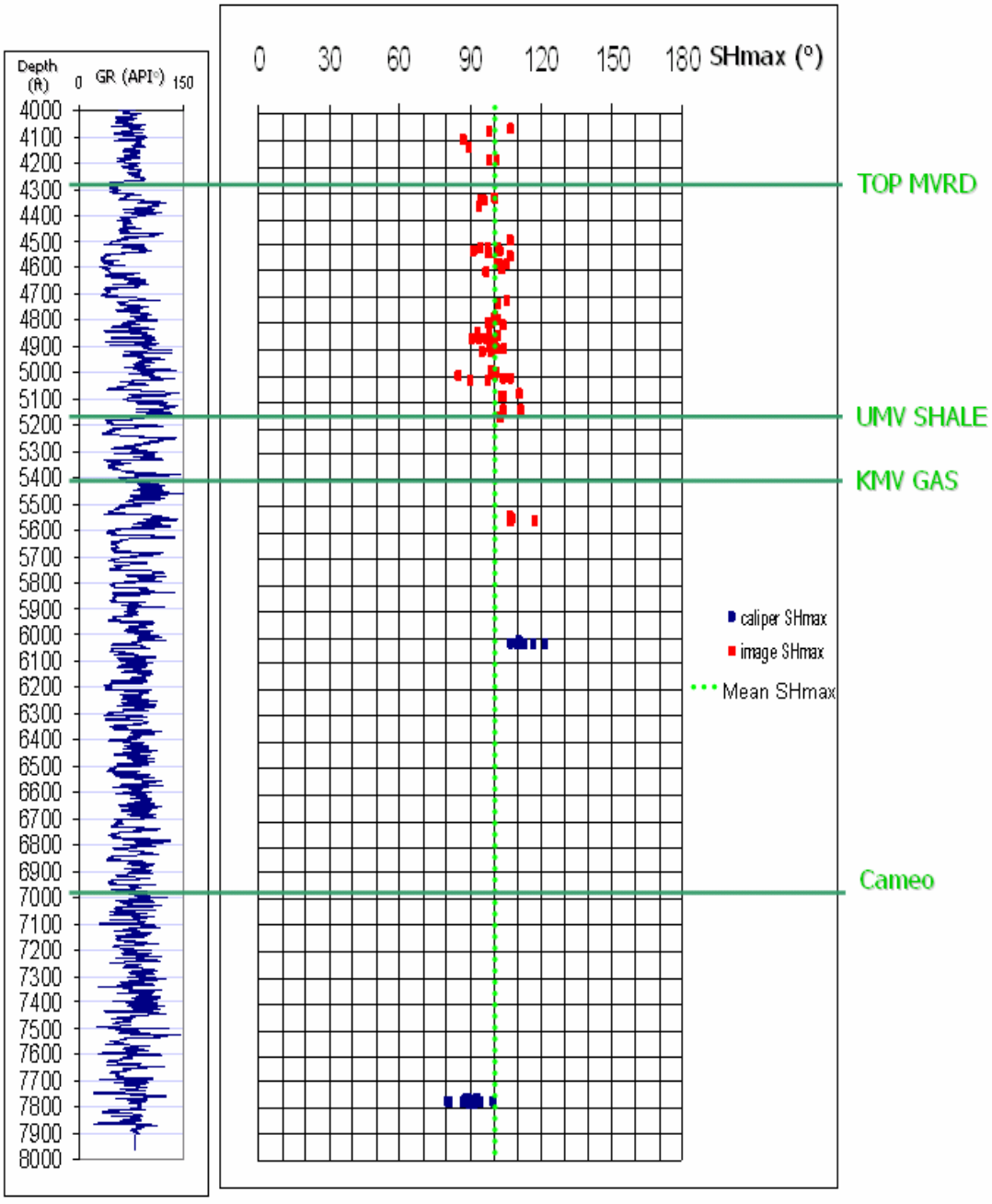

Figure 4.12. Logs of GR of the imaged interval and breakouts in the RWF 542-20 well. Both caliper and image log interpretations of SHmax are shown. Mean SHmax is 102°. Depth scale is in feet.

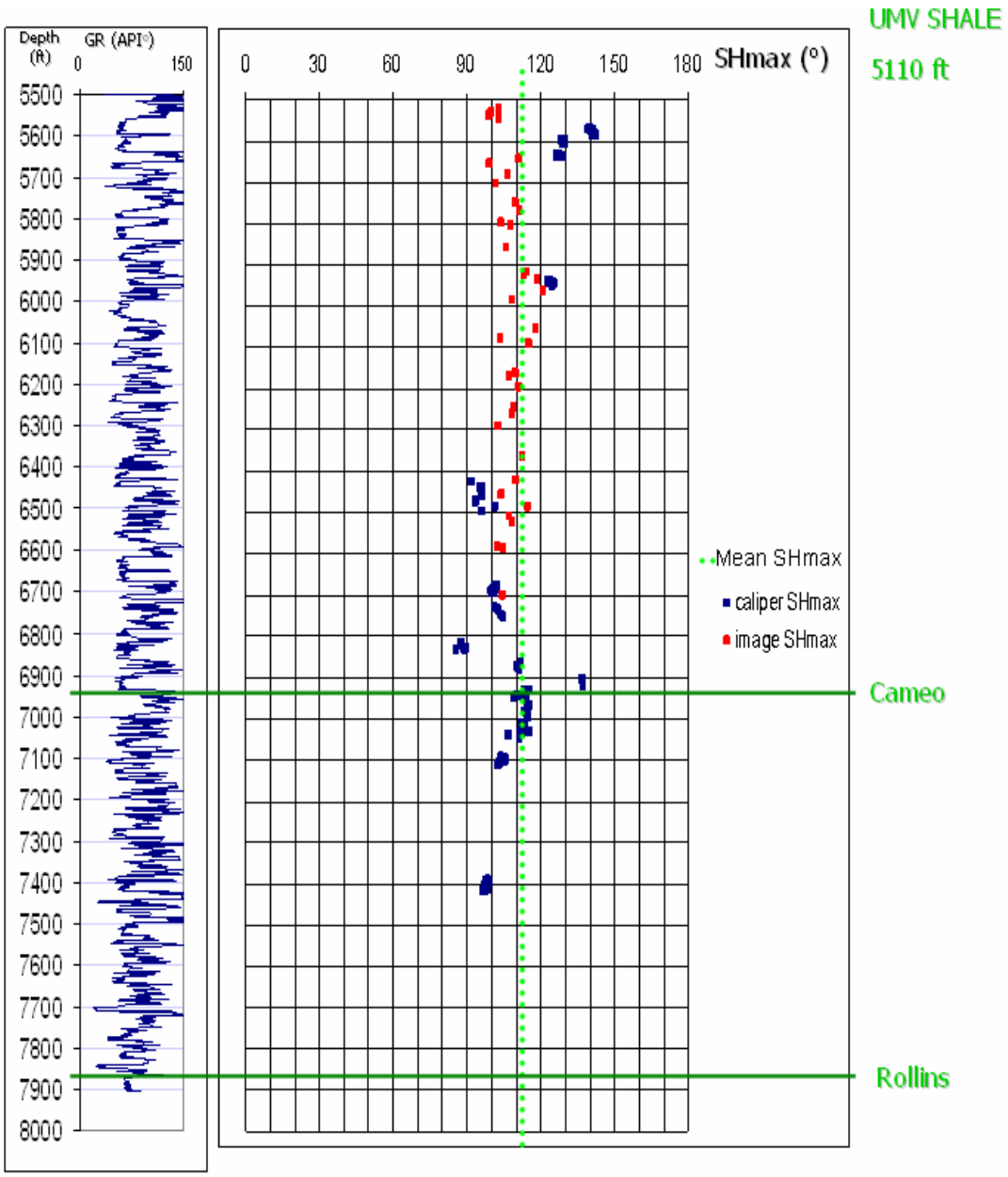

Figure 4.13. Logs of GR of the imaged interval and breakouts in the RWF 523-20 well. Both caliper and image log interpretations of SHmax are shown. Mean SHmax is 112°. Depth scale is in feet.

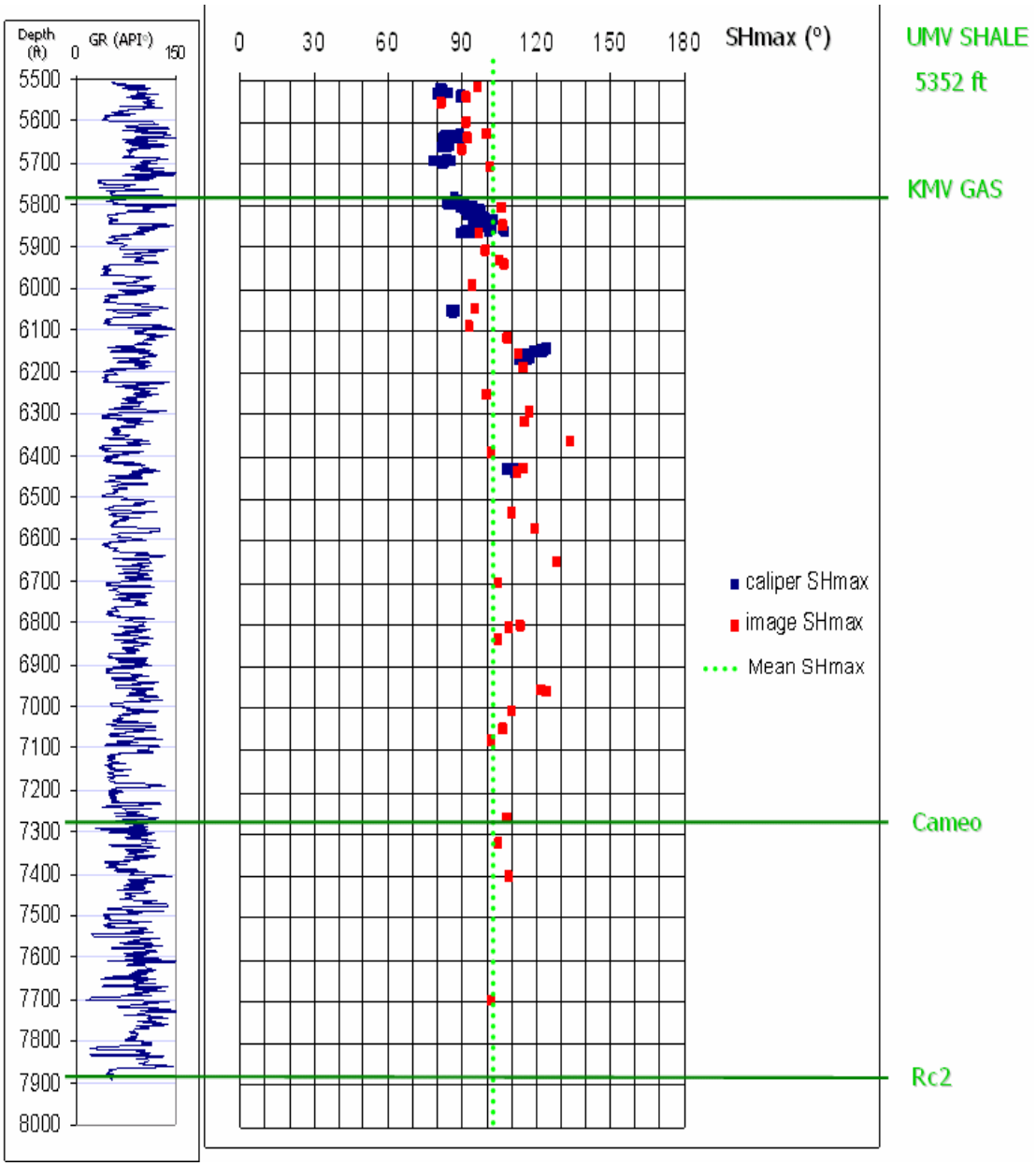

Figure 4.14. Logs of GR of the imaged interval and breakouts in the RMV 60-17 well. Both caliper and image log interpretations of SHmax are shown. Mean SHmax is 101°. Depth scale is in feet.

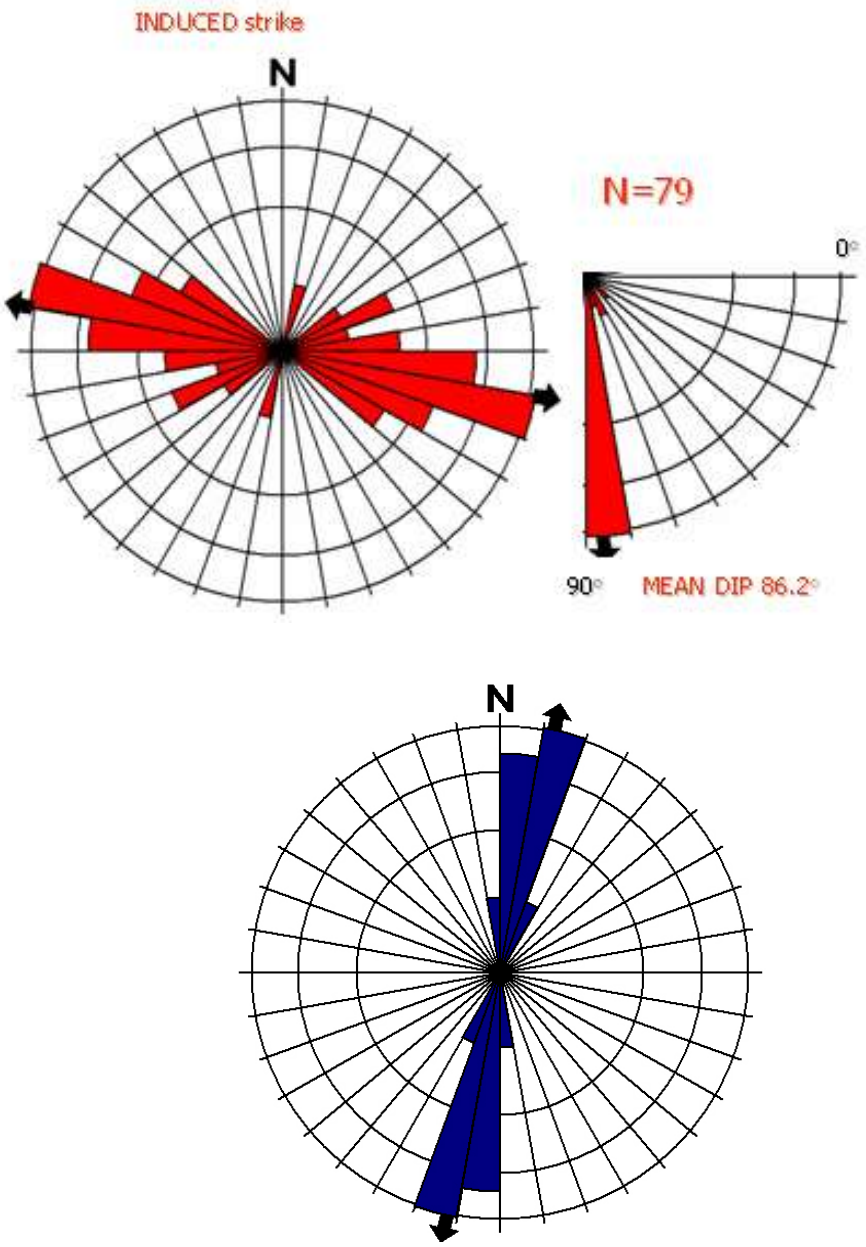

Figure 4.15. Rose diagrams (in red) of drilling induced fractures and breakouts (in blue) in the RWF 542-20 well (strike=left, dip=right). There is a dominant set of fractures with 110^{o} of strike azimuth. Number of induced fractures=79. Mean dip shows value of 86.2^{o}. Breakouts have mean strike of 10.6^{o}. Number of breakouts=63.

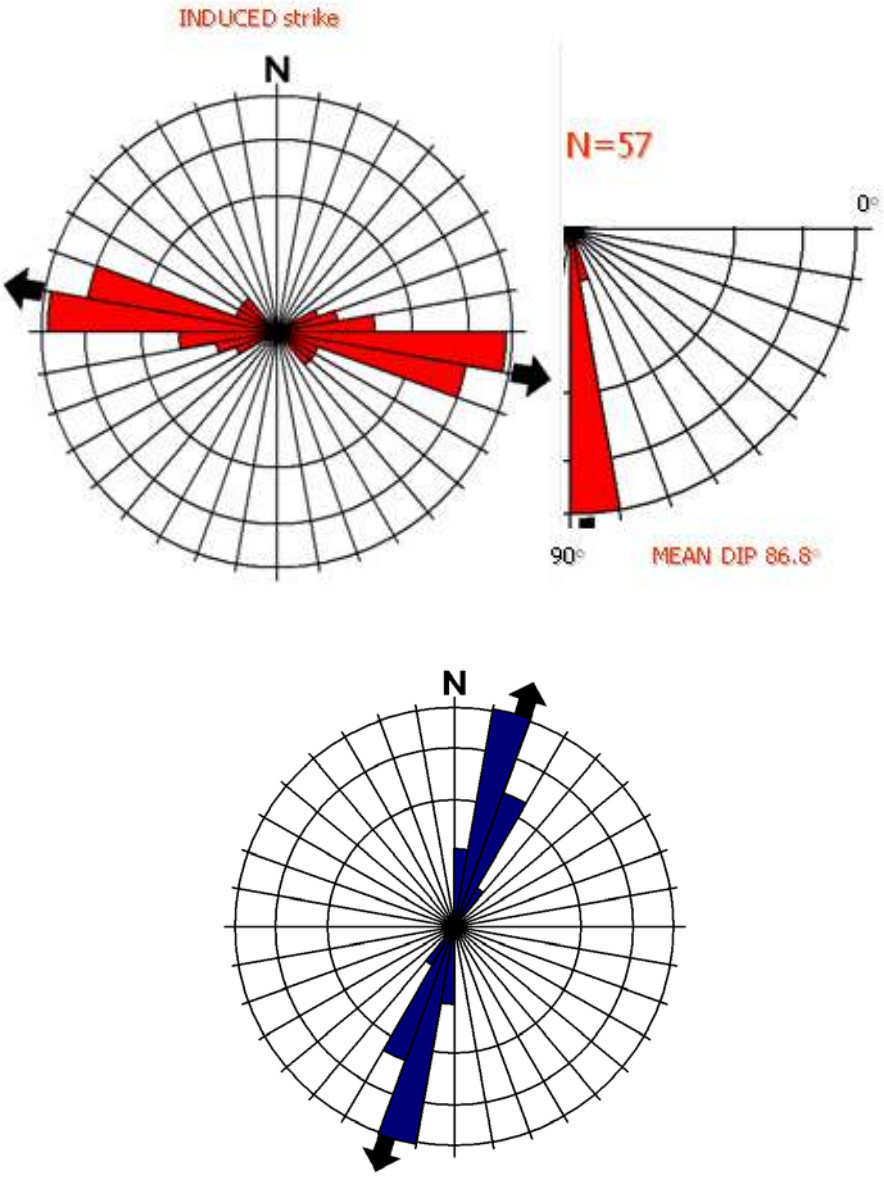

Figure 4.16. Rose diagrams (in red) of drilling induced fractures and breakouts (in blue) in the RWF 523-20 well (strike=left, dip=right). There is a dominant set of fractures with 110^{o} of strike azimuth. Number of induced fractures=57. Mean dip shows value of 86.8^{o}. Breakouts have mean strike of 17.8^{o}. Number of breakouts=38.

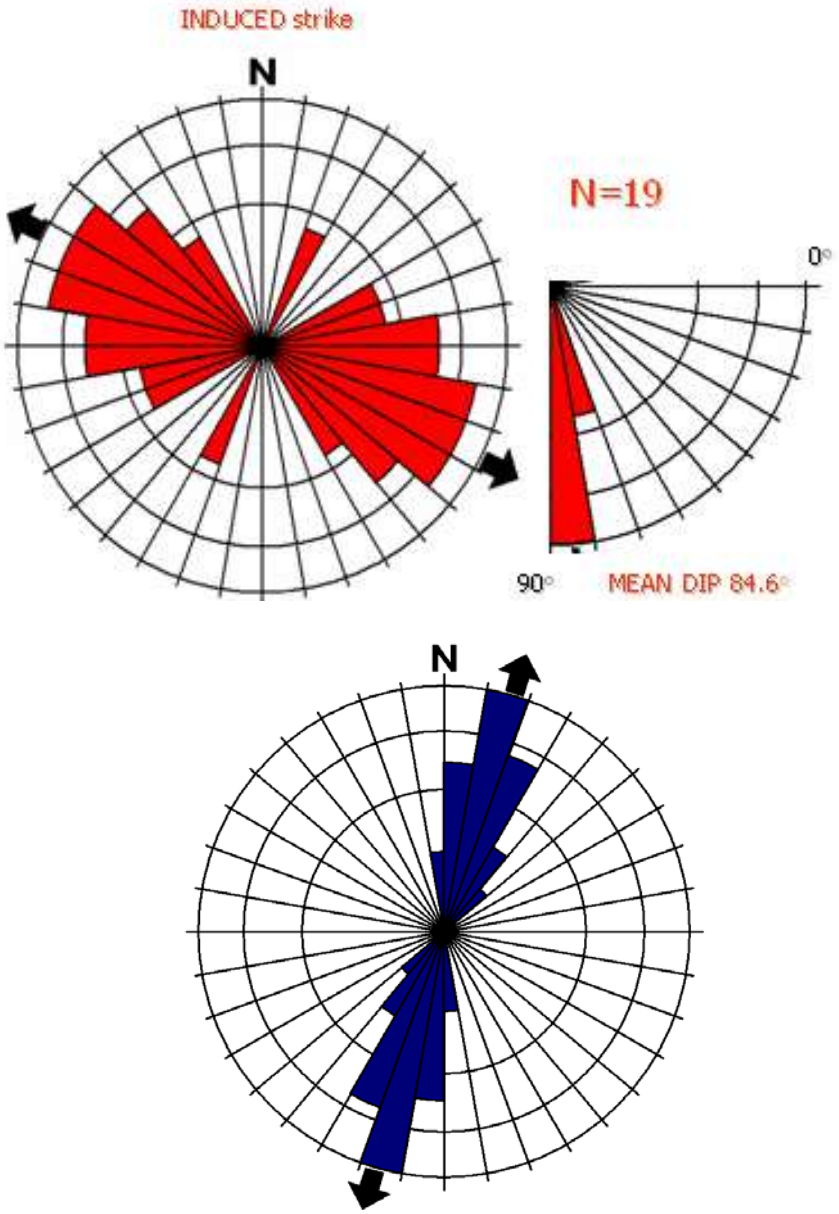

Figure 4.17. Rose diagrams (in red) of drilling induced fractures and breakouts (in blue) in the RMV 60-17 well (strike=left, dip=right). There is a dominant set of fractures with 117^{o} of strike azimuth. Number of induced fractures=19. Mean dip shows value of 84.6^{o}. Breakouts have mean strike of 16.4^{o}. Number of breakouts=45.

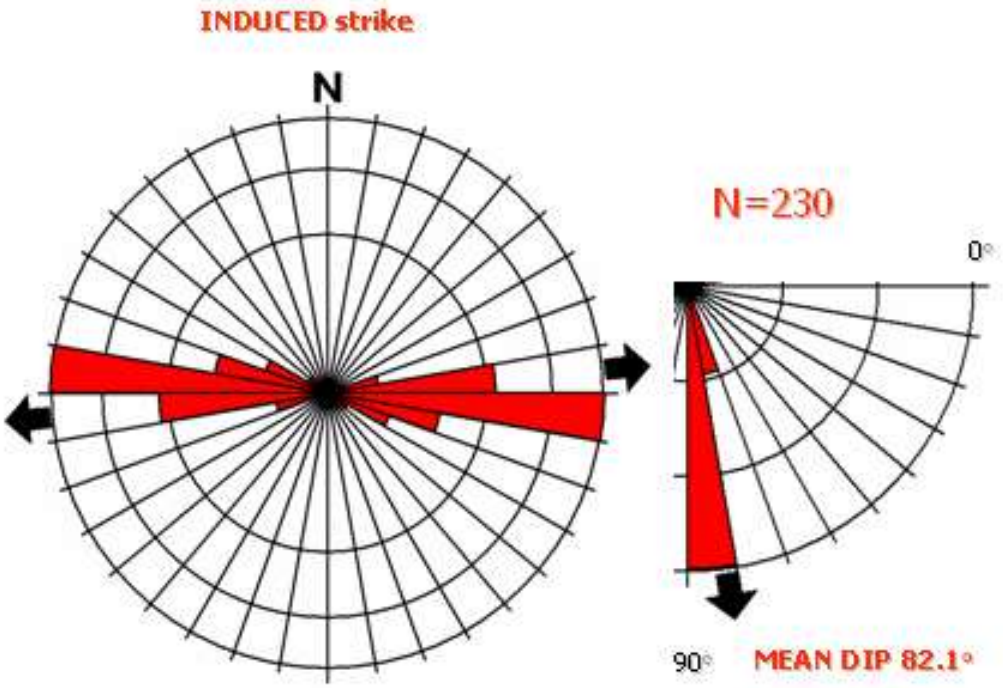

Figure 4.18. Rose diagrams of drilling induced fractures in the RWF 441-20 well (strike=left, dip=right). There is a dominant set of fractures with 95^{o} of strike azimuth. Number of induced fractures=230. Mean dip shows value of 82.1^{o}.

4.4. Discussion

Breakouts in the image logs were dominantly present in the shaly sandstone intervals. The explanation for that phenomenon might be due to the brittle nature of rocks which contain shales. Clean sandstones, on the other hand, are relatively more resistant rocks where breakouts were absent.

Generally, image and caliper breakouts show a good match, although there are some differences. There are a few possible reasons for the discrepancy between image and caliper breakout interpretations. The first reason is the lack of reliable bit-size information in the wells. Some of the caliper-interpreted breakouts might be filtered as washouts, in case the effective bit size was too small. On the other hand, in case that bit size was too large, the interval might not be labeled as a borehole breakout. The second reason for the discrepancy is the imperfection of image log interpretation. Some of the breakouts might not be visible because of the pull of the tool, washout zones where pads have poor contact to the borehole wall, processing problems, or gas presence which obscures any feature encountered in the well.

Open natural fractures show the same strike orientation. Because of that it was, in some cases, difficult to discern between induced and open fractures. The open natural fractures are solely developed in the sandstones and this was the main criteria for their recognition (Chapter 5).

All of the interpreted SHmax and induced fractures correspond well with the previous published work in the Piceance basin (Koepsell et al., 2003; Reinecker et al., 2005). Their strike is generally E-W with variations from ENE to ESE.

CHAPTER 5

FRACTURE ANALYSIS

Natural fractures in this study are represented by two major groups: open and resistive fractures. The open fractures are easily seen as dark sine waves on resistivity images. The resistive fractures are seen as bright sine waves because they contain more resistive infill material than the surrounding rock.

5.1. Methods

To interpret a fracture, one fits a sine wave of the feature on the static or dynamic image. Every picked sine wave has information that concerns dip and azimuth, and is represented with a tadpole. Rose diagrams were used to display fracture strike and dip for the three wells.

Open fractures are solely developed in sandstone intervals. This was used as the main criterion to distinguish them from the drilling induced fractures. They can have

various orientations with respect to borehole breakouts. Generally, they show dips lower than drilling induced fractures (near vertical).

Resistive fractures cannot be confused with any other type of fractures because of their mineral filling.

5.2. Results

Natural fractures in this study are represented with strike rose diagrams of two major groups: open and resistive fractures.

5.2.1. Open Fractures

Open fractures tend to have a consistent orientation in the imaged interval of the four wells. Figures 5.1 to 5.4 show the strike and dip rose diagrams for the wells. All four wells show mean strike of 100^{o} with minor variations of 15 degrees. Besides the main trend, open fractures for the RMV 60-17 well show secondary orientations in various directions. Average dip of the open fractures is lower than the dip of drilling induced fractures by about 15^{o}.

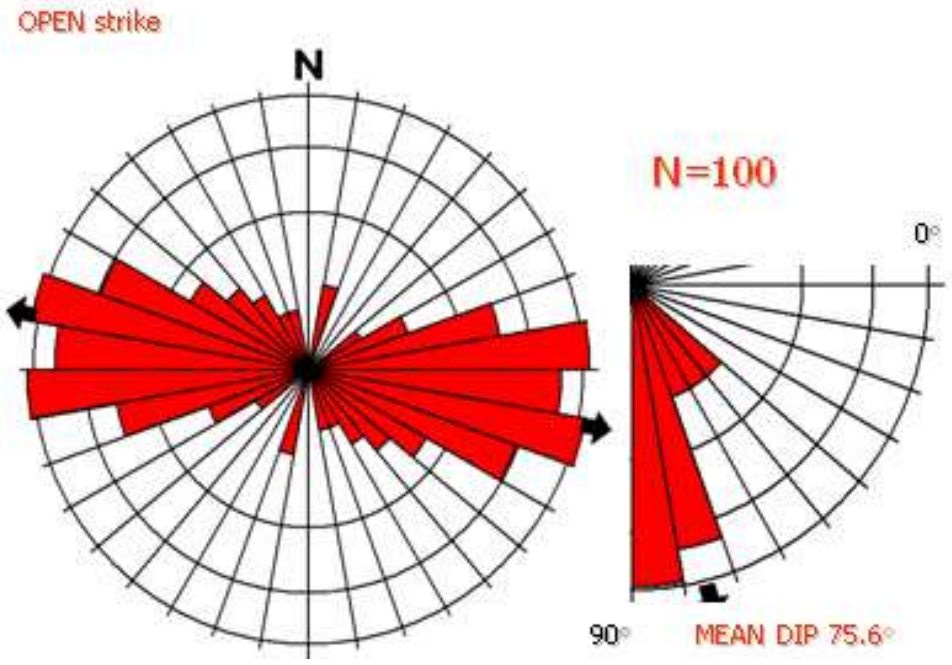

Figure 5.1. Rose diagrams of open fractures in the RWF 542-20 well (strike=left, dip=right). There is a dominant set of fractures with strike azimuth of 100°. Mean dip shows a value of 75.6°.

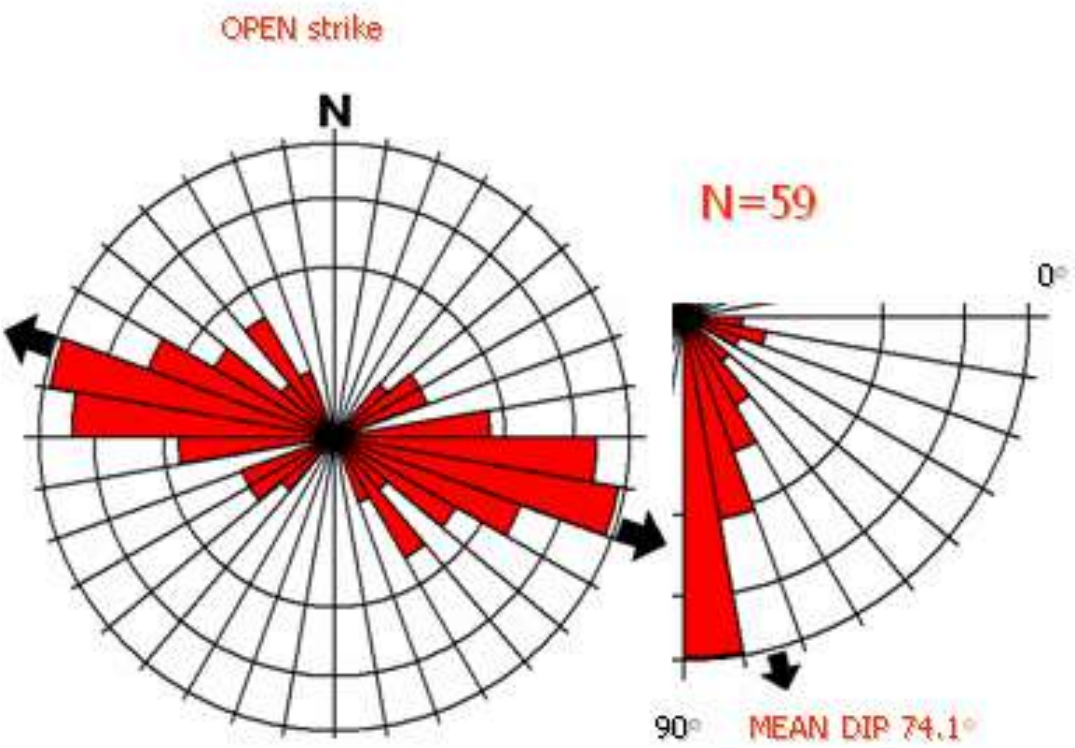

Figure 5.2. Rose diagrams of open fractures in the RWF 523-20 well (strike=left, dip=right). There is a dominant set of fractures with strike azimuth of 107°. Mean dip shows a value of 74.1°.

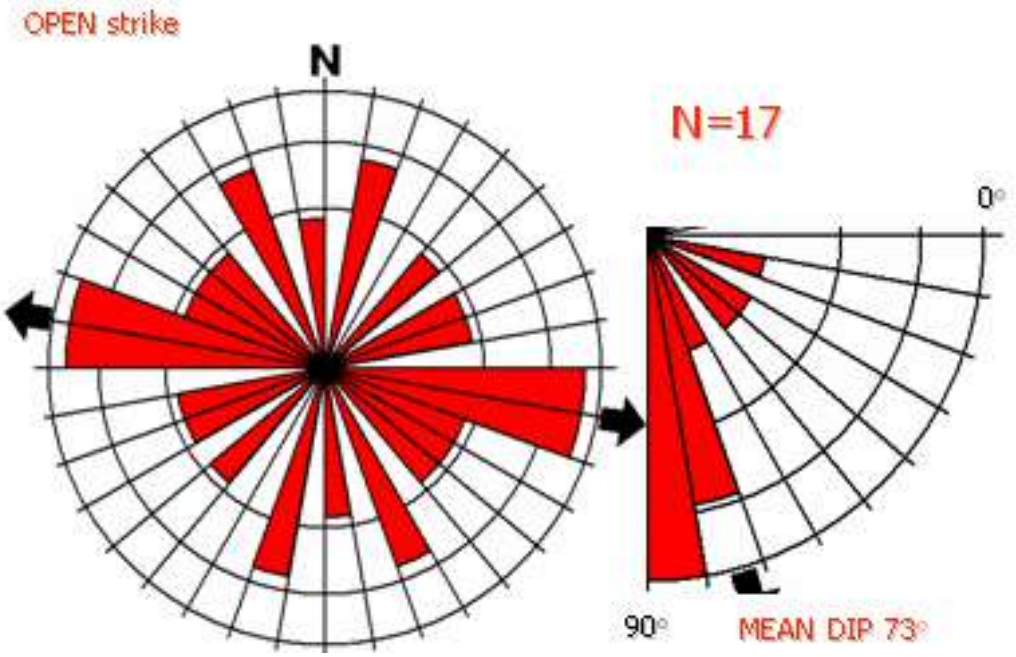

Figure 5.3. Rose diagrams of open fractures in the RMV 60-17 well (strike=left, dip=right). There is a dominant set of fractures with strike azimuth of 100°. The minor set shows inconsistent orientation. Mean dip shows a value of 73°.

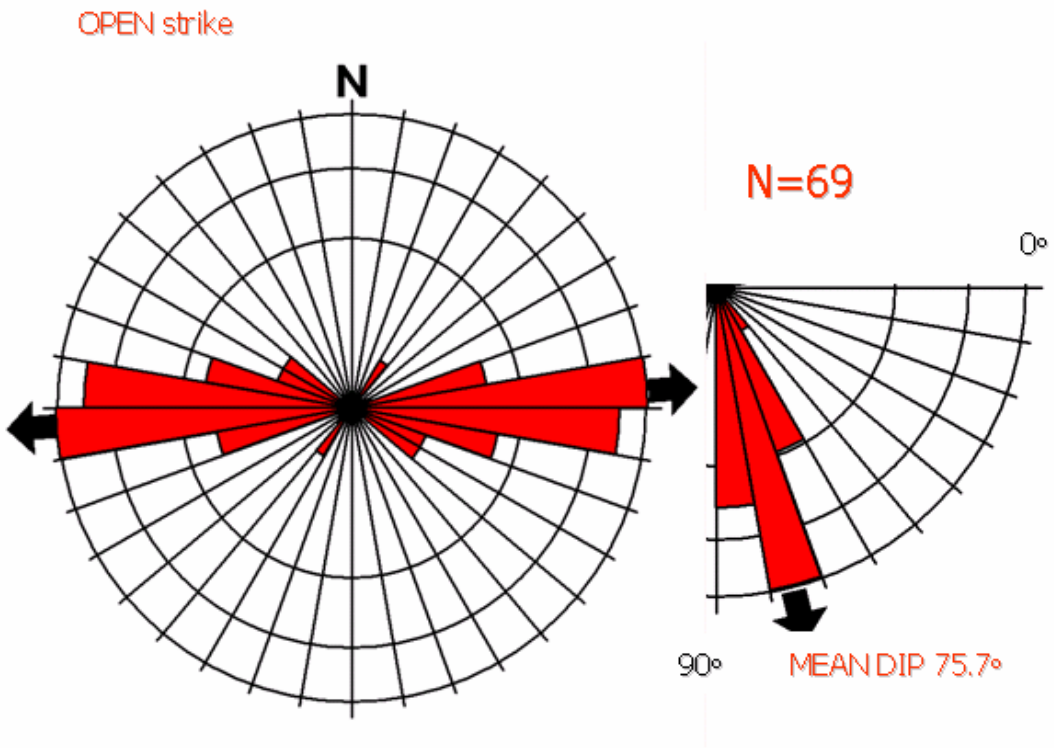

Figure 5.4. Rose diagrams of open fractures in the RWF 441-20 well (strike=left, dip=right). There is a dominant set of fractures with strike azimuth of 88°. Mean dip shows a value of 75.7°.

5.2.2. Resistive Fractures

Figures 5.5 to 5.8 show the strike and dip azimuth rose diagrams for the RWF 542-20, RMV 60-17 and RWF 441-20 wells. In well RWF 523-20, only one resistive fracture was interpreted. In the rose diagram for the three wells combined, three sets of resistive fractures are apparent (Figure 5.7). The mean strike of the dominant set is 330°. The two minor sets show strikes of 70 and 110^{o} degrees, respectively. The mean dip angle for all three wells is 35^{o}. The rose diagrams from RWF 441-20 were appended to support the results from the previously interpreted three wells. The strike of the dominant set is 88^{o}. The minor set shows a strike of 125 degrees.

5.3. Discussion

In some cases it was difficult to distinguish between natural open and drilling induced fractures (Chapter 4). Because the stress orientation remained relatively constant in the geologic history of the Piceance basin, some open fractures might have been overprinted with induced fractures. Furthermore, induced and open natural fractures have the same mean orientation.

Two sets of resistive fractures parallel the orientation of fractures determined by Kuuskraa et al. (1997). They noticed a series of N30W and N60E fractures associated

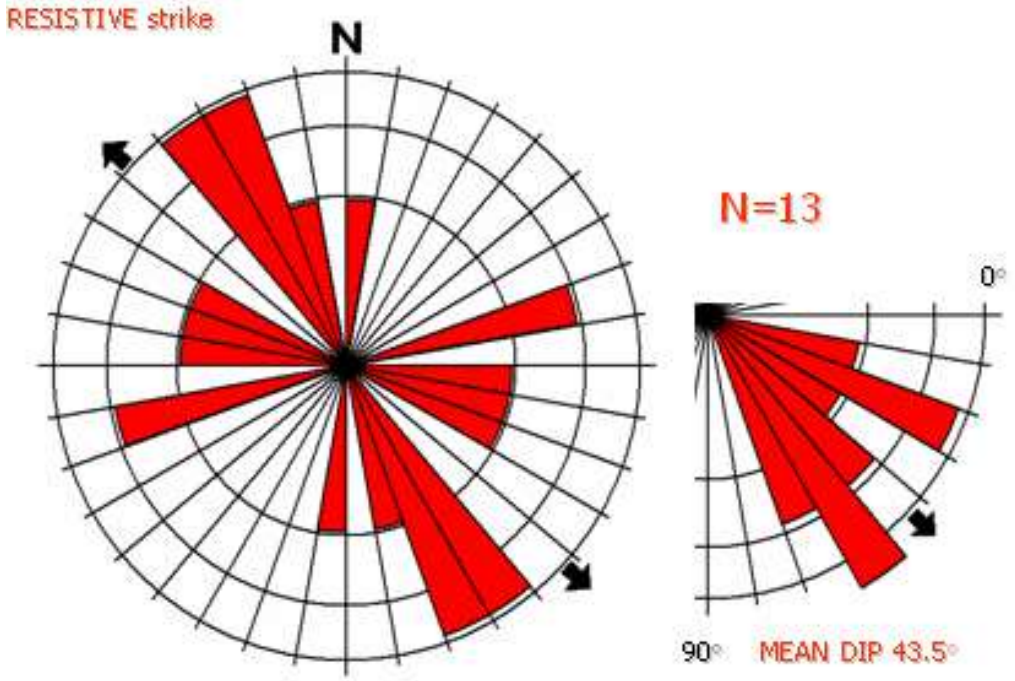

Figure 5.5. Rose diagrams of resistive fractures in the RWF 542-20 well (strike=left, dip=right). There is a dominant set of fractures with strike azimuth of 330°. The two minor sets show strikes of 75° and 105° degrees, respectively. Mean dip shows a value of 43.5°.

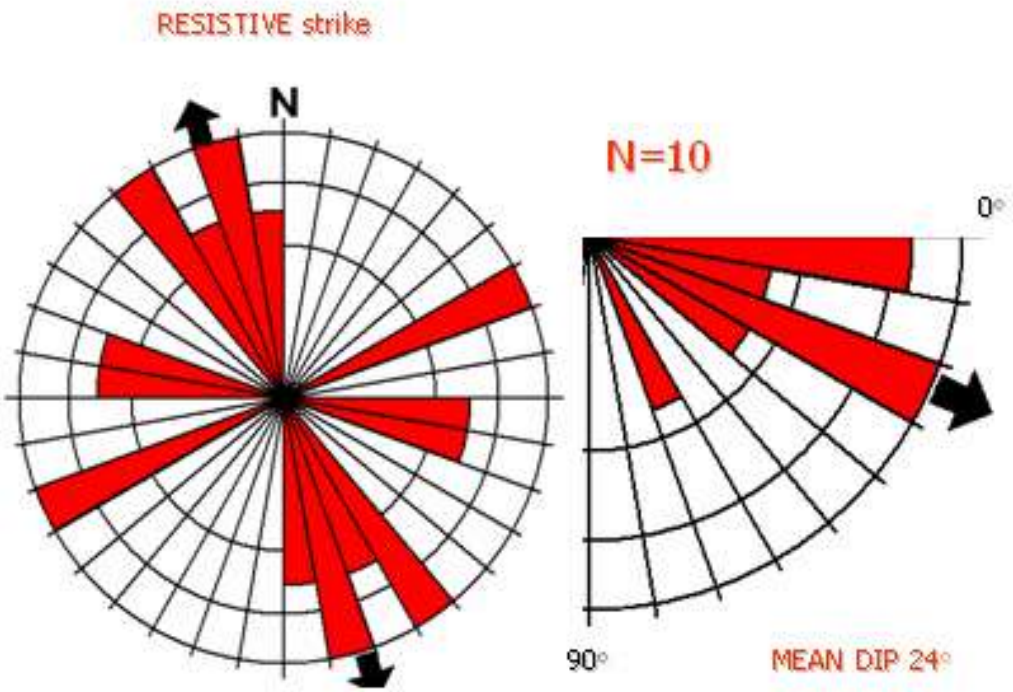

Figure 5.6. Rose diagram of resistive fractures in the RMV 60-17 well (strike=left, dip=left). There is a dominant set of fractures with strike azimuth of 340°. The two minor sets show strikes of 65° and 100° degrees, respectively. Mean dip shows a value of 24°.

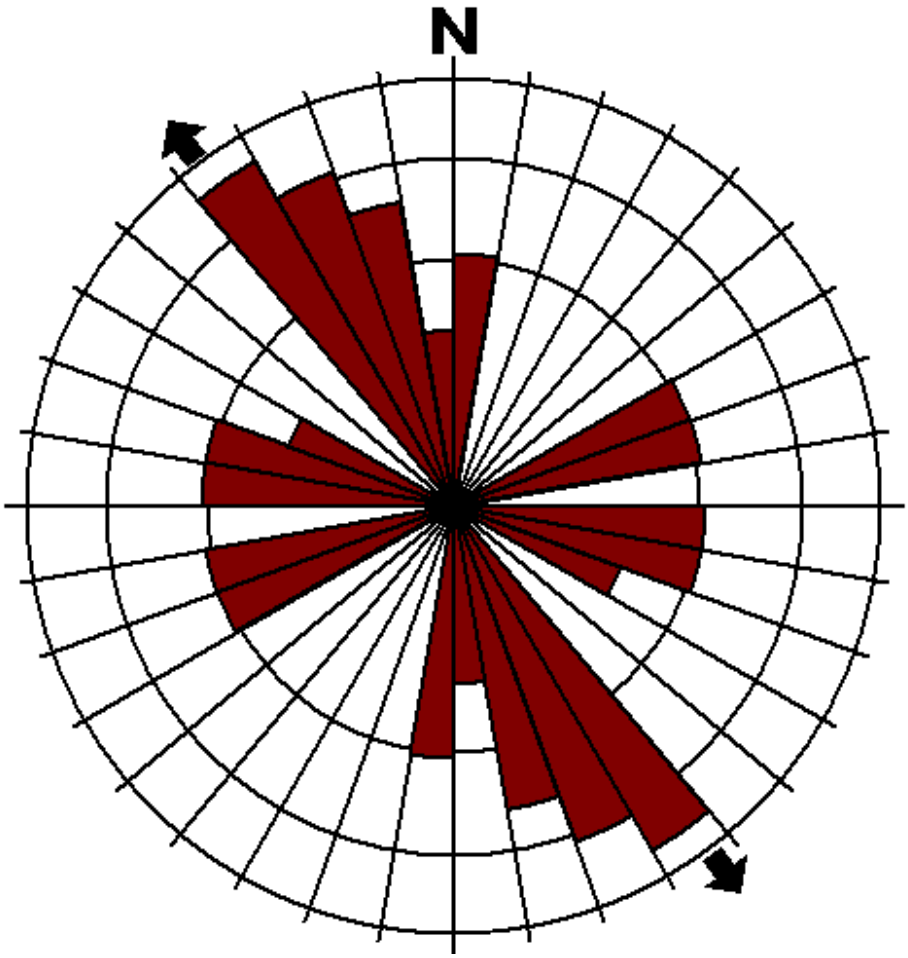

Figure 5.7. Strike rose diagram of resistive fractures for the RWF 542-20 RMV, RWF 523-20 and RMV 60-17 wells combined. There is a dominant set of fractures with strike azimuth of 340^{o}. The two minor sets show strikes of 70^{o} and 110^{o} degrees, respectively. Mean dip value is 35^{o}.

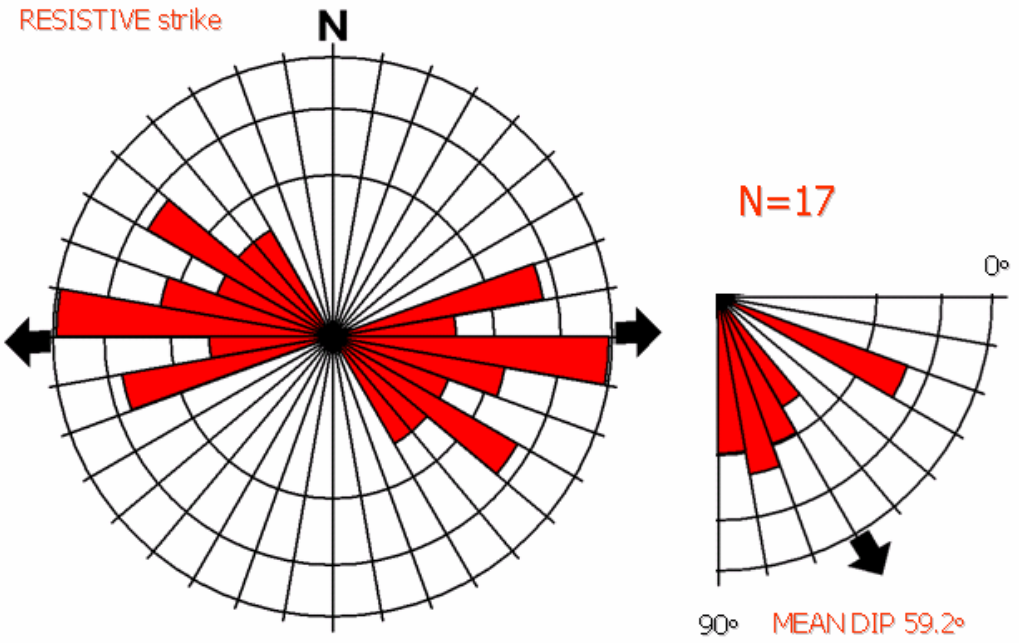

Figure 5.8. Rose diagram of resistive fractures in the RWF 441-20 well (strike=left, dip=left). There is a dominant set of fractures with strike azimuth of 95°. Mean dip shows a value of 59.2°.

with larger-scale faults, joints, and fractures in Rulison field. The existence of the two sets might suggest that larger-scale structural features exist in the vicinity of the RWF 542-20 and RMV 60-17 wells. The third, least numerous set of resistive fractures shows the orientation of SHmax, suggesting that it was created in the same stress regime as the drilling induced or natural open fractures. The well RWF 441-20 has the dominant set which parallels the orientation of SHmax. The minor sets are absent, which might suggest that the well was drilled away from the larger-scale structural features.

Resistive fractures have lower dip angles than open natural fractures by about 40^{o}.

CHAPTER 6

BASE OF GAS SEEPS

Because of the lack of production logs in the RCP area, gas seeps were interpreted to help determine qualitatively the more productive intervals. Also, there was a question about correlation of those features with any structural or lithologic controls in the imaged wells.

Gas in the image log is a feature which is possible to interpret (Figure 6.1). Also, gas obscures structural and stratigraphic features. A usual phenomenon associated with gas is that a bubble of gas is stuck under the tool pad and dragged along the borehole wall. The bubble under the pad can obscure the shallower gas-seep base and lead to a false interpretation about quantities of gas. Another important factor is the mud weight. Overbalanced drilling and formation damage can cause gas not to flow into the well during drilling and/or logging.

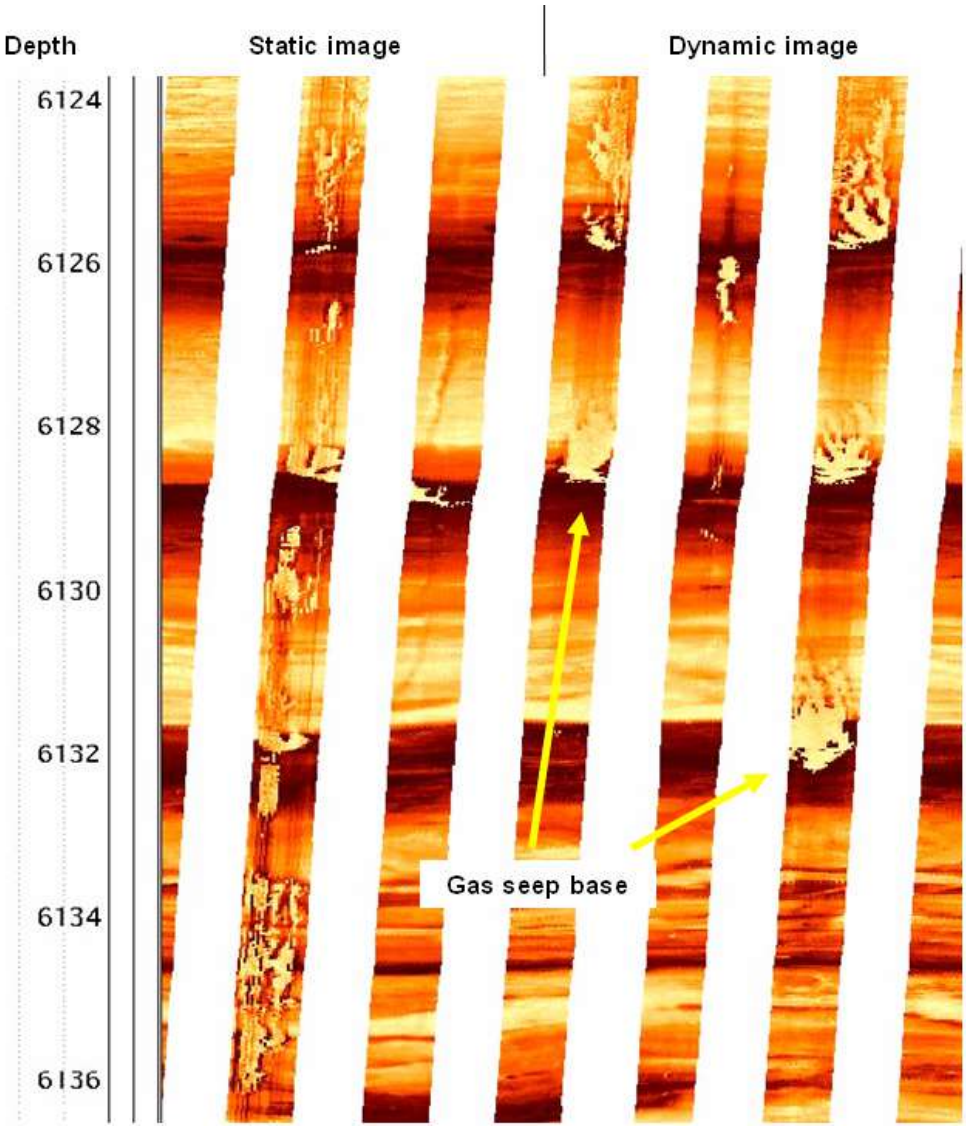

Figure 6.1. Gas seeps in the image log in well RWF 542-20. Depth scale is in ft.

6.1. Methods

Bases of the gas seeps were interpreted in the image logs by fitting a straight line through the lowest point of each feature. The point of the gas seep also has information concerning depth and gamma ray value (GR). The GR value was used to show the distribution of values in order to answer questions about the dominant lithology of the gas seeps. The plot of mud weight vs. gas-seep density shows the importance of mud weight.

6.2. Results

The GR value was sampled at the base of each gas seep. The histograms of the GR along the imaged interval and the GR values of gas seeps for the RWF 542-20 well show a similar bimodal distribution (Figure 6.2). The well RMV 60-17 shows even more similarity between the mentioned distributions (Figure 6.3). The similarity of descriptive statistical parameters confirms the same observation. Well RWF 523-20 has no gas seeps.

Figures 6.4 and 6.5 show the bases of gas seeps for wells RWF 542-20 and RMV 60-17. The figures show a combination of the fracture, GR of imaged interval, gas seep, gas-seep density (number of gas seeps per 10 ft) and mud-weight logs plotted

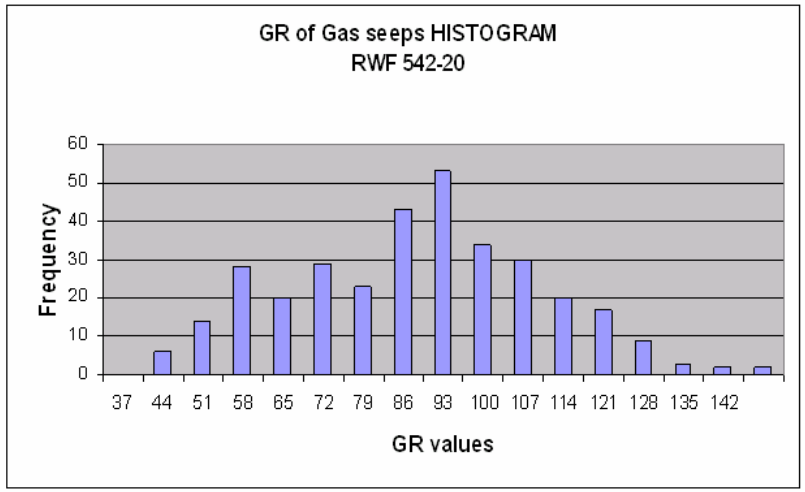

Mean	78.12384
Standard Error	1.205888
Median	79.4602
Mode	77.7116
Standard Deviation	22.0054
Sample Variance	484.2374
Kurtosis	-0.47829
Skewness	0.020997
Range	109.3815
Minimum	30.9391
Maximum	140.3206
Sum	26015.24
Count	333

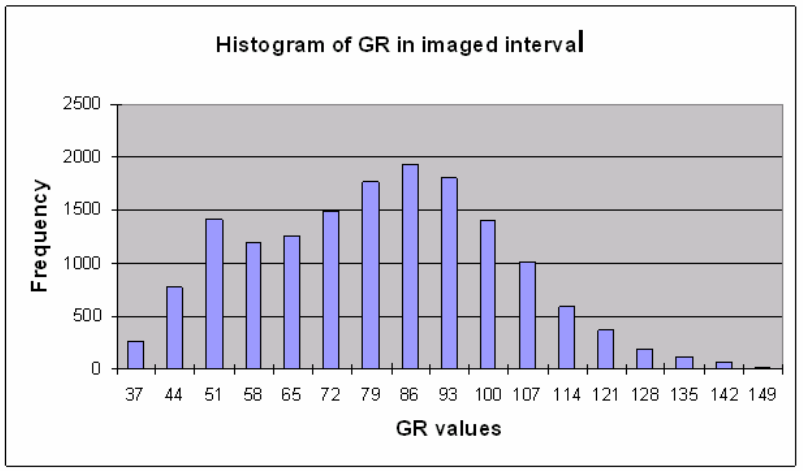

Mean	76.71441
Standard Error	0.178574
Median	77.55735
Mode	82.1808
Standard Deviation	22.41652
Sample Variance	502.5003
Kurtosis	-0.42667
Skewness	0.117994
Range	146.6017
Minimum	18.5831
Maximum	165.1848
Sum	1208866
Count	15758

Figure 6.2. Comparison of GR of gas seeps and overall GR values of imaged interval for RWF 542-20 well.

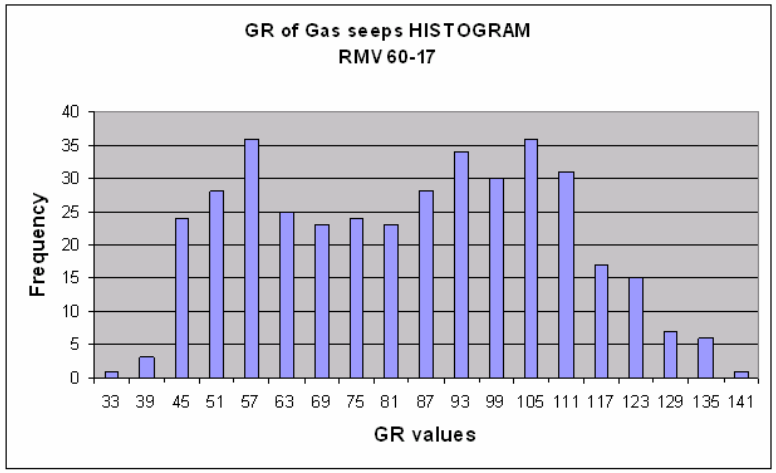

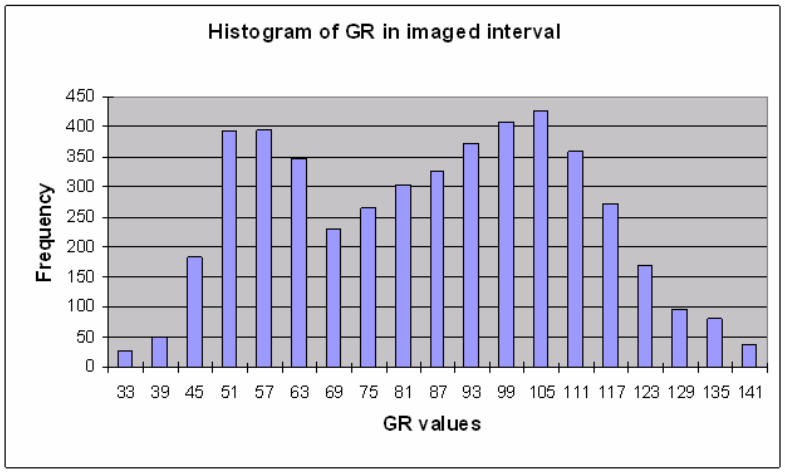

Mean	82.61599
Standard Error	1.294356
Median	84.35
Mode	90.7
Standard Deviation	25.69224
Sample Variance	660.0913
Kurtosis	-0.97352
Skewness	0.069773
Range	116.1
Minimum	33.1
Maximum	149.2
Sum	32550.7
Count	394

Mean	82.85103535
Standard Error	0.373892172
Median	84.6
Mode	53.4
Standard Deviation	25.85269038
Sample Variance	668.3615999
Kurtosis	-0.708765312
Skewness	0.100631209
Range	196.5
Minimum	14
Maximum	210.5
Sum	396110.8
Count	4781

Figure 6.3. Comparison of GR of gas seeps and overall GR values of imaged interval for RMV 60-17 well.

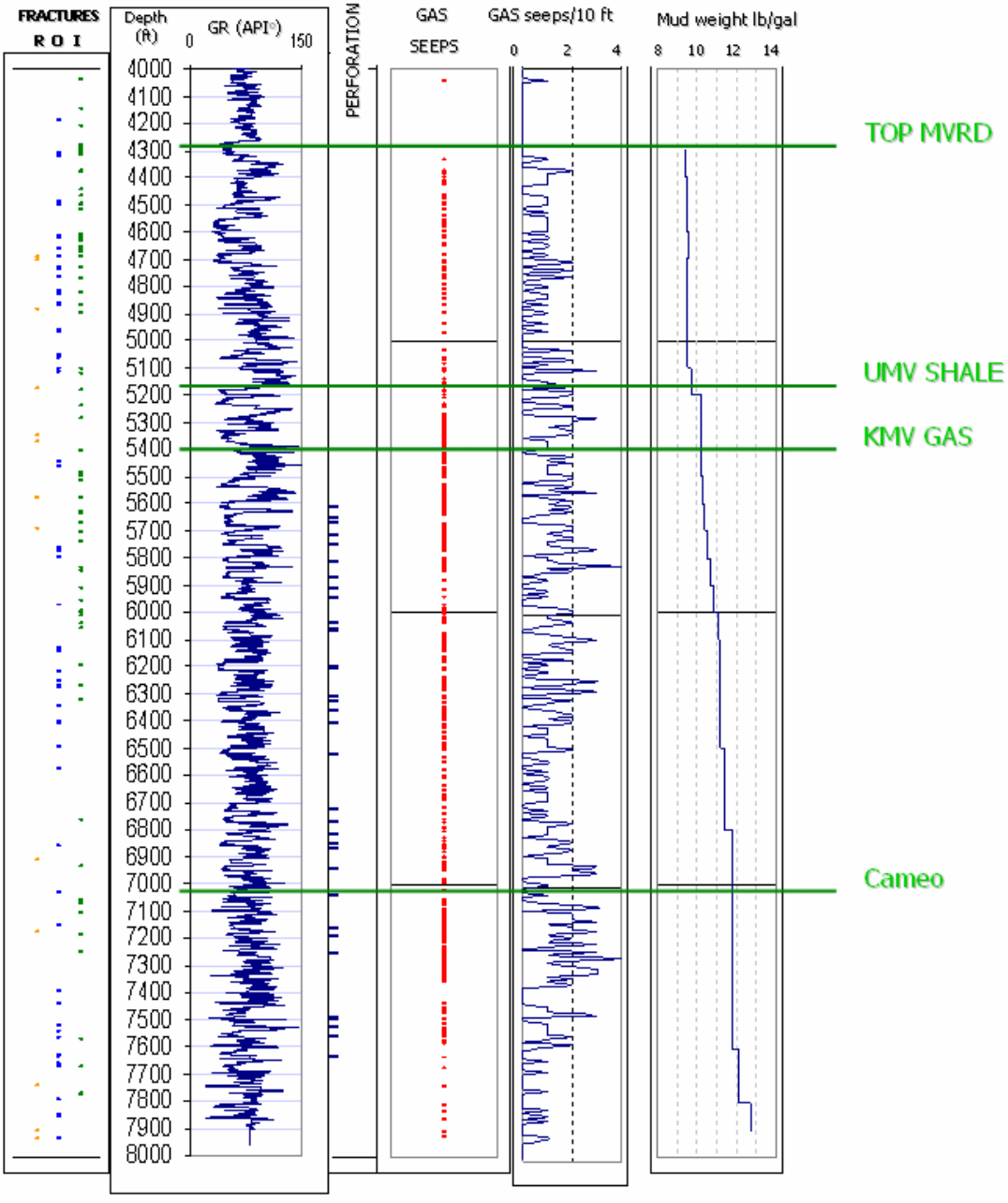

Figure 6.4. Combination of the fracture, GR of imaged interval, gas seep, gas-seep density (number of gas seeps per 10 ft) and mud-weight logs in the RWF 542-20 well. Abbreviations: R=resistive fractures; O= open fractures; I= drilling induced fractures.

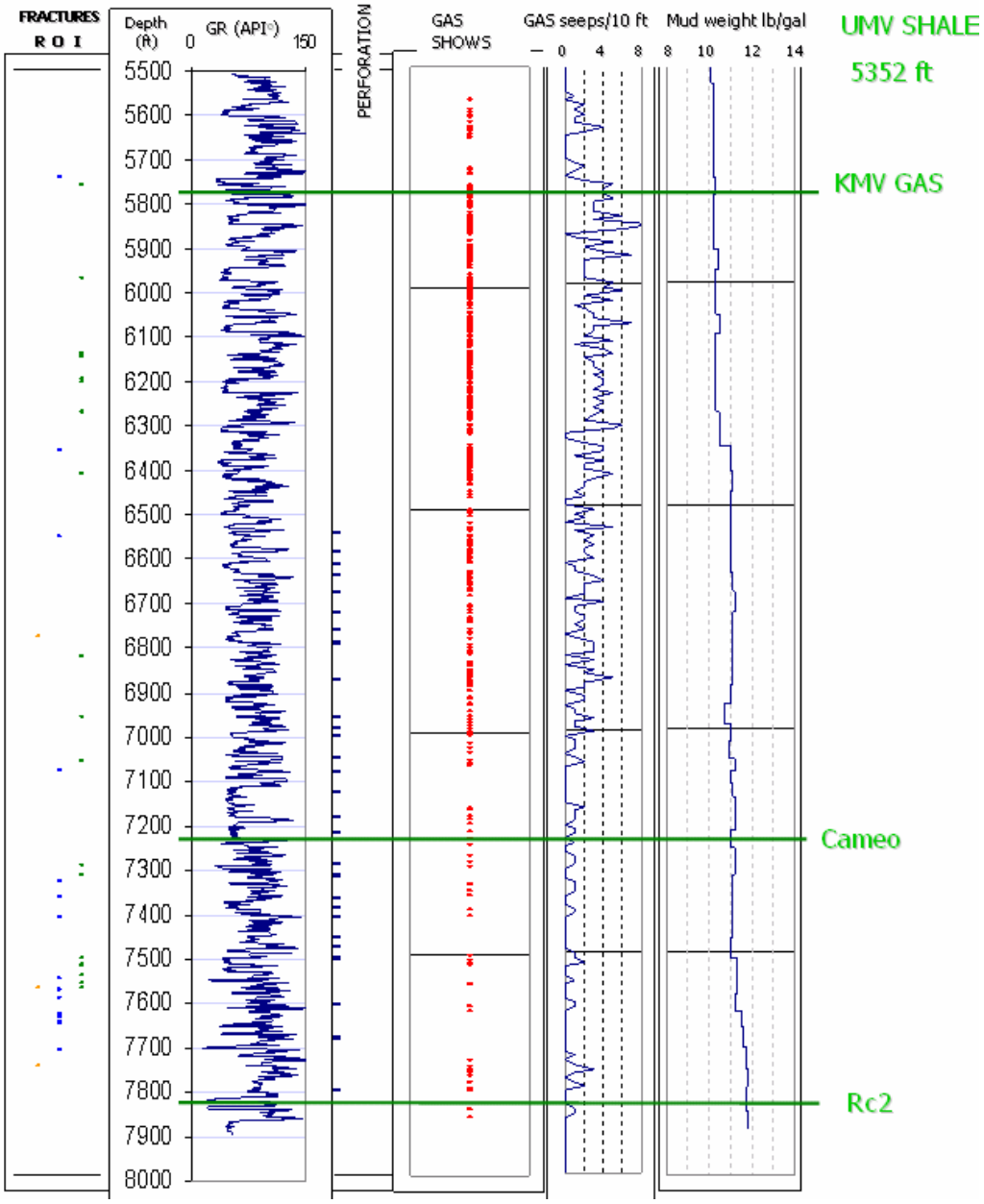

Figure 6.5. Combination of the fracture, GR of imaged interval, gas seep, gas-seep density (number of gas seeps per 10 ft) and mud-weight logs in the RMV 60-17 well. Abbreviations: R=resistive fractures; O= open fractures; I= drilling induced fractures.

against the gamma ray curve and their correlation with fractures and mud weight.

In the RWF 542-20 well gas seeps occur at most mud weights (Figure 6.6). The number of gas seeps decreases for the RMV 60-17 well with high values of mud weight (Figure 6.7).

6.3. Discussion

Most of the imaged interval shows the presence of gas seeps. Gamma ray (GR) values of gas seeps in the imaged interval of wells RMV 60-17 and RWF 542-20 show a bimodal distribution which mimics the GR distribution of the imaged intervals. That suggests that there is no dominant lithology of gas seeps.

Furthermore, I noticed that gas seeps are continuously developed throughout the Mesaverde section. That suggests that 2 wells were drilled under balanced. There was no definitive relationship between fractures, sandstone beds and gas seeps.

The absence of gas shows in the RWF 523-20 image log might be related to the weighted-up mud column (personal communication with Lesley Evans, Williams geologist), since the logging on the well was extensive.

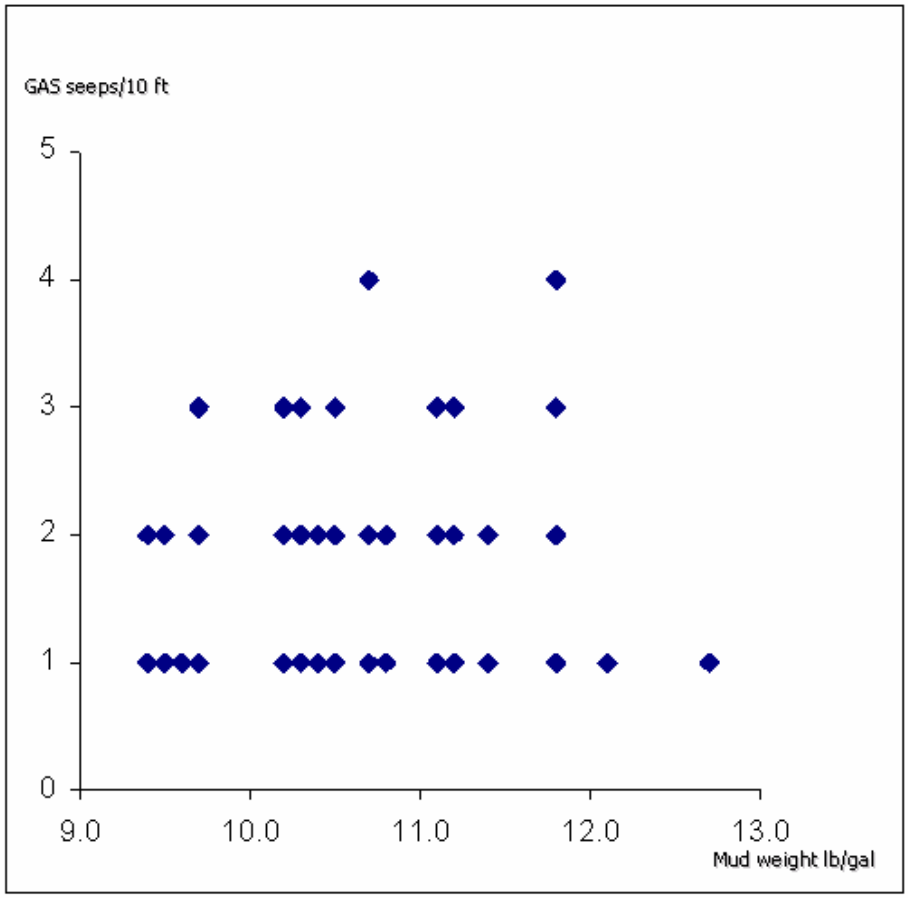

Figue 6.6. Gas-seep density versus mud weight for the RWF 542-20 well. Gas seeps occur at most mud weights.

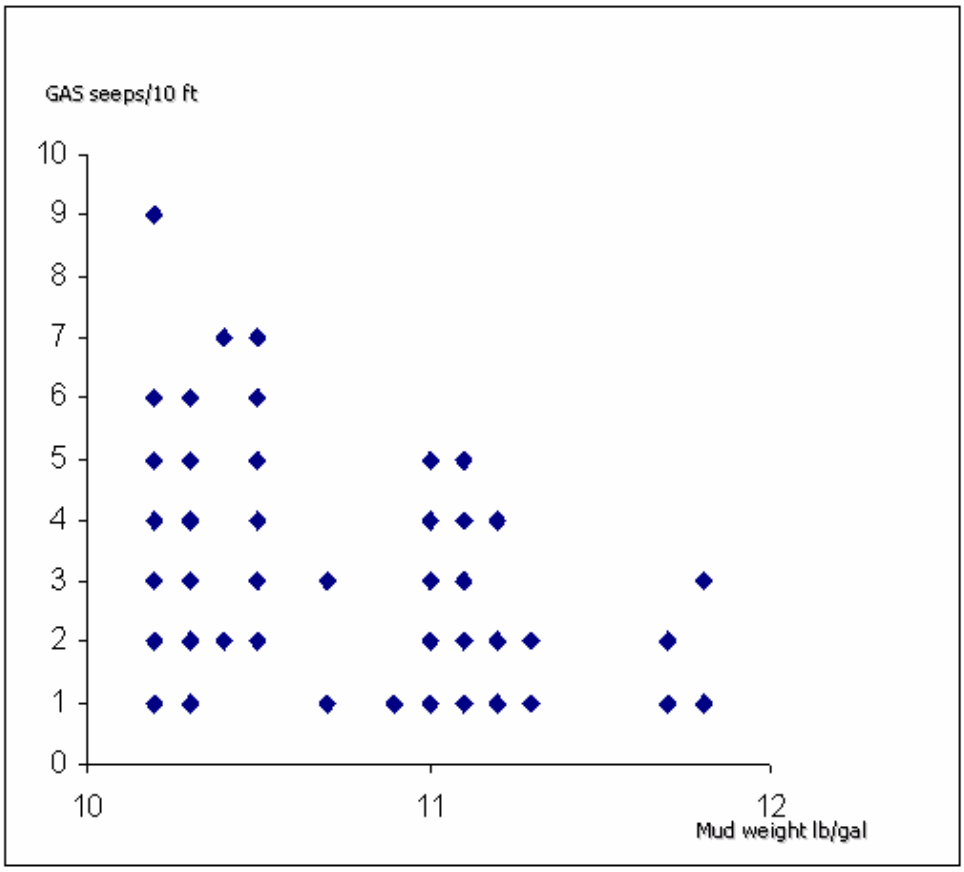

Figure 6.7. Gas-seep density versus mud weight for the RMV 60-17 well. High values of mud weight correspond to decreased gas-seep density.

If we assume that both observed wells have the same production potential and distribution of gas along the well, one has to take into consideration the importance of the mud column. There is a probable relationship between relatively small changes in the mud-weight column versus gas-seep density. Two observed wells, with similar depths and mud-weight values, have significantly different gas-seep profiles. Small changes in the mud-weight column can significantly alter the number of gas seeps.

Because of the mentioned factors, gas-seep base interpretations have to be approached with caution, and used as qualitative indicators of gas presence.

CHAPTER 7

MICROFAULT AND FAULT ANALYSIS

Structural components and determination of more productive intervals are two essential features which need to be better understood in Rulison field. The purpose of this study is to use the image logs from wells RWF 542-20, RWF 523-20 and RMV 60-17 to help solve these complex issues. Image-log interpretations and dip-domain analyses were performed for the purpose of identifying faults and microfaults, generally smaller than those interpreted from seismic data. The results from the Halliburton report for well RWF 441-20 are included in the Discussion section.

7.1. Methods

Two types of dip-domain analyses were performed: cumulative dip plots and dip azimuth vector plots. Cumulative dip plots are more useful than conventional cross-plots or tadpole diagrams because they highlight subtle changes and tend to smooth out erratic patterns in measured dips (Hurley, 1994). A dip domain is characterized by either relatively constant dip magnitude or dip azimuth. Cumulative dip plots were constructed

to identify dip domains of constant dip magnitude, and dip azimuth vector plots were constructed to identify dip domains of constant dip azimuth. Both of the dip-domain analyses use shale beds as input. This was accomplished by assigning each dip a gamma ray value. 80 API units was the cutoff in the wells interpreted in this study. Anything above this gamma ray cut off was used in the following plots. The beds with GR values higher than the cutoff were regarded as shales. The assumption is that the shales were deposited horizontally and that the present-day structural dip is caused by tectonic activity. Every inflection point from cumulative dip and dip azimuth vector plots was checked in the image log to find possible evidence of faulting.

All interpreted microfaults were shown in strike azimuth rose diagrams.

7.2. Results

Results of the two types of dip-domain analyses (cumulative dip plots and dip azimuth vector plots) are shown in the first section. In the following section, representation of the faults in the image logs is documented.

7.2.1. Cumulative Dip Plots

This process (Hurley, 1994) involves cross-plotting cumulative dip magnitude versus sample number. Sample numbers were used rather than depth measurements because of the irregular distances between the identified bedding planes. Using the assumption that shale beds were originally deposited horizontally, a straight segment on a shale bed cumulative-dip plot was interpreted to represent structural dip of a given dip domain (Knight, 1999). Abrupt changes in dip magnitude were interpreted as possible faults or unconformities. Figures 7.1 to 7.3 show cumulative dip plots for the shale-bed data sets corresponding to wells RWF 542-20, RWF 523-20 and RMV 60-17. Inflection points and corresponding depths are shown. Every inflection point from the cumulative dip plots was checked in the corresponding image log to find possible evidence of faulting. In the RWF 542-20 well (Figure 7.1), 41 dip domains are separated by 40 inflection points. Abrupt changes in dip direction are interpreted as possible faults. Two inflection points were confirmed in the image logs to be probable faults. The RWF 523-20 well, has 29 dip domains separated by 28 inflection points (Figure 7.2). Evidence of faulting was found in 9 inflection points. There are 31 dip domains in the RMV 60-17 well, separated by 30 inflection points (Figure 7.3). Six of the inflection points showed the evidence of faulting in the image log. All inflection points are shown in Appendix C.

In total, 17 inflection points were confirmed as faults with structural features observed in images.

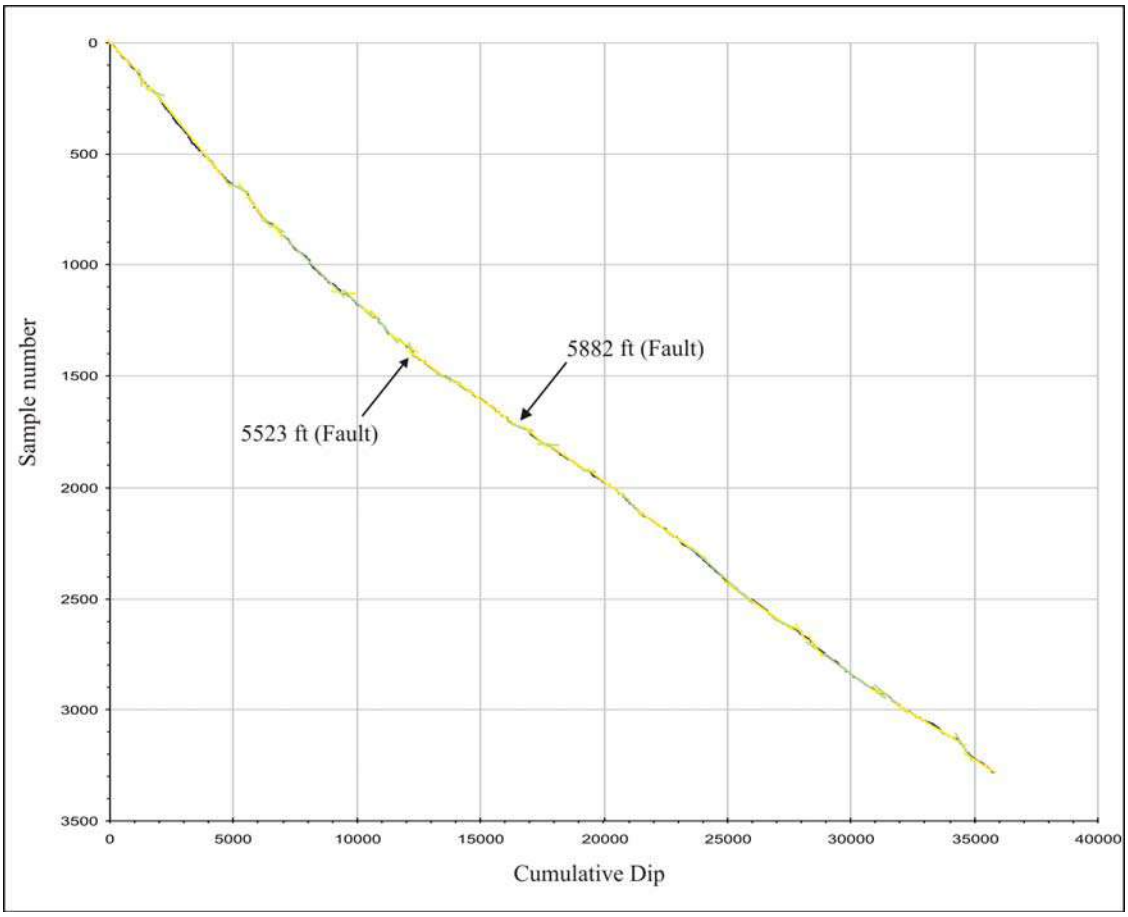

Figure 7.1. Cumulative dip plot in the well RWF 542-20. Notice 2 depth points (inflection points), confirmed in image logs to be probable faults.

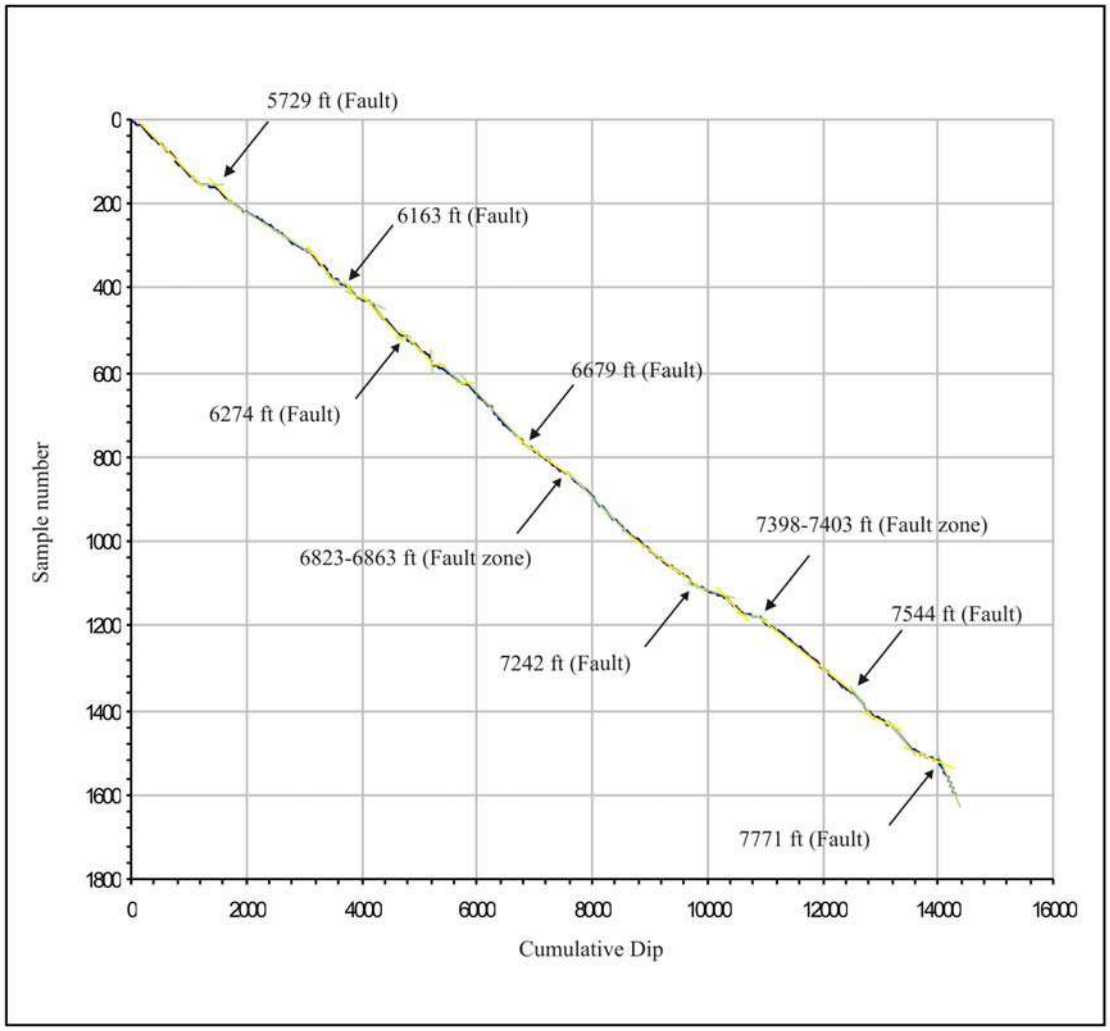

Figure 7.2. Cumulative dip plot in the well RWF 523-20. Notice 9 depth points (inflection points), confirmed in image logs to be probable faults or fault zones.

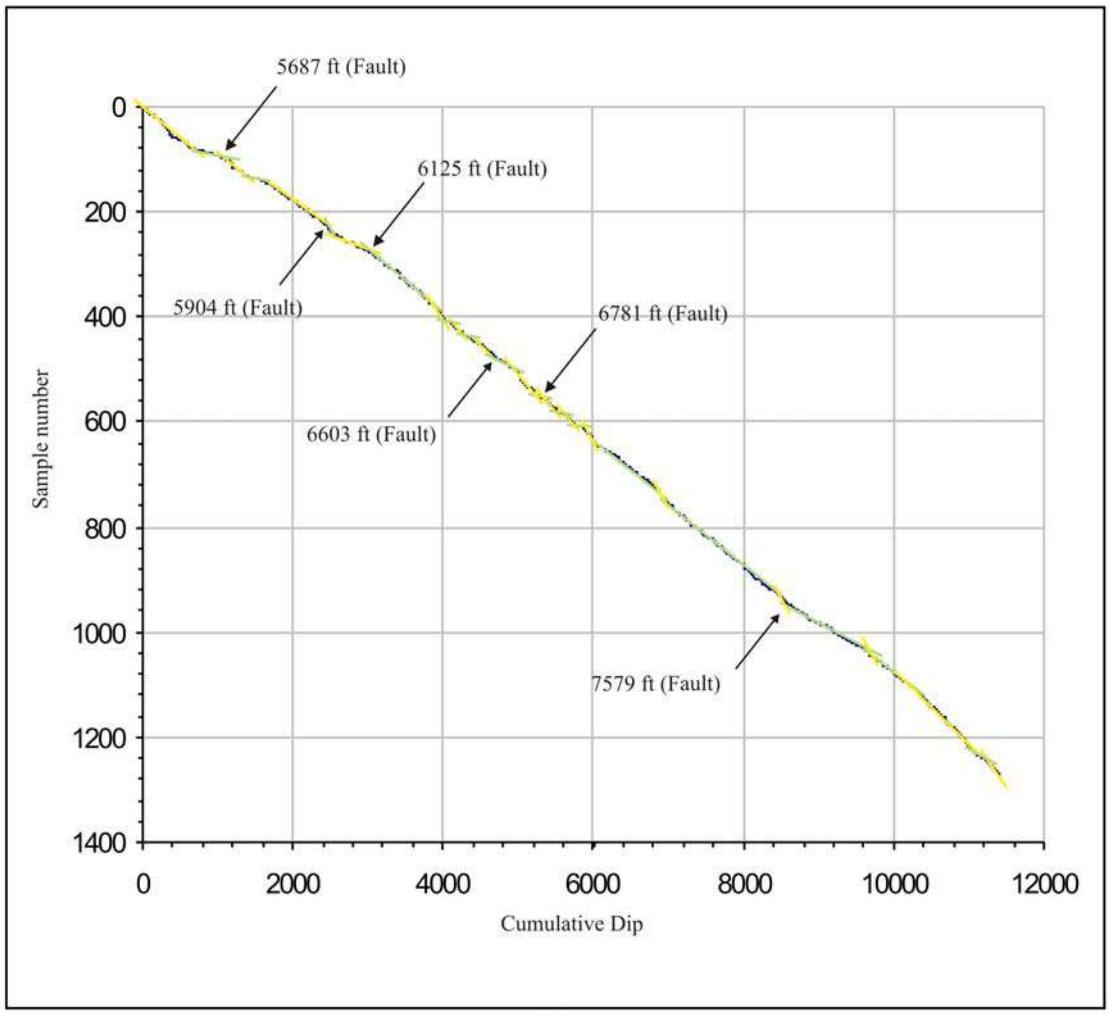

Figure 7.3. Cumulative dip plot in the well RMV 60-17. Notice 6 depth points (inflection points), confirmed in image logs to be probable faults.

7.2.2. Dip Azimuth Vector Plots

Dip azimuth vector plots were generated by plotting, in map-view format, the vectors corresponding to shale bedding-plane dip azimuths. Beginning with the deepest measured bed orientation, a unit vector pointing in the direction of each bedding plane dip was plotted. The second vector, plotted at the tip of the first vector, represents the next bed up the hole. In a like manner, subsequent vectors were plotted to represent sequential up-hole dip azimuths. Each vector has the same length. Again, inflection points on a vector plot represent abrupt changes in dip direction, which can be related to faults.

Every inflection point from dip azimuth vector plots was checked in image logs to find possible evidence of faulting. Three graphs of dip azimuth vector plots of shale beds were plotted (Figures 7.4 to 7.6). In the RWF 542-20 well, 11 dip azimuth domains are separated by 10 inflection points (Figure 7.4). Three inflection points were confirmed in the image logs to be probable faults. There are 27 dip azimuth domains in the RWF 523-20 well, separated by 26 inflection points (Figure 7.5). Six inflection points were confirmed with structural features in images. Interpretation of the RMV 60-17 showed the existence of 17 dip domains, separated by 16 inflection points (Figure 7.6). One inflection point was confirmed to be a probable fault.

In total, 10 probable faults were interpreted in the three dip azimuth vector plots.

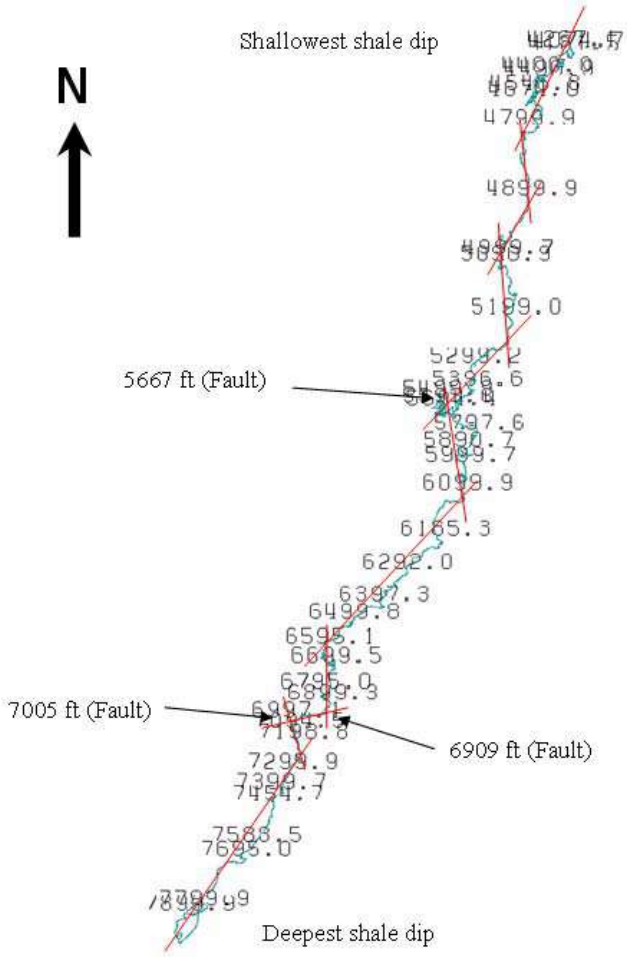

Figure 7.4. Dip azimuth vector plot in the RWF 542-20 well. Notice three depth points, confirmed in image logs to have structural features associated with faulting.

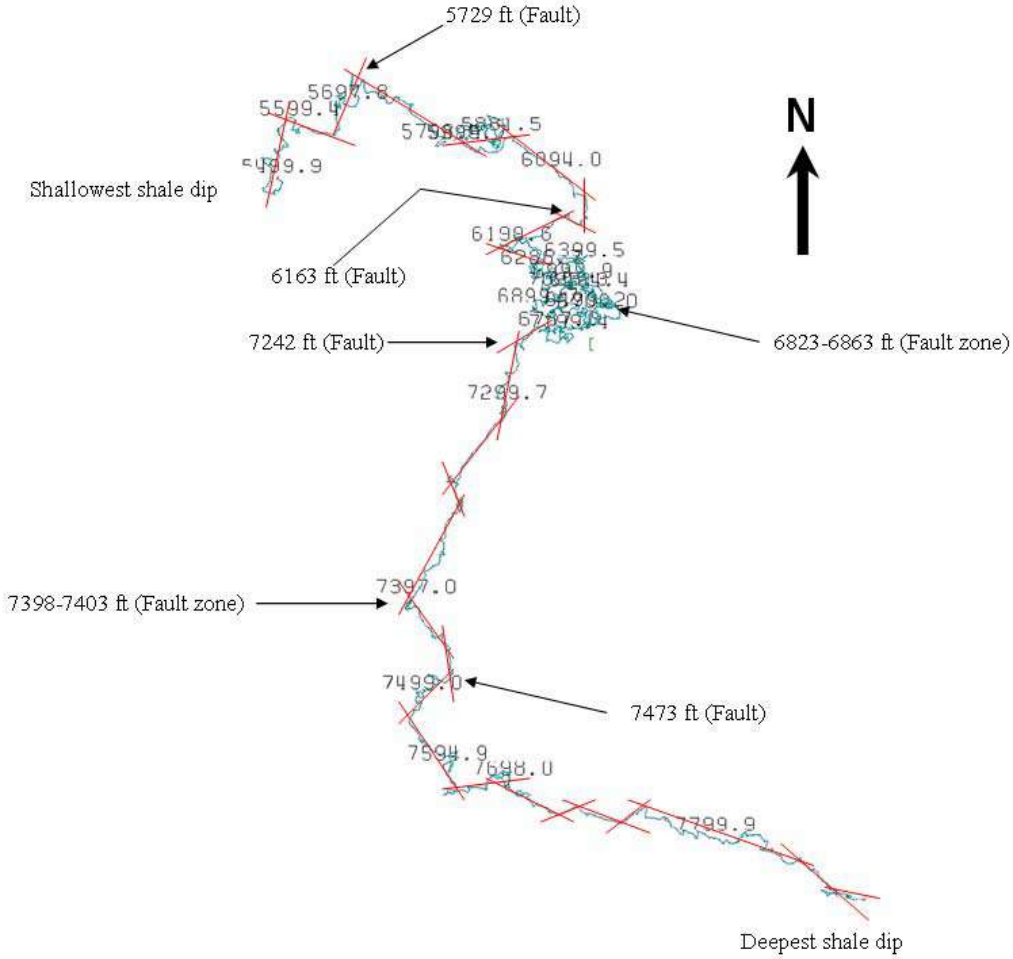

Figure 7.5. Dip azimuth vector plot in the RWF 523-20 well. Notice six inflection points, confirmed in the image log to have structural features associated with faulting.

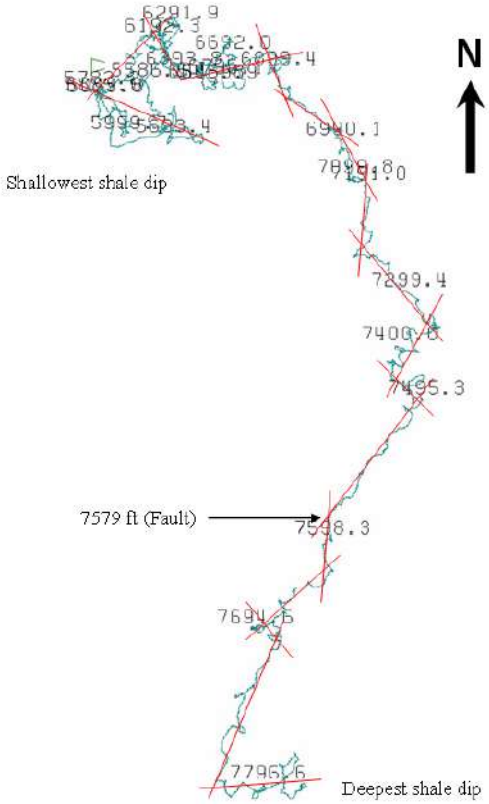

Figure 7.6. Dip azimuth vector plot in the RMV 60-17 well. Notice one depth point, confirmed in the image log to have structural features associated with faulting.

7.2.3. Faults in the Image Logs

Six structural features showed evidence of faulting in both cumulative dip plots and dip azimuth vector plots of shale beds. The other 14 features showed evidence of faulting in only one of the dip domain plots (Table 7.1). Their representation in the image logs is shown in Figures 7.7 to 7.27.

The overall strike azimuth rose diagram of the 18 interpreted fault surfaces with their respective dip and azimuth is shown in Figure 7.28. In spite of the low number of interpreted faults, two azimuth directions show a relatively high frequency (55^o and 345^o). Their average dip is 50^o. Figures 7.30 to 7.32 show a combination of the GR of the imaged interval with gas-seep, fracture and mud-weight logs.

7.3. Discussion

In well RWF 523-20, the occurrence of the open fractures can be noticed at the depths of fault surfaces. There is no definitive relationship between the location of microfaults, fractures or gas seeps.

The faults were pinpointed with an accuracy of 20 ft above and below the particular inflection point. This accuracy, combined with careful examination of image logs, does not leave much probability for the eventually omitted faults.

RWF 542-20			RWF 523-20			RMV 60-17		
CDP	Depth (ft)	DAVP	CDP	Depth (ft)	DAVP	CDP	Depth (ft)	DAVP
●	5523		●	5729	●	●	5687	
	5667	●	●	6163	●	●	5904	
●	5882		●	6274		●	6125	
	6909	●	●	6679		●	6603	
	7005	●	●	6823-6863	●	●	6781	
			●	7242	●	●	7579	●
			●	7398-7403	●			
				7473	●			
			●	7544				
			●	7771				

Table 7.1. Inflection points in dip-domain plots. Symbol "●" means evidence of faulting both in image and plot. Abbreviations: CDP=Cumulative dip plot, DAVP=Dip azimuth vector plot.

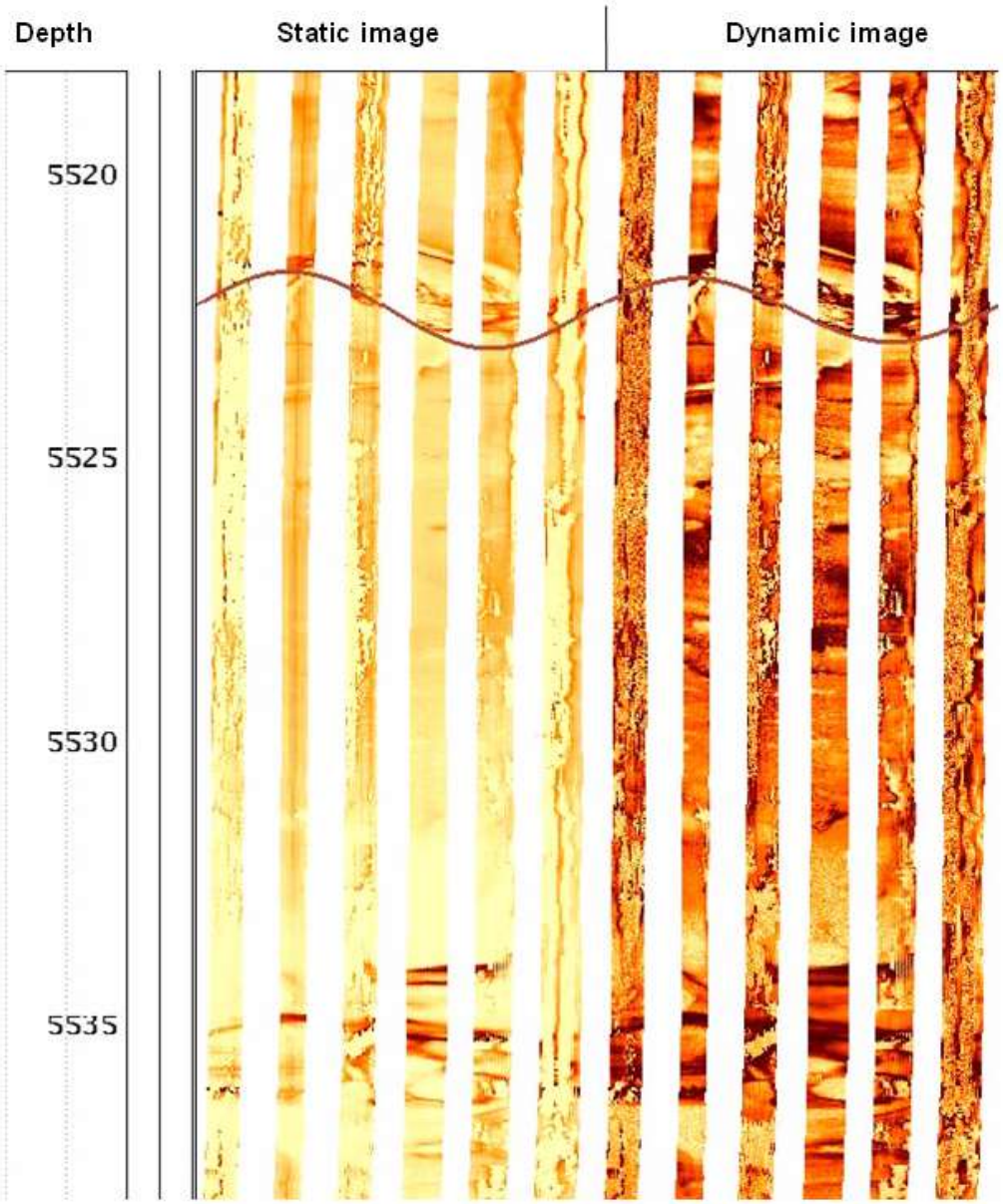

Figure 7.7. Inflection point at 5523 ft confirmed with fault in the RWF 542-20 image log. Breccia is present above the sine wave. Depth scale in feet. Dip 60°; dip azimuth 263°.

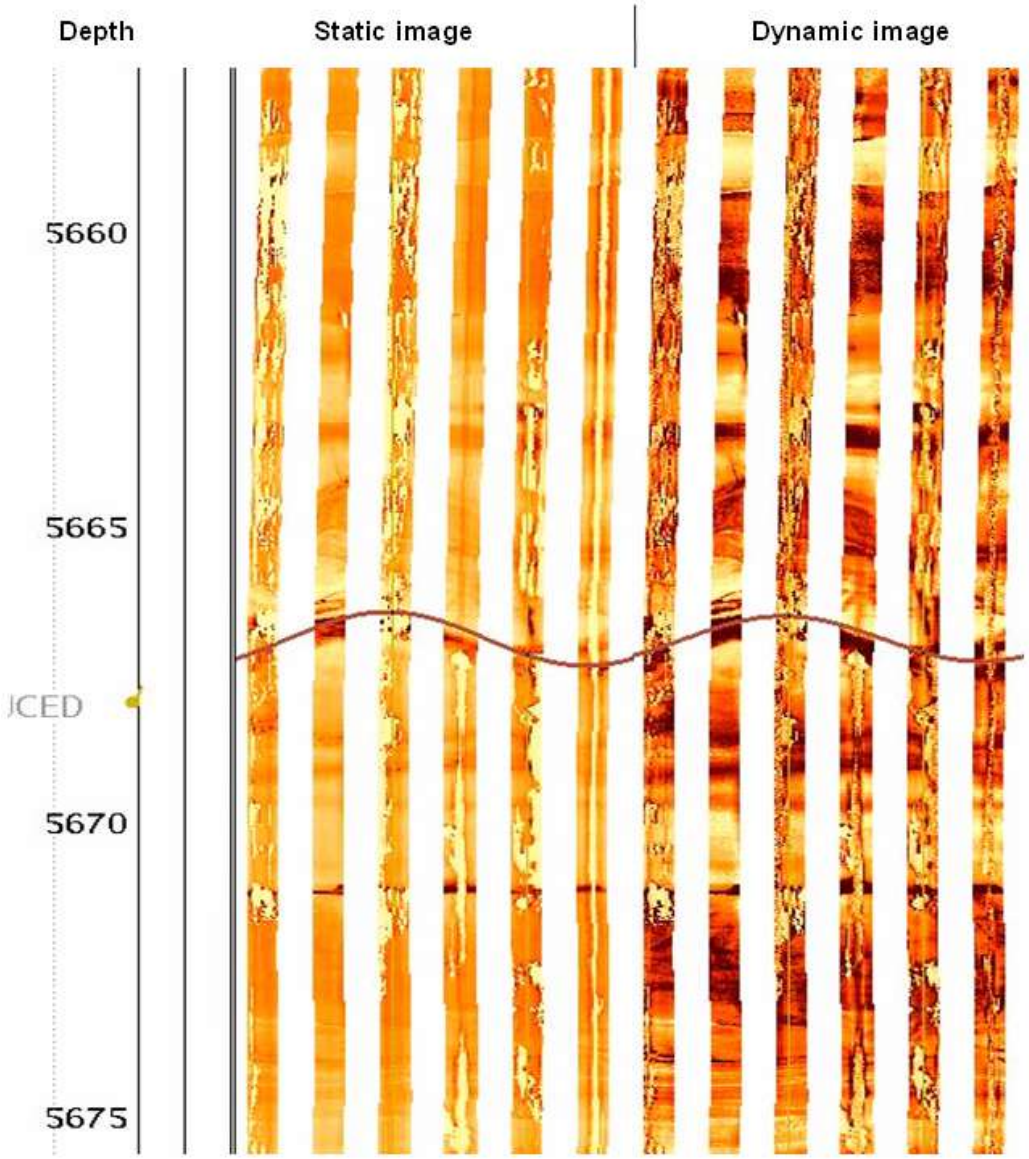

Figure 7.8. Inflection point at 5667 ft confirmed with fault in the RWF 542-20 image log. Depth scale in feet. Dip 45°; dip azimuth 316°.

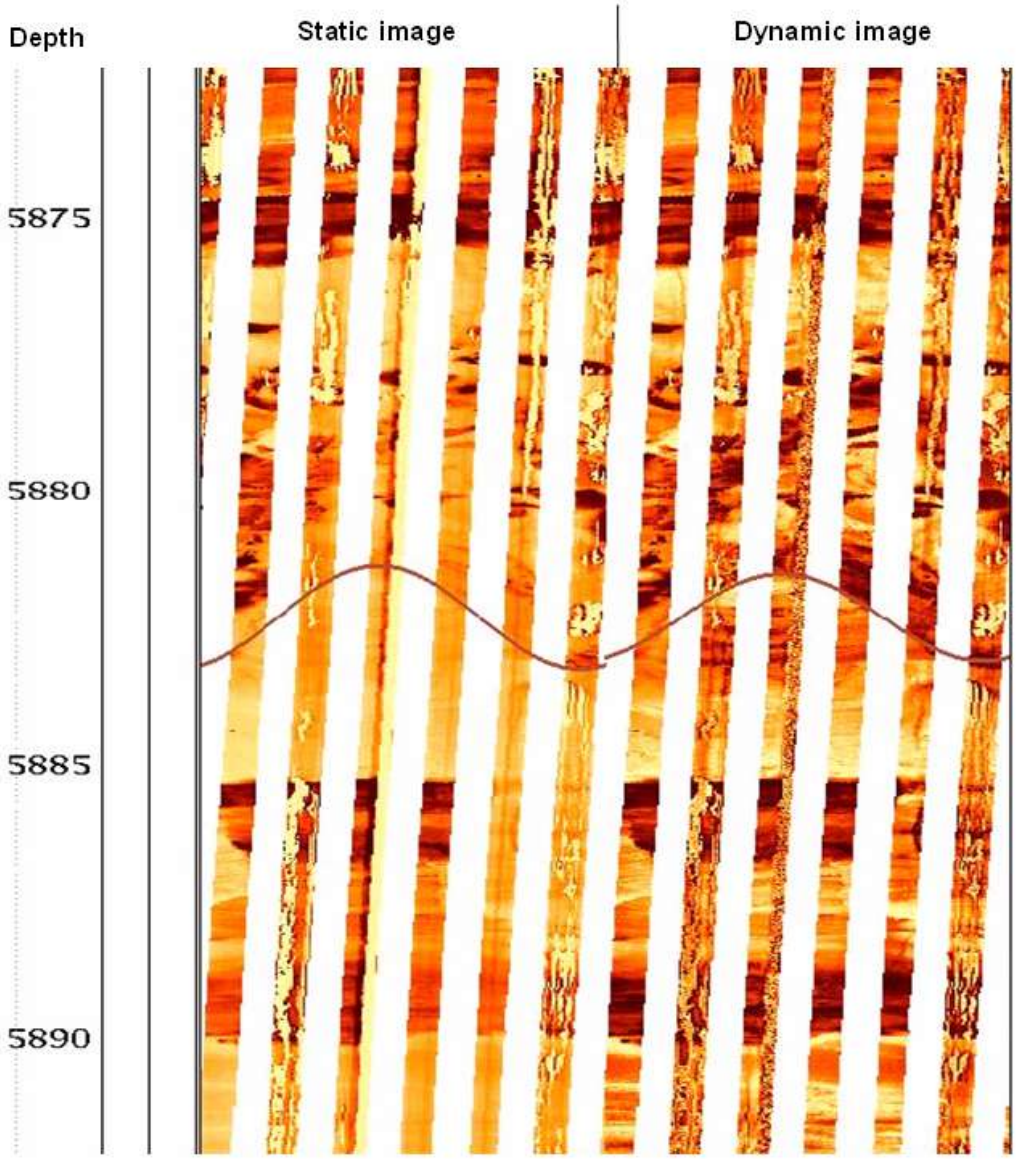

Figure 7.9. Inflection point at 5882 ft confirmed with fault in the RWF 542-20 image log. Breccia is present above the sine wave. Depth scale in feet. Dip 64^{o}; dip azimuth 338^{o}.

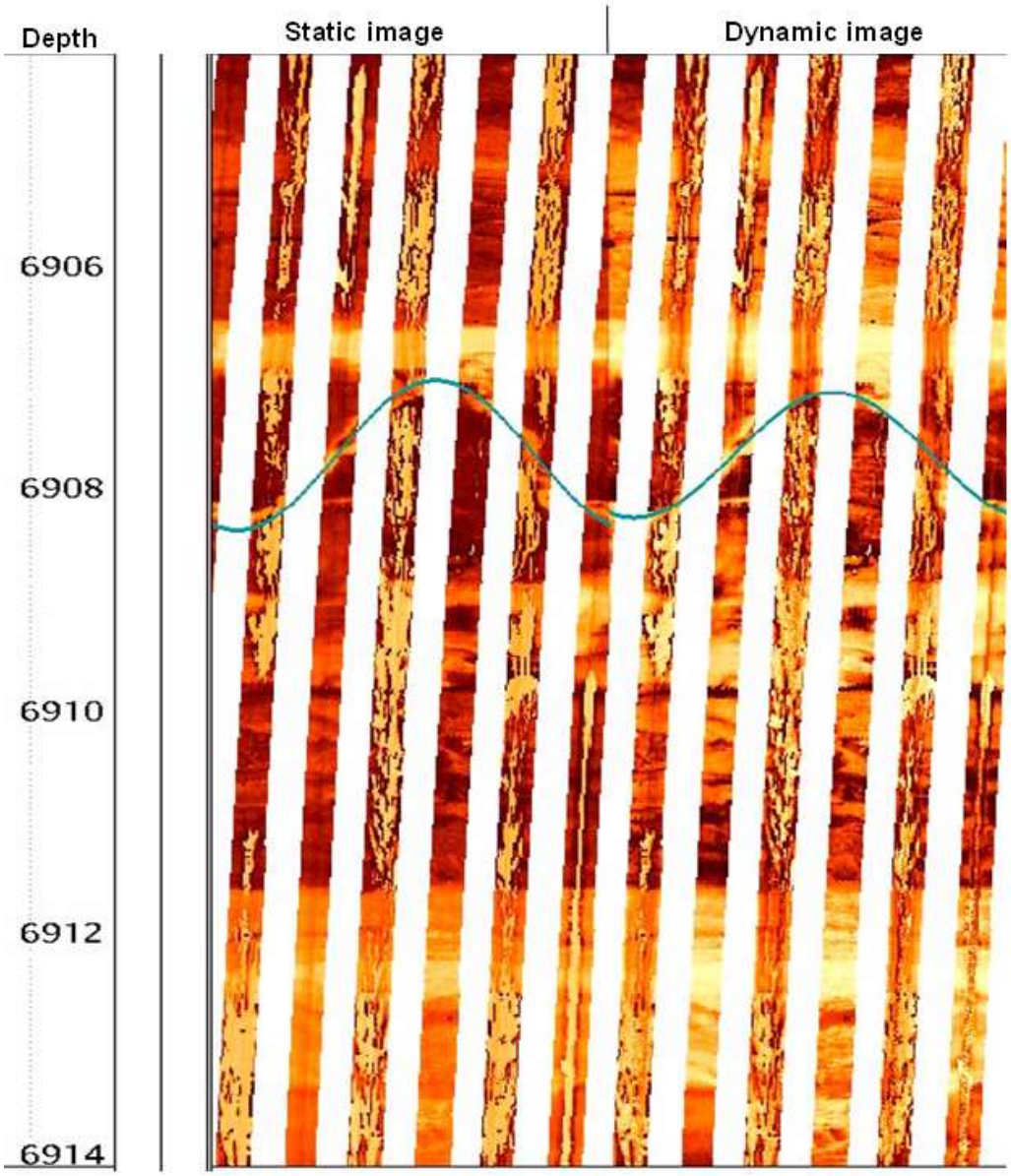

Figure 7.10. Inflection point at 6908 ft confirmed with the resistive fracture in the RWF 542-20 image log. Depth scale in feet. Dip 57°; dip azimuth 22°.

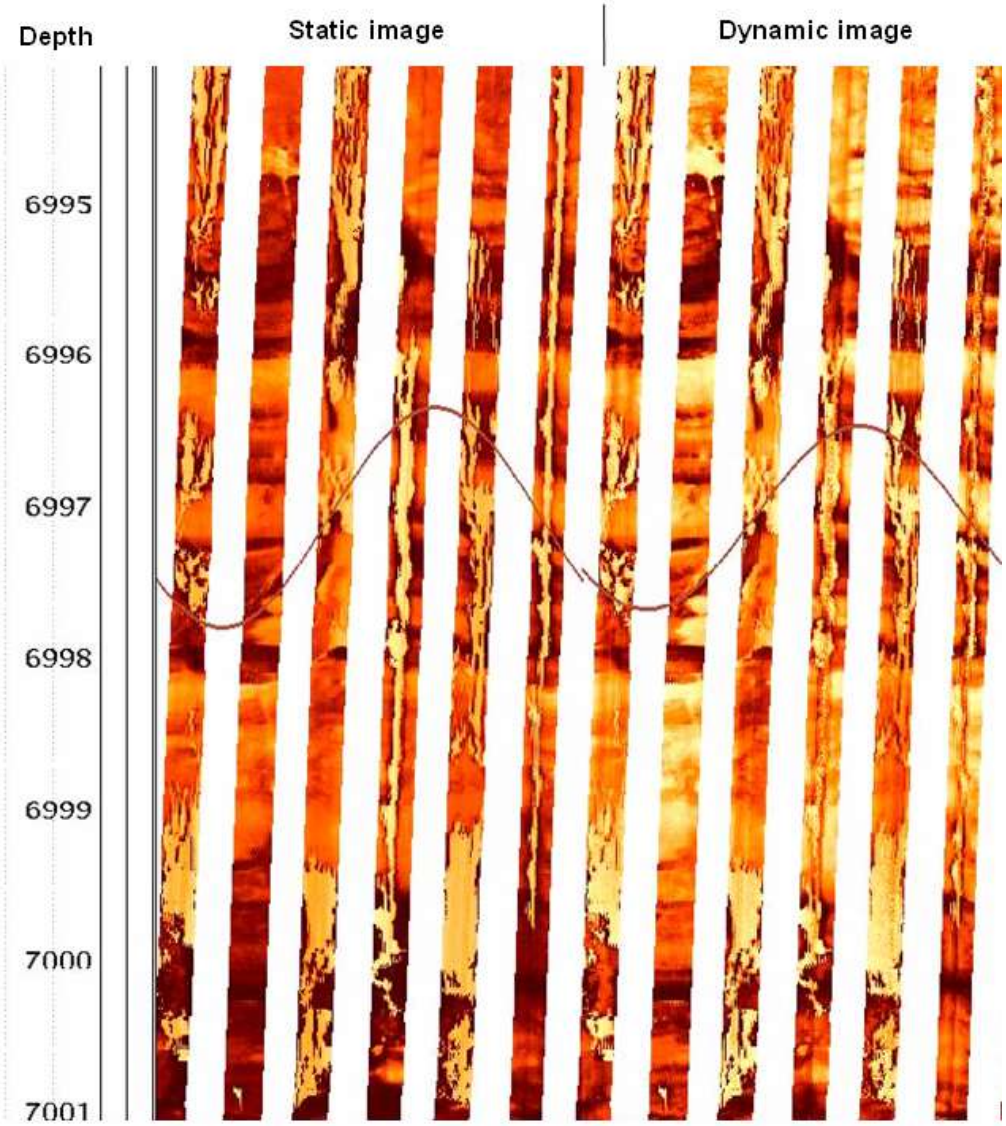

Figure 7.11. Inflection point at 6997 ft confirmed with the fault surface in the RWF 542-20 image log. Depth scale in feet. Dip 59°; dip azimuth 55°.

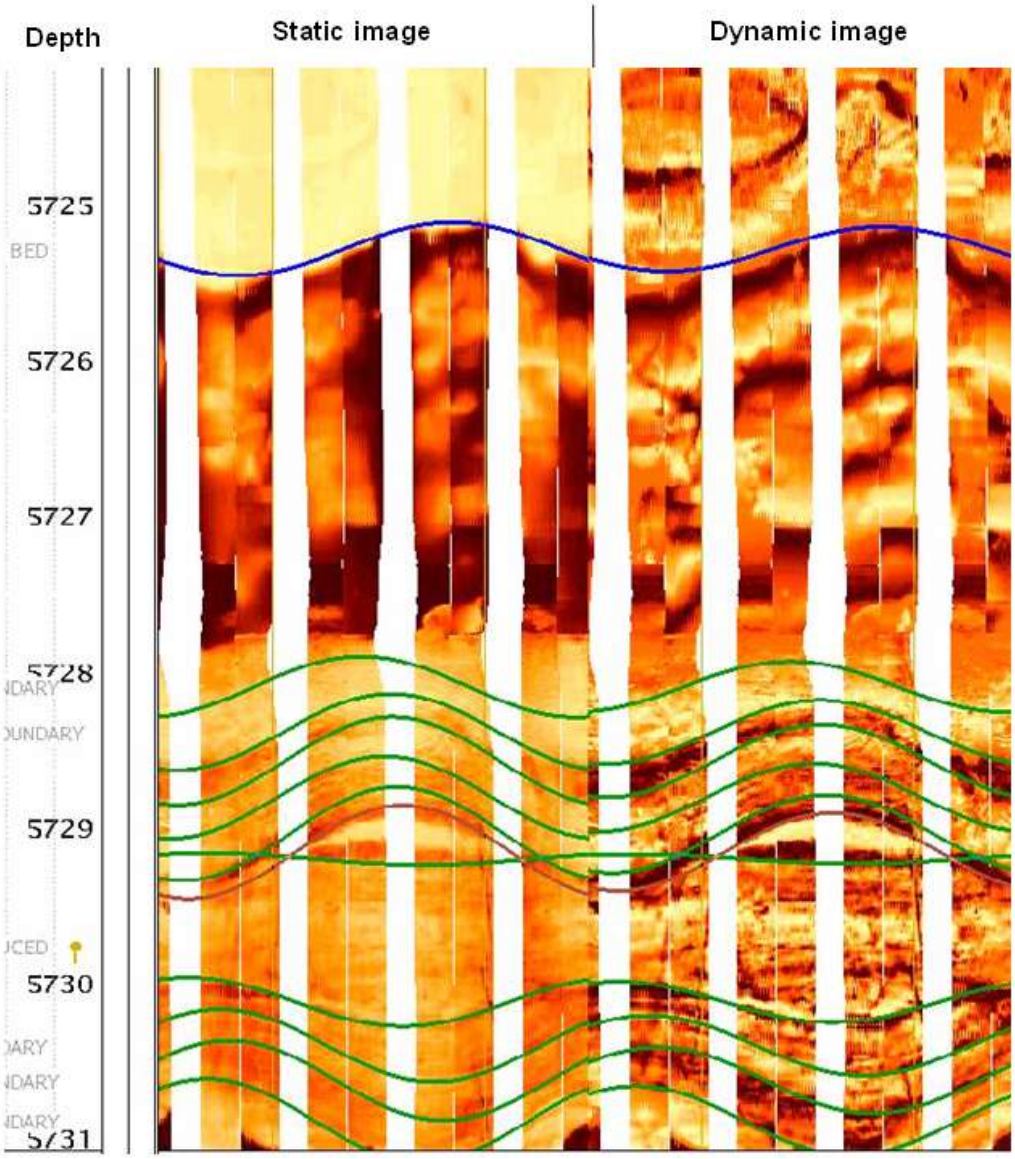

Figure 7.12. Inflection point at 5729 ft confirmed with the fault in the RWF 523-20 image log (brown sine wave). Depth scale in feet. Dip 39°; dip azimuth 22°.

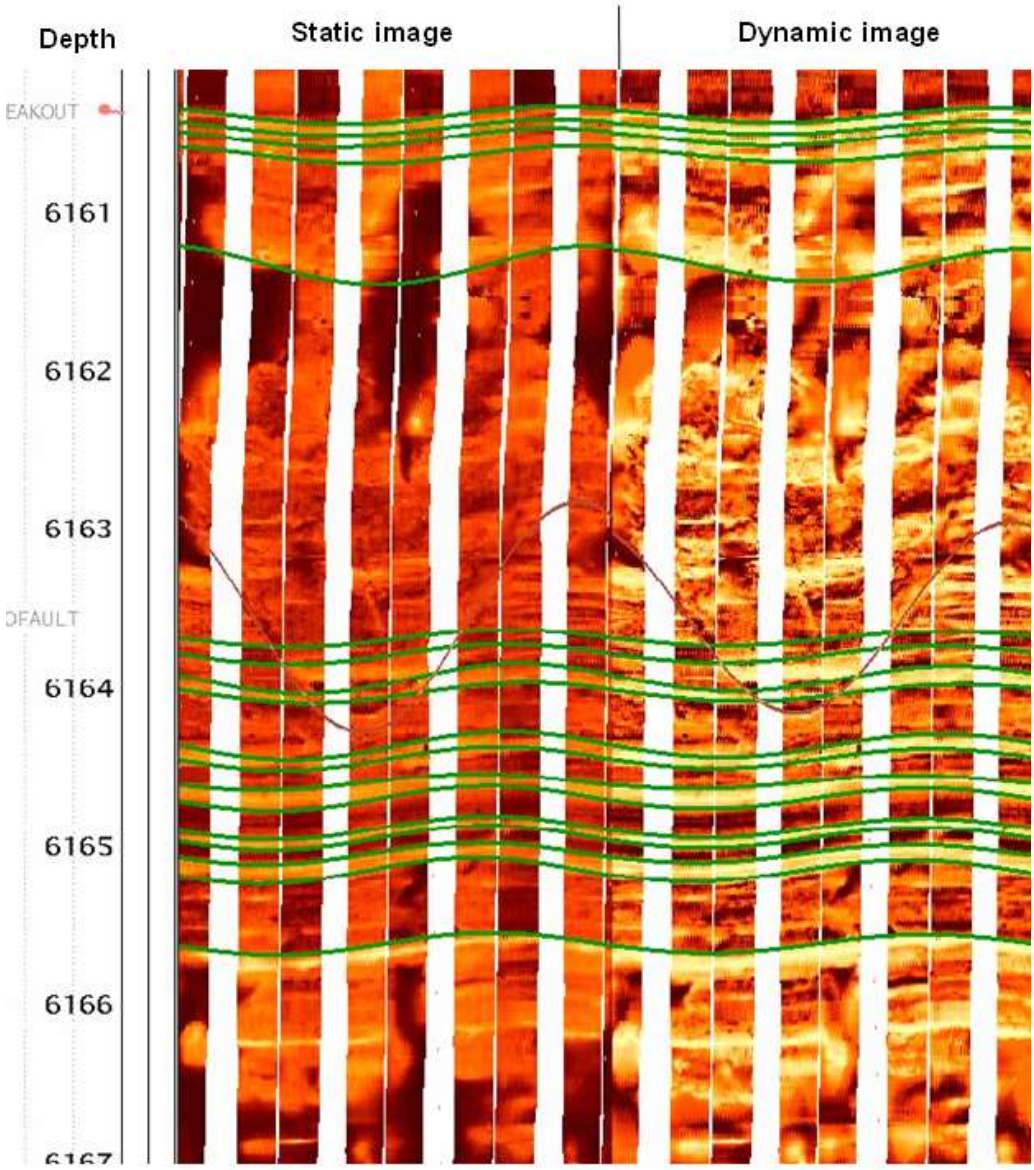

Figure 7.13. Inflection point at 6163 ft confirmed with the microfault in the RWF 523-20 image log (brown sine wave). Notice the offset of the sandstone layer on the opposite sides of the fault surface. Depth scale in feet. Dip 58^{o}; dip azimuth 152^{o}.

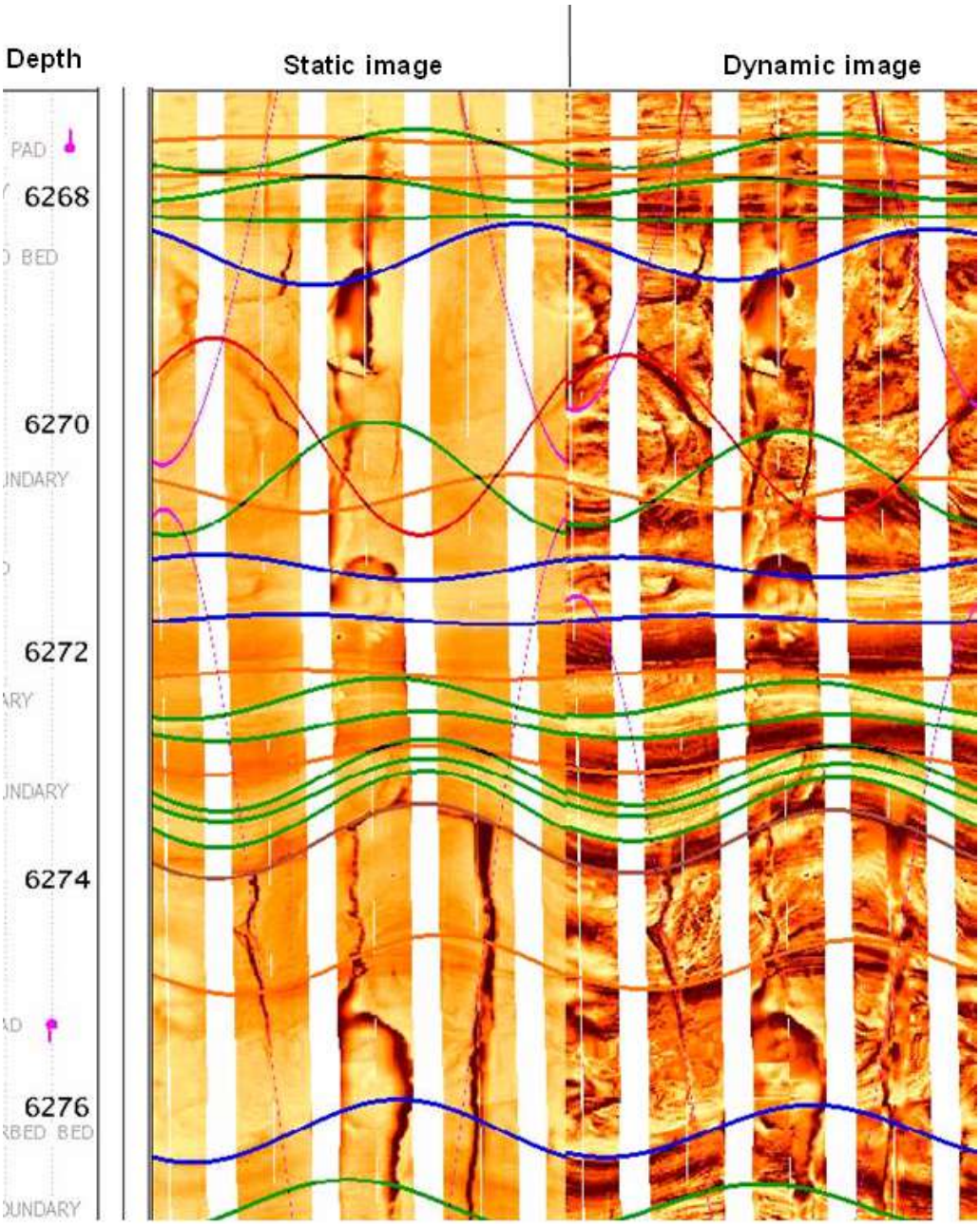

Figure 7.14. Inflection point at 6274 ft confirmed with the fault in the RWF 523-20 image log (brown sine wave). Notice the fractured character of the zone. Depth scale in feet. Dip 37°; dip azimuth 47°.

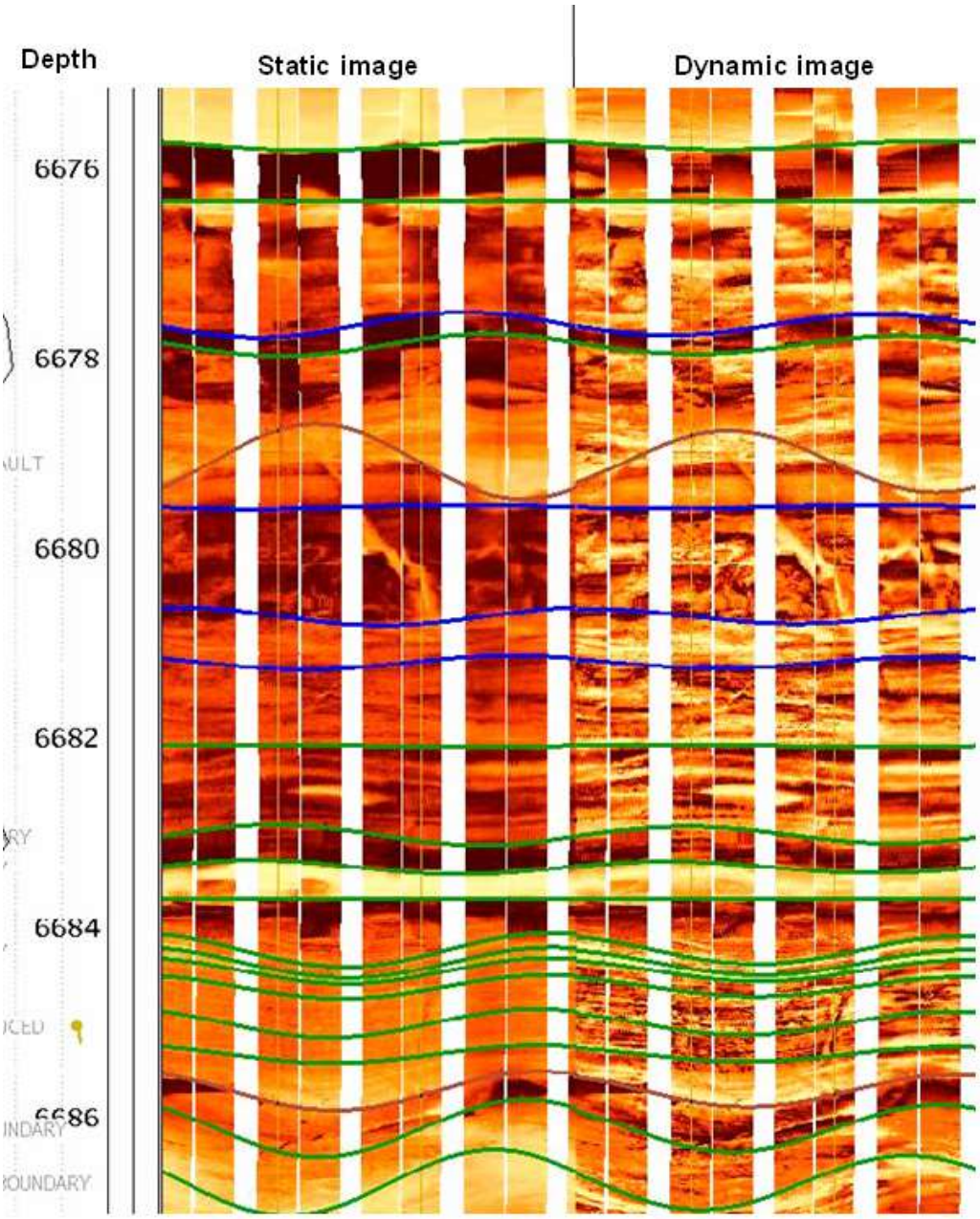

Figure 7.15. Inflection point at 6679 ft confirmed with the microfault in the RWF 523-20 image log (brown sine wave). Notice the offset of the shale layer on the opposite sides of the fault surface. Depth scale in feet. Dip 51^{o}; dip azimuth 312^{o}.

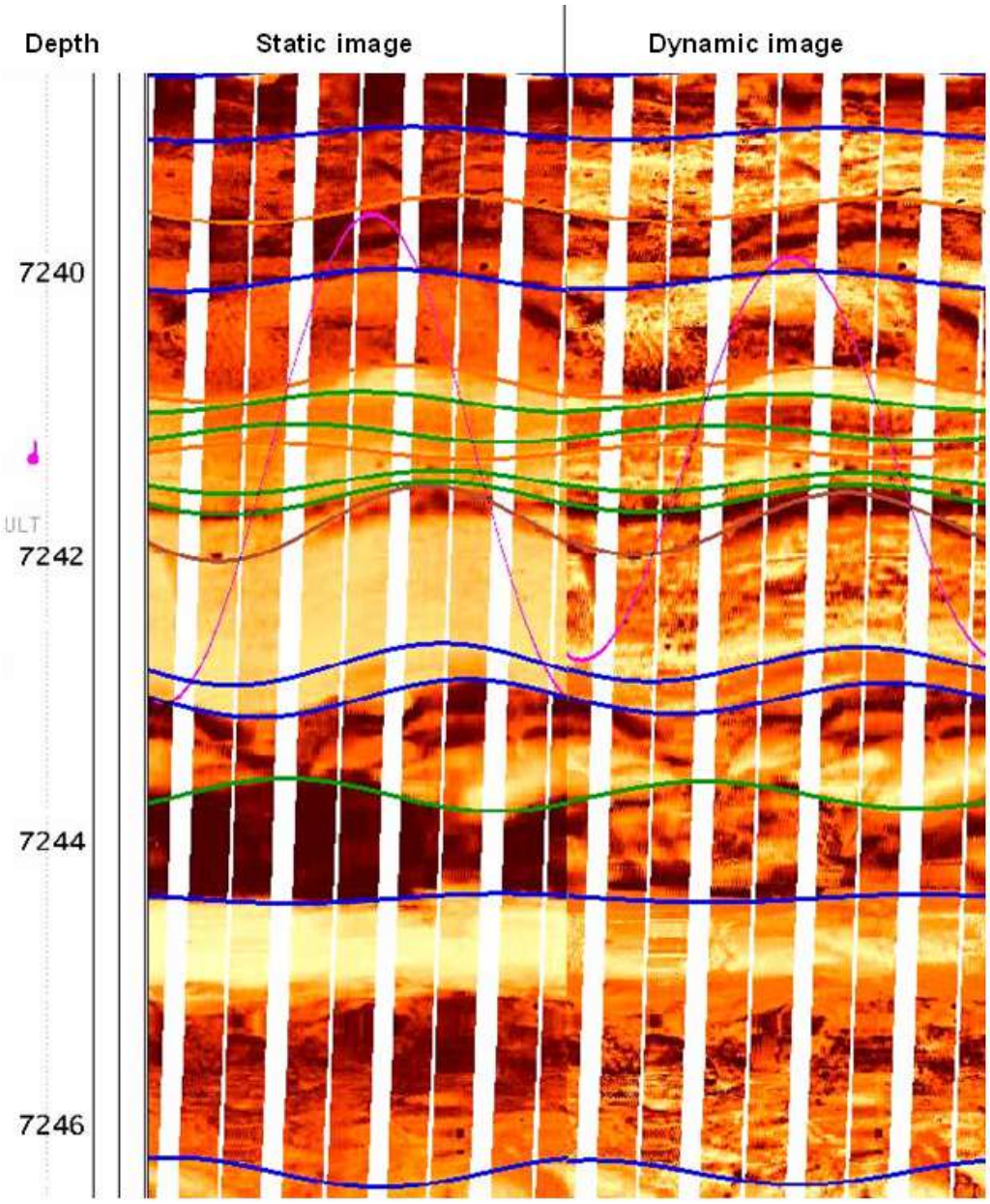

Figure 7.16. Inflection point at 7242 ft confirmed with the fault in the RWF 523-20 image log (brown sine wave). Notice the offset of the shale layer on the opposite sides of the fault surface. Depth scale in feet. Dip 30°; dip azimuth 51°.

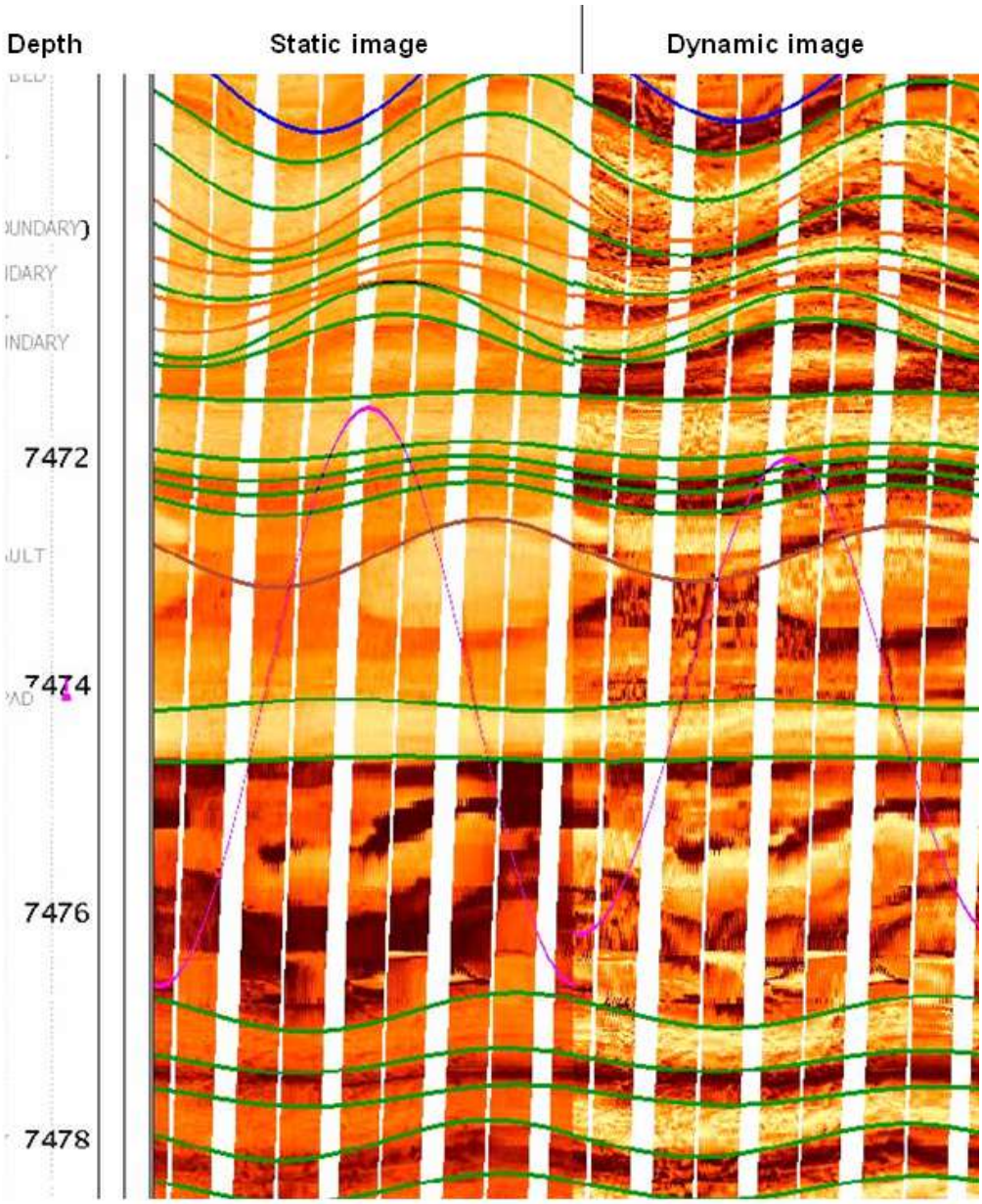

Figure 7.17. Inflection point at 7473 ft confirmed with the fault in the RWF 523-20 image log (brown sine wave). Notice the open fracture (pink sine wave) terminating at the fault surface. Depth scale in feet. Dip 31^{o}; dip azimuth 100^{o}.

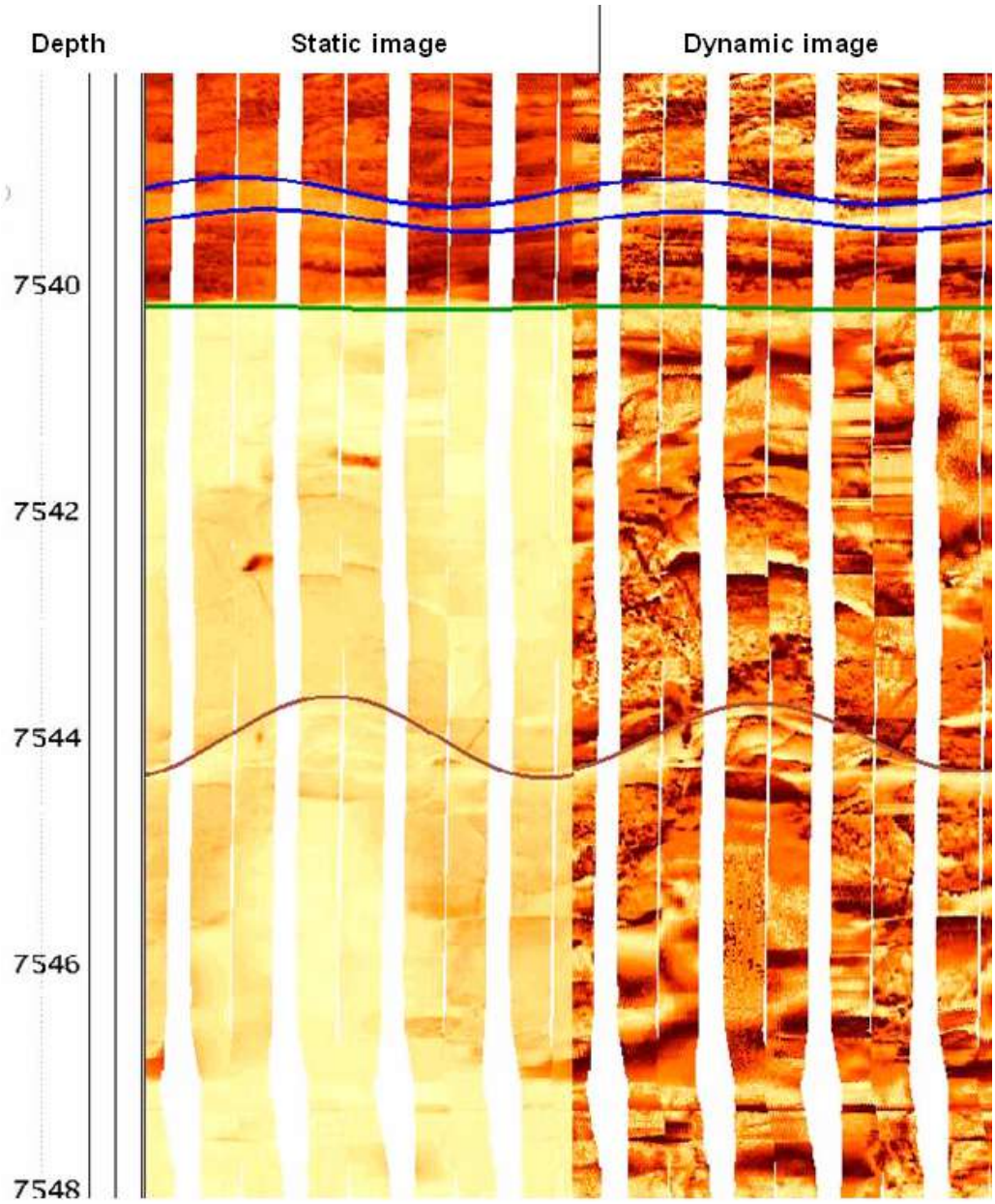

Figure 7.18. Inflection point at 7544 ft confirmed with the fault in the RWF 523-20 image log. Depth scale in feet. Dip 45°; dip azimuth 336°.

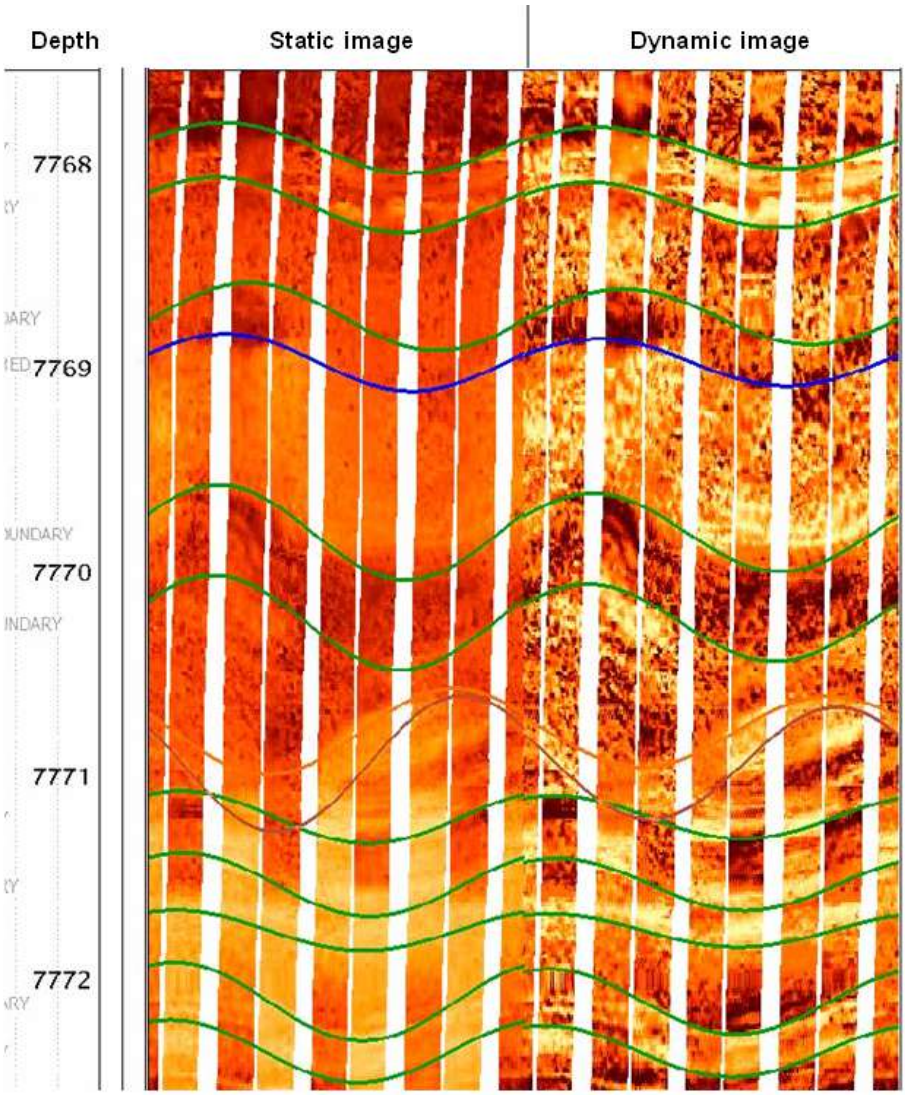

Figure 7.19. Inflection point at 7771 ft confirmed with the fault in the RWF 523-20 image log (brown sine wave). Depth scale in feet. Dip 35°; dip azimuth 119°.

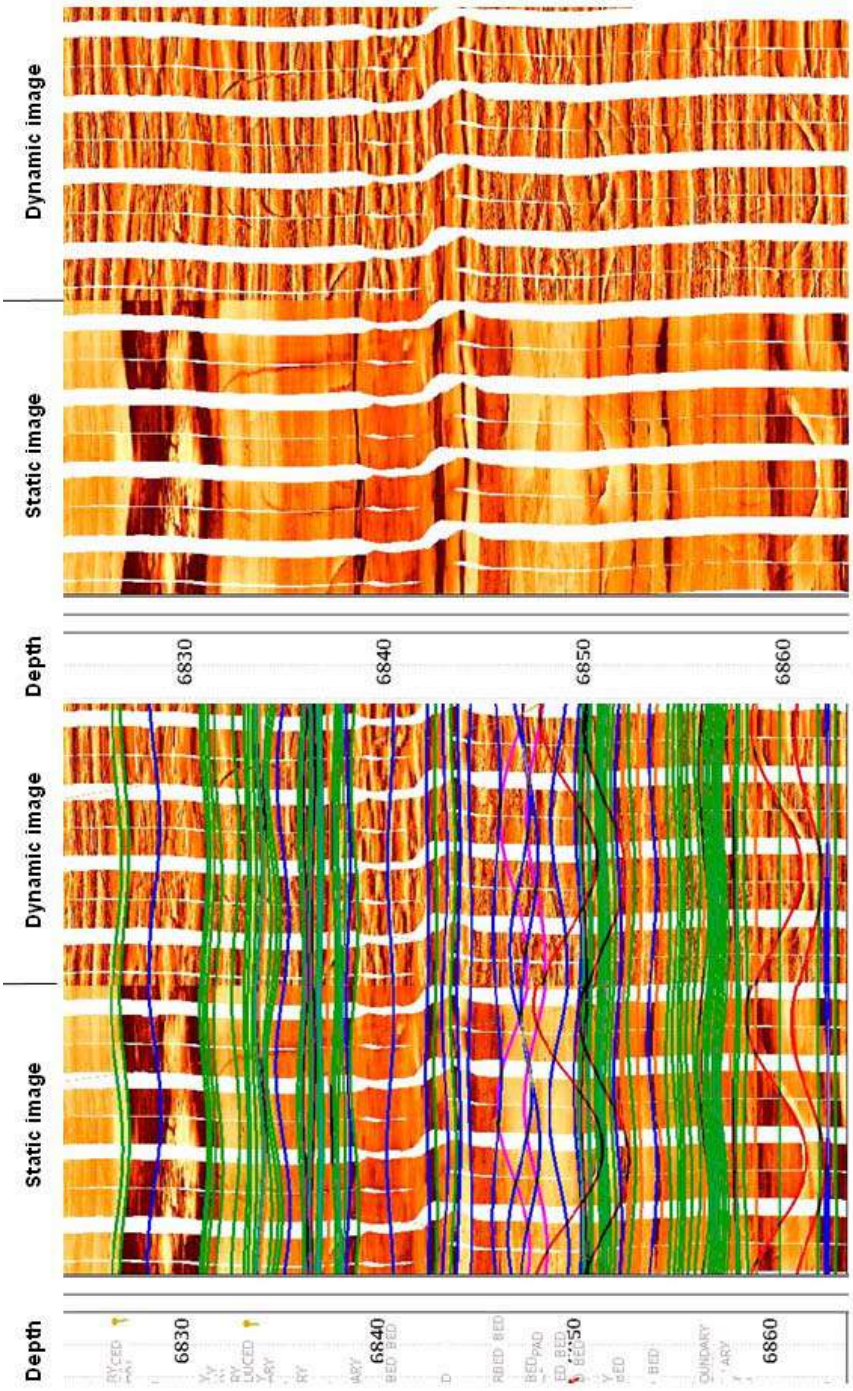

Figure 7.20. Zone of erratic vectors in dip azimuth vector plot, from 6823 to 6863 ft confirmed with the fault zone in the RWF 523-20 image log. Left: interpreted image; right: noninterpreted image. Notice the resistive natural fractures, interpreted red and pink sine waves. The fault zone might be noticed on seismic-scale data. Depth scale in feet.

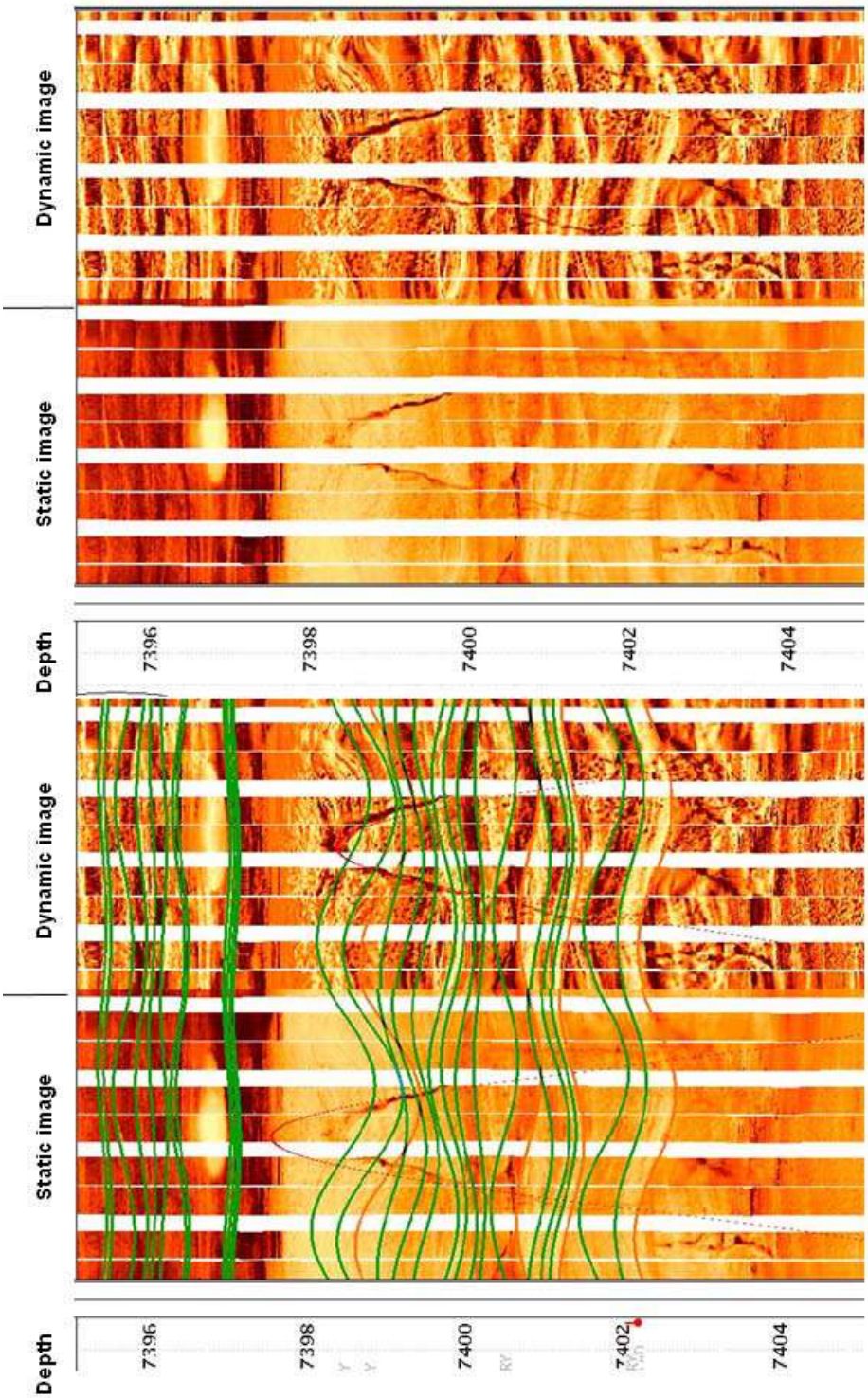

Figure 7.21. Inflection point in plots confirmed with the fault zone (7398 to 7403 ft) in the the RWF 523-20 image log. Left:interpreted image; right: noninterpreted image. Notice the natural open fracture (red sine wave) associated with irregular fractures. Depth scale in feet.

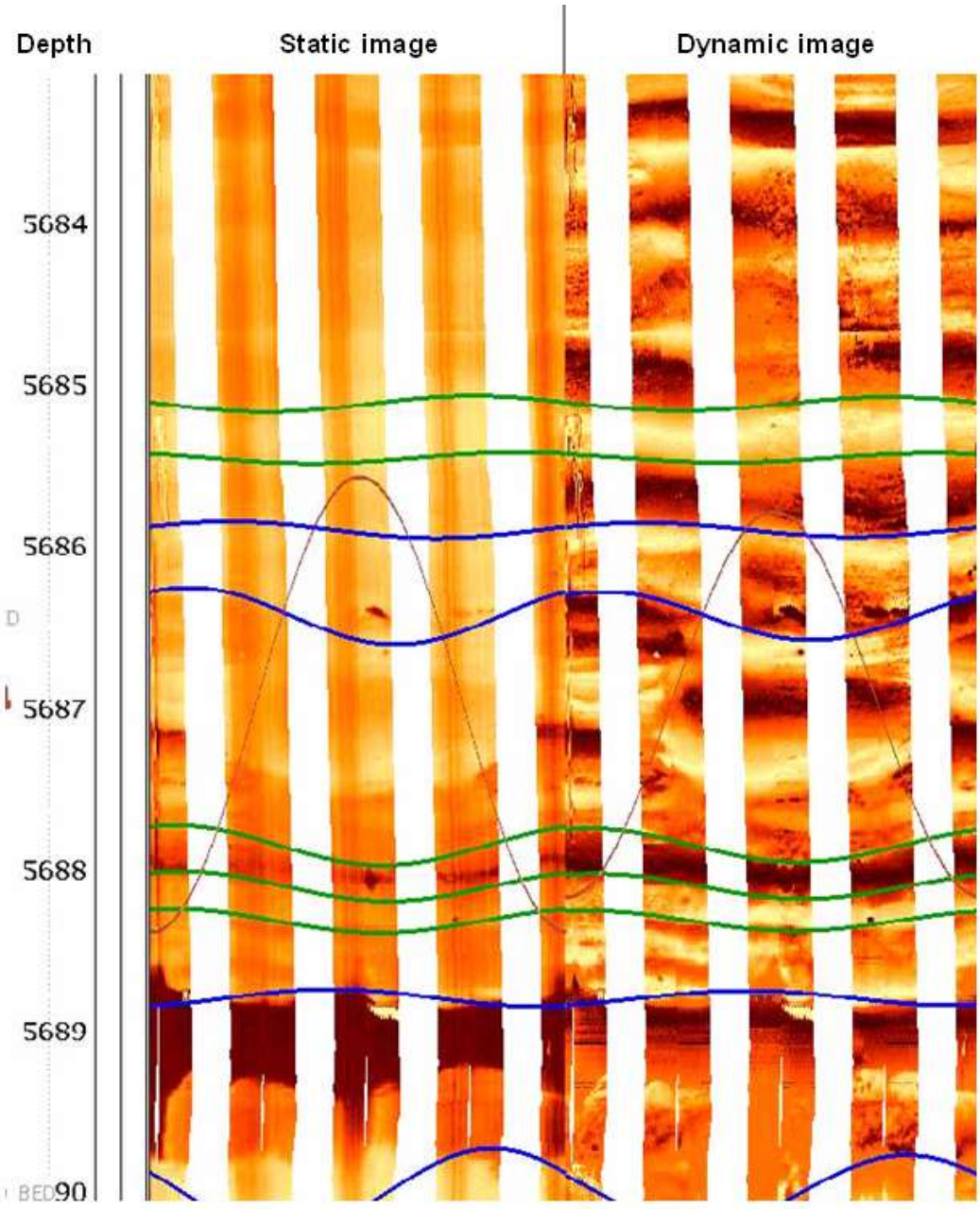

Figure 7.22. Inflection point at 5687 ft confirmed with the fault in the RMV 60-17 image log (brown sine wave). Depth scale in feet. Dip 73°; dip azimuth 0°.

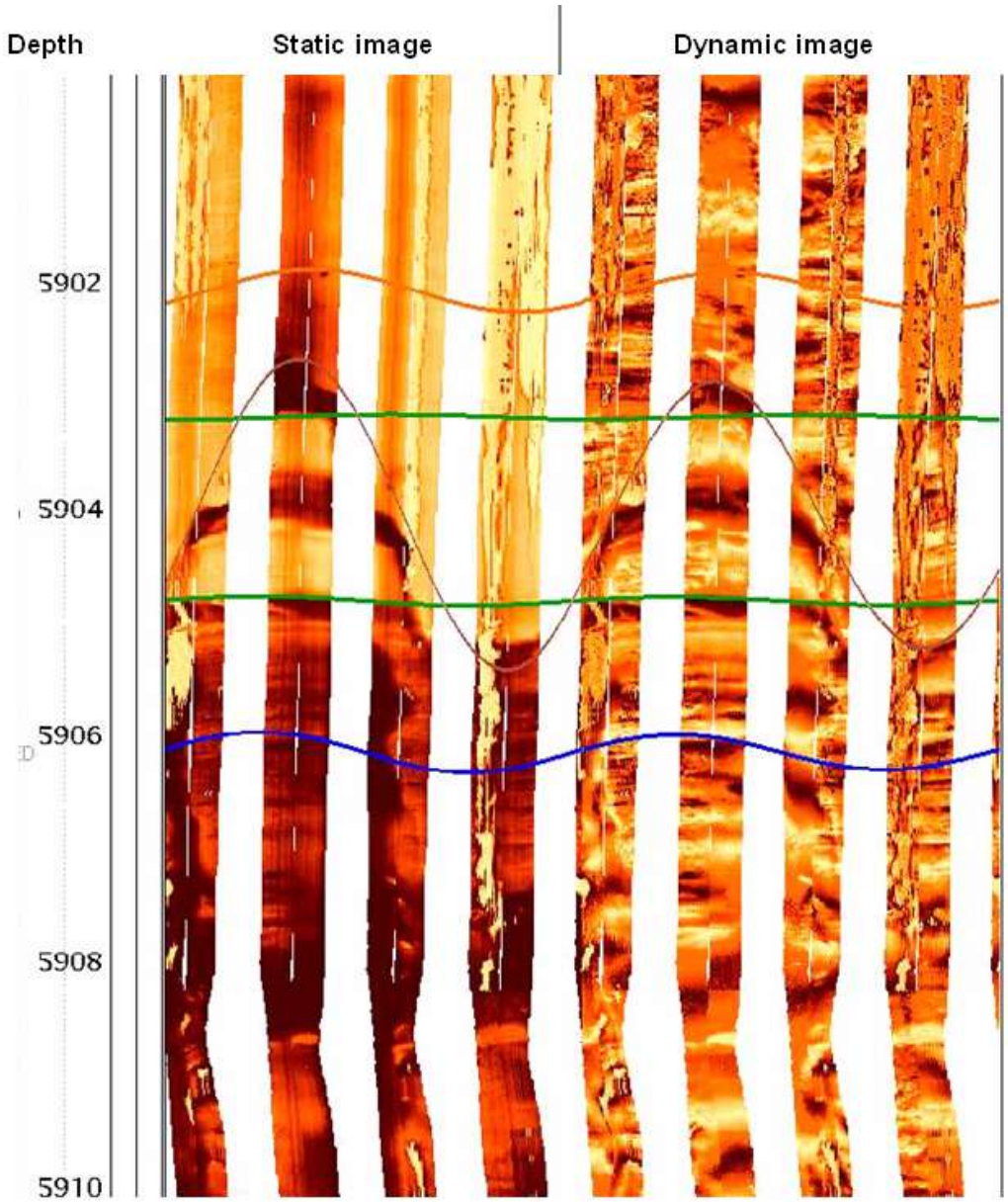

Figure 7.23. Inflection point at 5904 ft confirmed with the fault in the RMV 60-17 image log (brown sine wave). Depth scale in feet. Dip 71°; dip azimuth 295°.

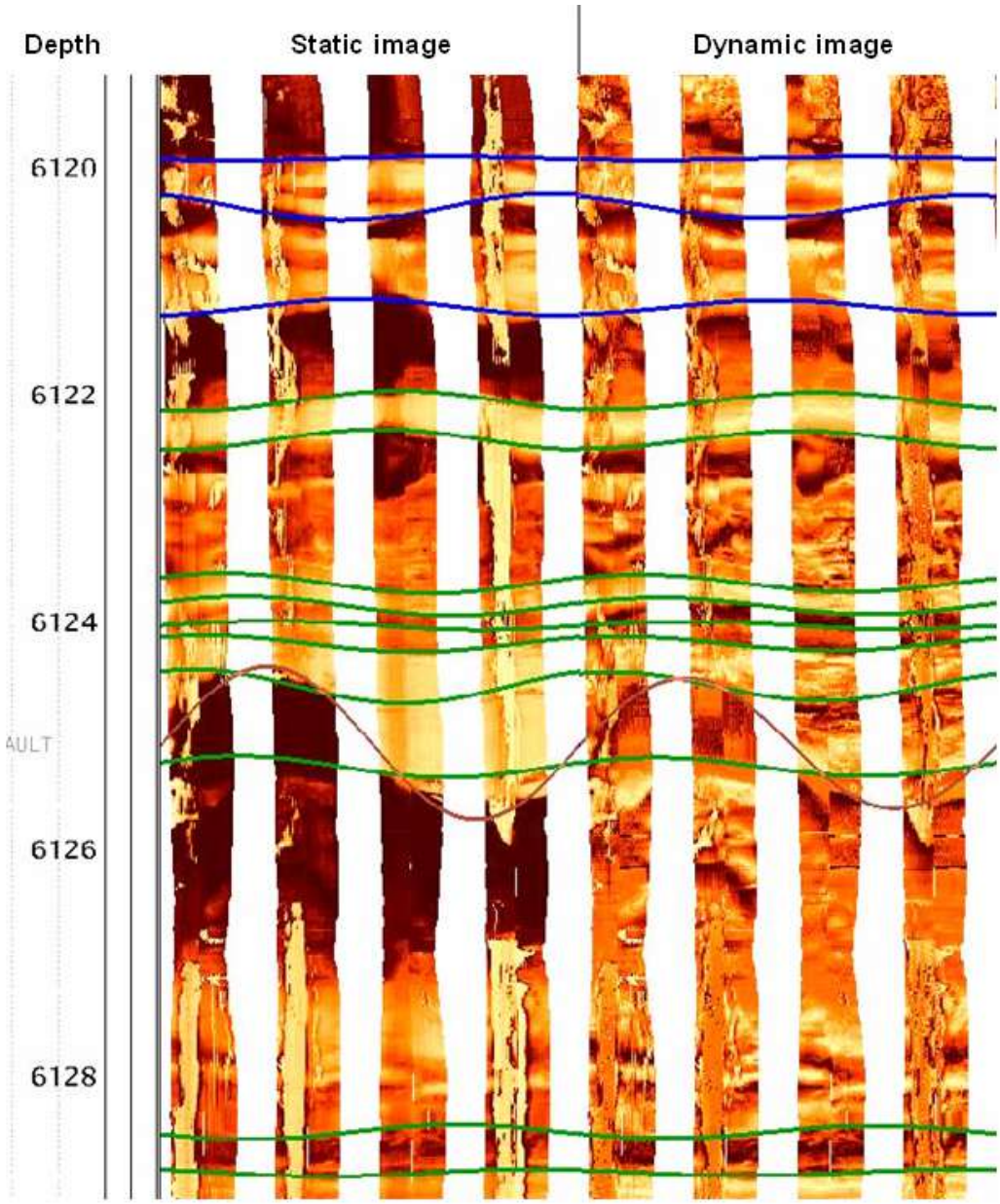

Figure 7.24. Inflection point at 6125 ft confirmed with the fault in the RMV 60-17 image log (brown sine wave). Depth scale in feet. Dip 54°; dip azimuth 273°.

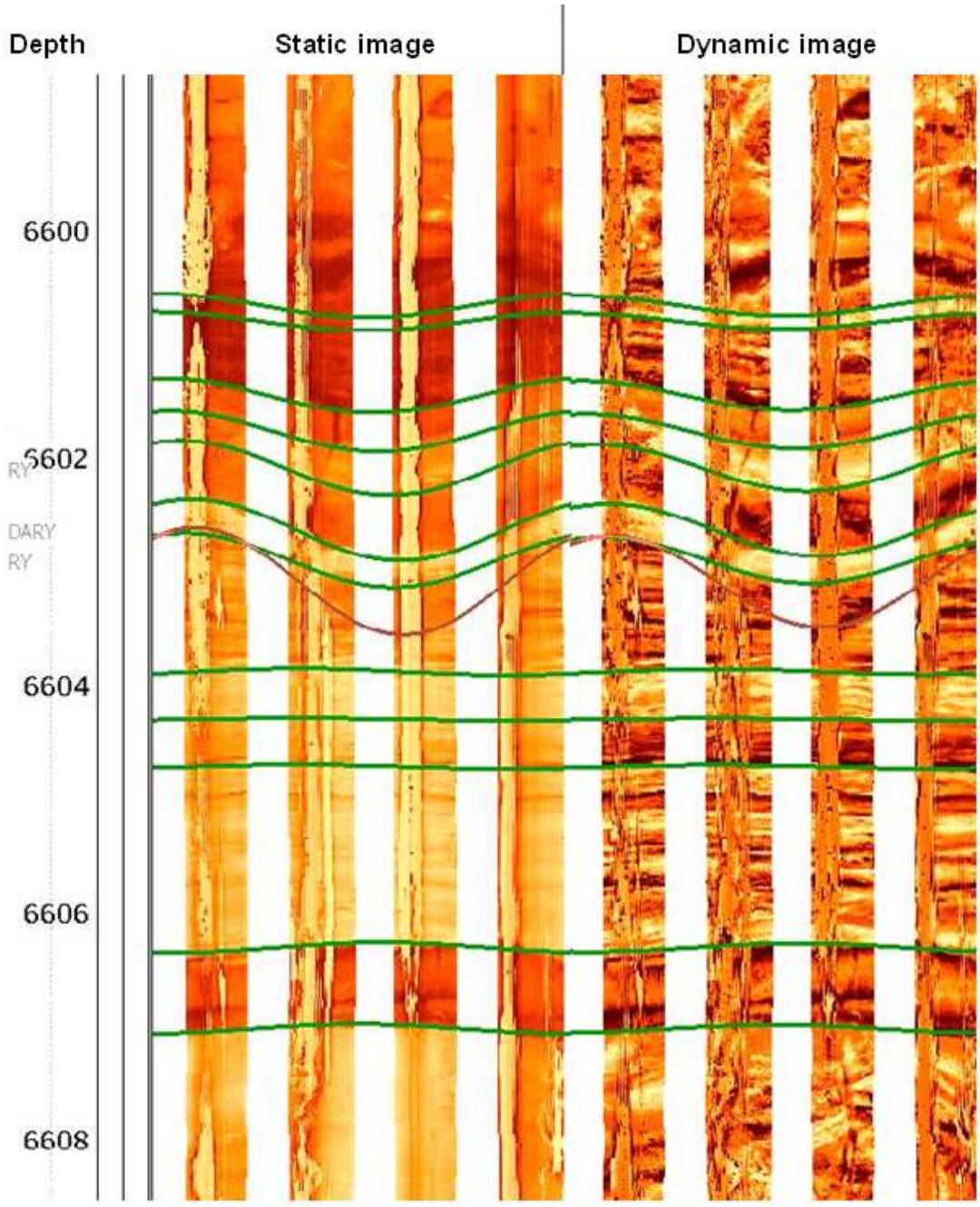

Figure 7.25. Inflection point at 6603 ft confirmed with the fault in the RMV 60-17 image log (brown sine wave). Depth scale in feet. Dip 43°; dip azimuth 128°.

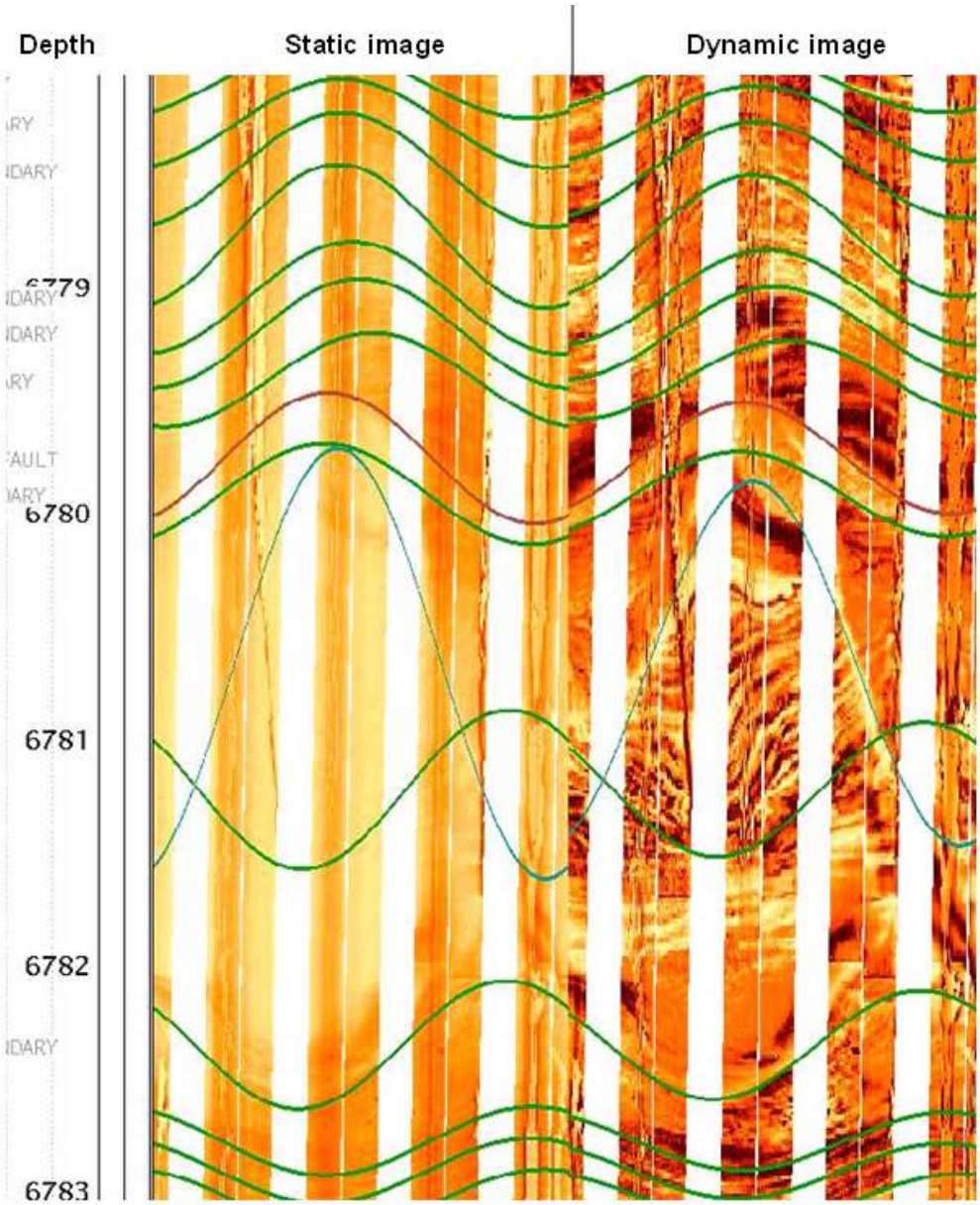

Figure 7.26. Inflection point at 6781 ft confirmed with the fault in the RMV 60-17 image log (blue-green sinewave). Notice the resistive character of the fault surface. Beds below the fault appear to be deformed. Depth scale in feet. Dip 65°; dip azimuth 339°.

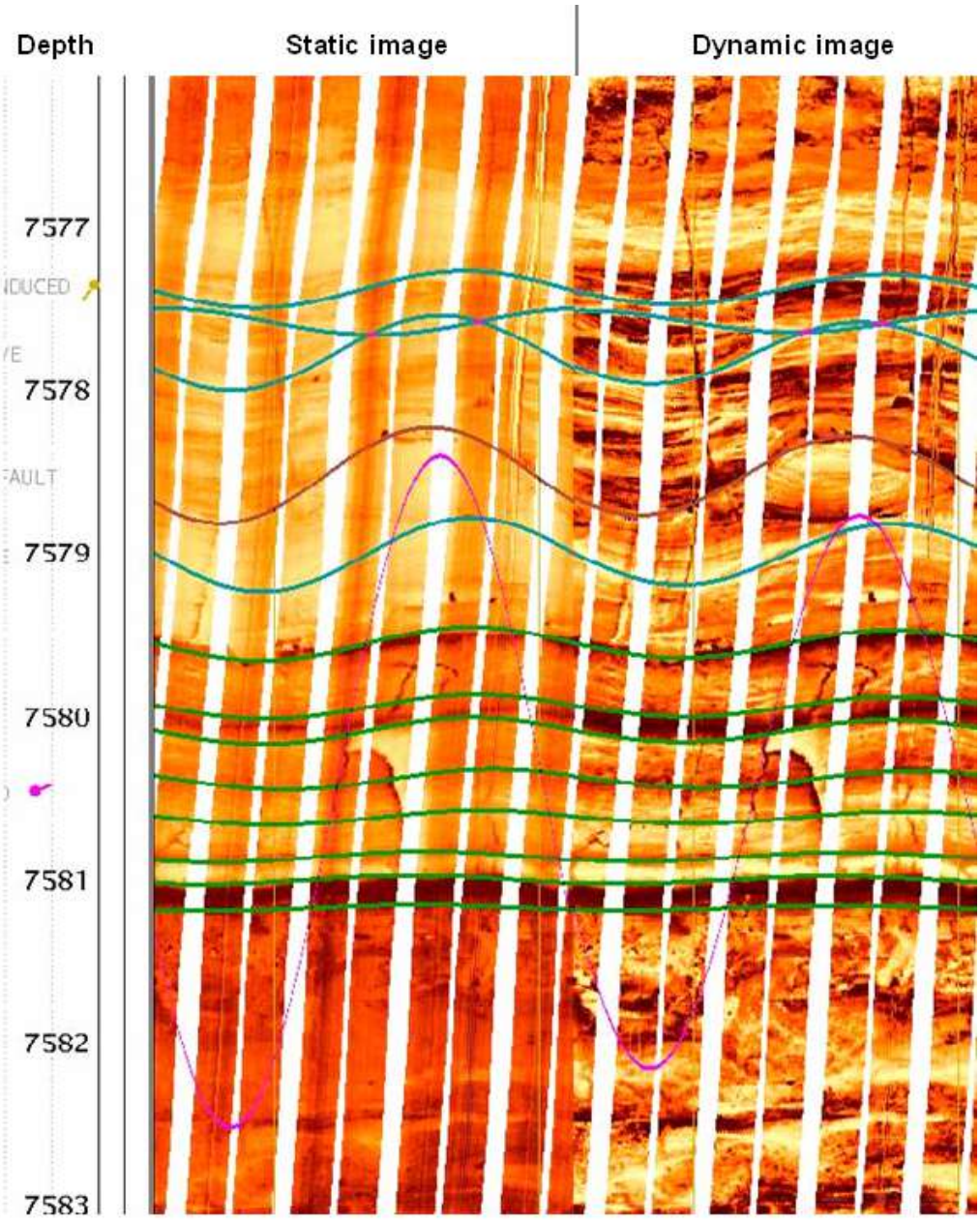

Figure 7.27. Inflection point at 7578.5 ft confirmed with the fault in the RMV 60-17 image log (brown sine wave). Notice the associated resistive fractures below and above (blue-green sinewave). Depth scale in feet. Dip 35°; dip azimuth 53°.

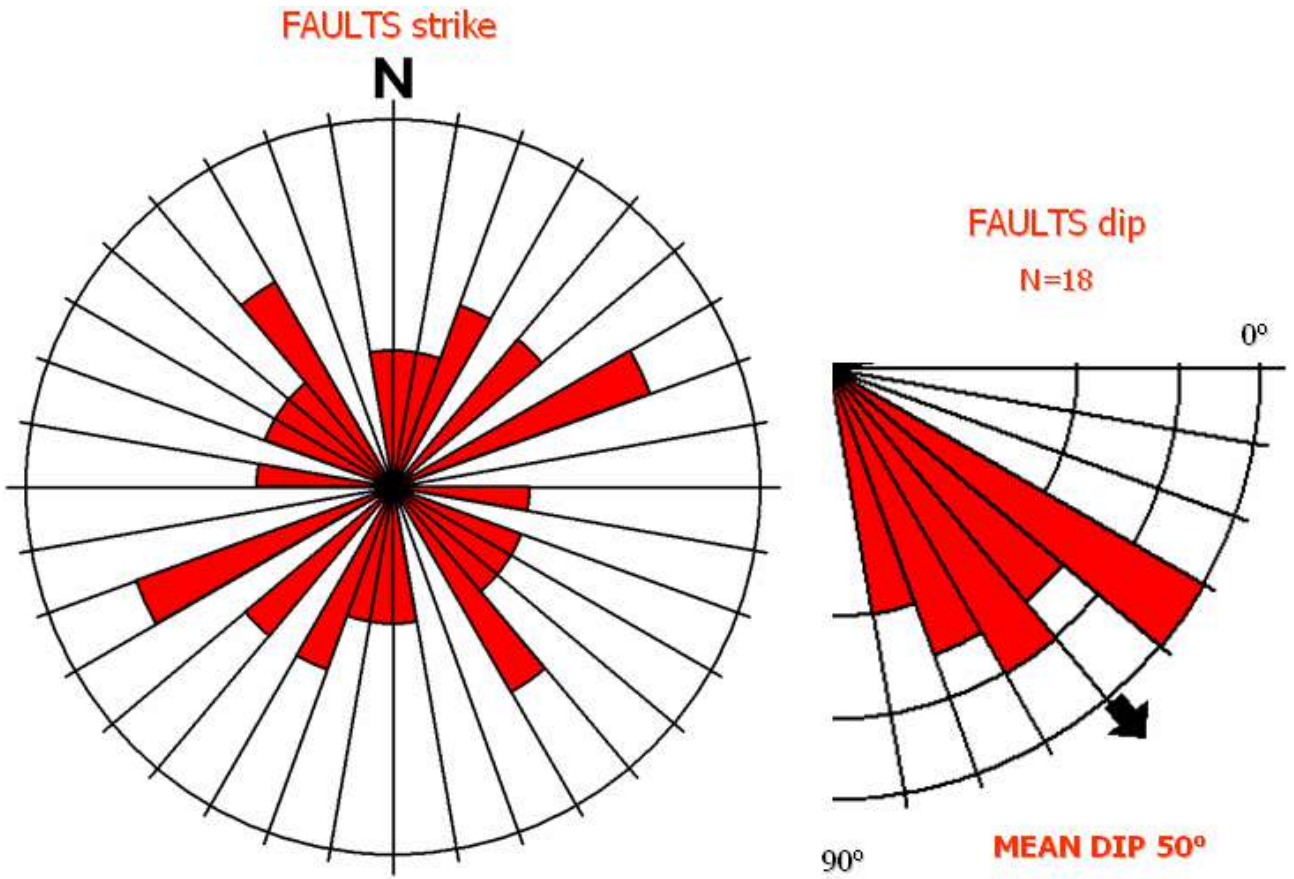

Figure 7.28. Strike and dip rose diagram of 18 interpreted fault surfaces. Two classes of fault strikes show relatively higher frequency (55° and 345°). The dip rose diagram shows a mean value of 50°.

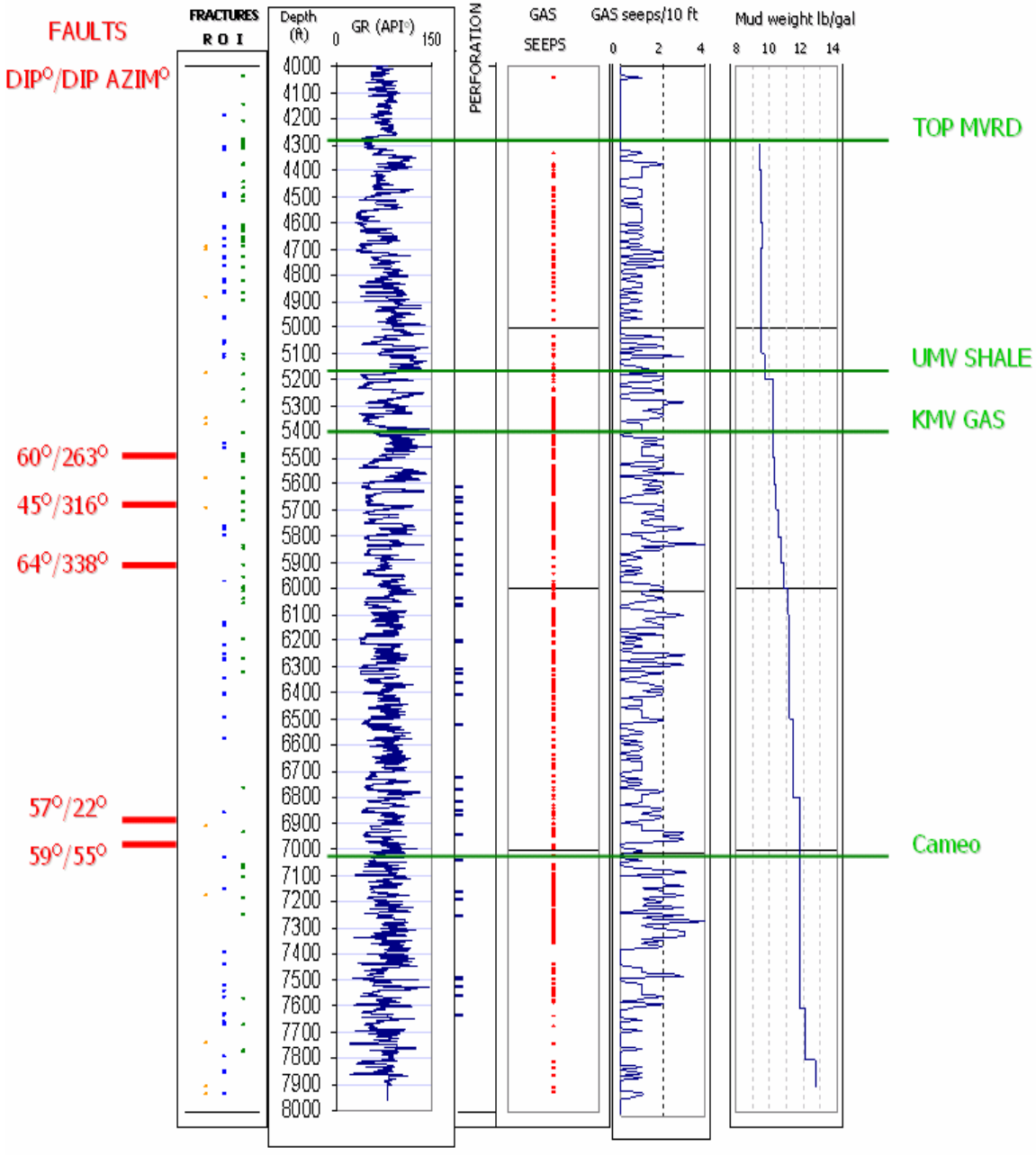

Figure 7.29. Combination of the fault position, fracture, GR of imaged interval, perforation, gas seep, gas-seep density (number of gas seeps per 10 ft) and mud-weight logs in the RWF 542-20 well. Abbreviations: R=resistive fractures; O= open fractures; I= drilling induced fractures.

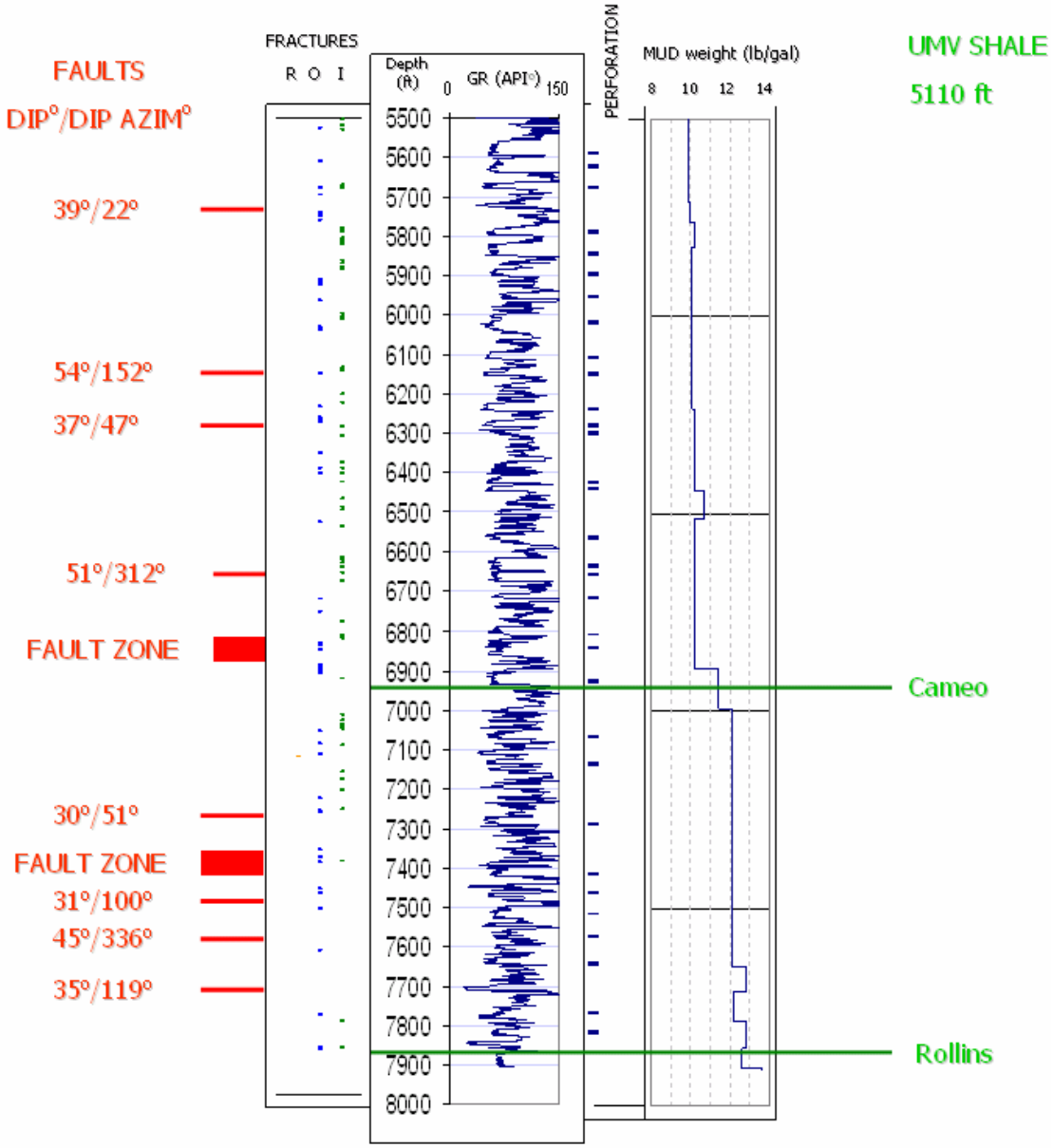

Figure 7.30. Combination of the fault, fracture, GR of imaged interval, perforation and mud-weight logs in the RWF 523-20 well. There are no gas seeps present in the image log. Abbreviations: R=resistive fractures; O= open fractures; I= drilling induced fractures.

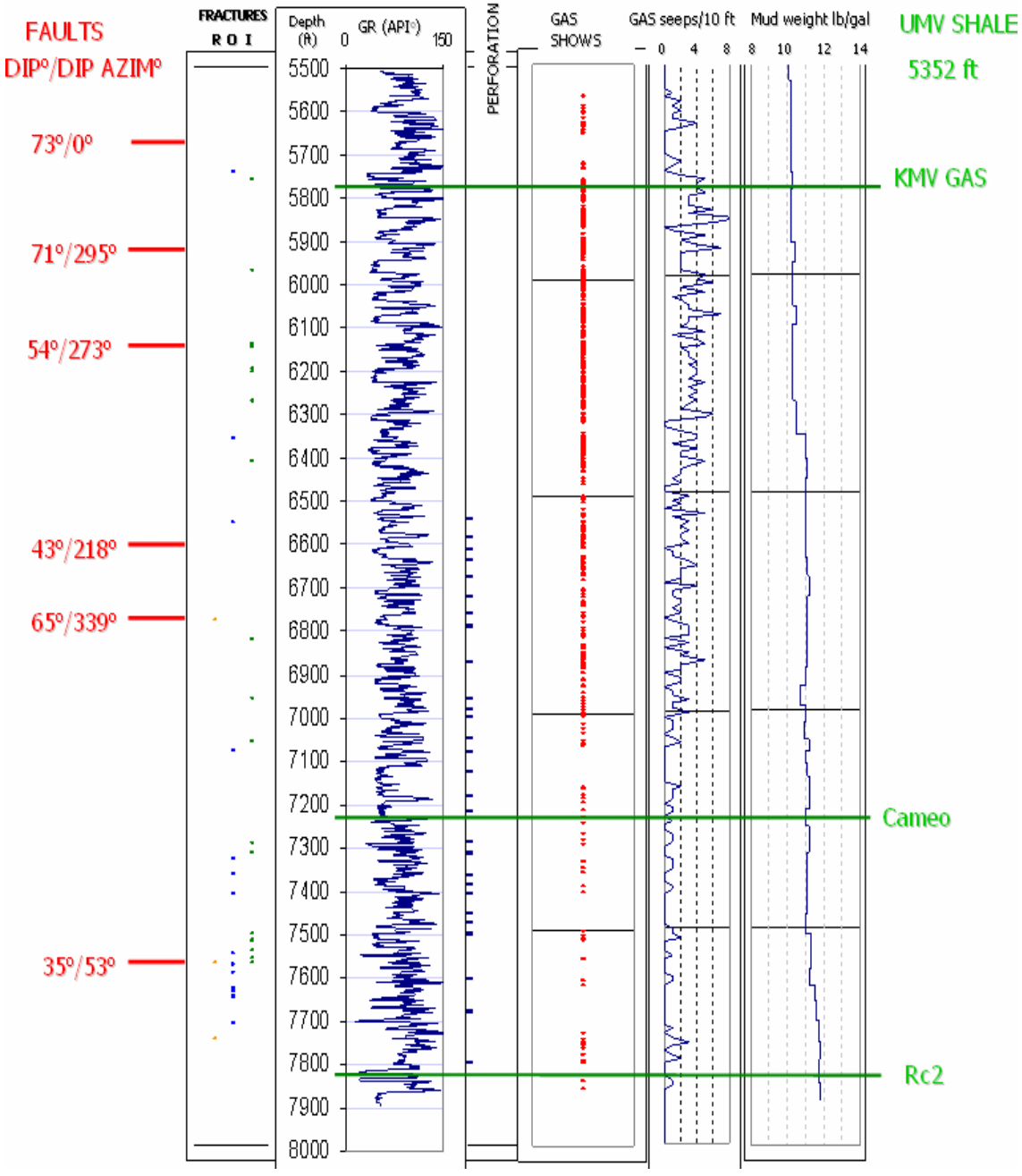

Figure 7.31. Combination of the fault position, fracture, GR of imaged interval, perforation, gas seep, gas-seep density (number of gas seeps per 10 ft) and mud-weight logs in the RMV 60-17 well. Abbreviations: R=resistive fractures; O= open fractures; I= drilling induced fractures.

Two fault zones and 18 fault surfaces were interpreted in both dip-domain analyses and image logs for wells RWF 542-20, RWF 523-20, and RMV 60-17. This information helps to relate features on different scales of investigation. The interpreted depths, dips and dip azimuths of the faults can be observed in the borehole compared with the corresponding geometrical features of the seismic-scale faults (Chapter 8).

The other inflection points interpreted in dip-domain analyses, which do not have evidence in the image logs, are also probably small-scale faults.

In the Halliburton report for the RWF 441-20 well, no fault surfaces were reported. Furthermore, only the set of fractures parallel to SHmax was encountered in the well (Chapter 5). Secondary N30^{o}W and N60^{o}E fracture or fault trends (Kuuskraa et al. 1997), associated with the larger-scale structural features, are absent. This might indicate that the well was drilled away from the larger-scale structural features.

One class of fault orientations (strike azimuth 345^{o}) shows a good match with the seismic-scale orientation of faults interpreted by Cumella and Ostby (2003) (Figure 7.32). The seismic survey in their work was named the “Seitel survey”. In the same work, the authors proposed a left-lateral slip kinematic model. Following that idea, and plotting the mean orientations of the structural features in this study (Figure 7.33), I propose a left-lateral shear-stress model. All of the orientations of the structural elements such as stress, fractures, and faults show a good match with the proposed model. Stress-axis orientation matches the present-day extensional regime in the Piceance basin. Drilling induced, open natural fractures and one class of resistive fractures are aligned with the principal stress

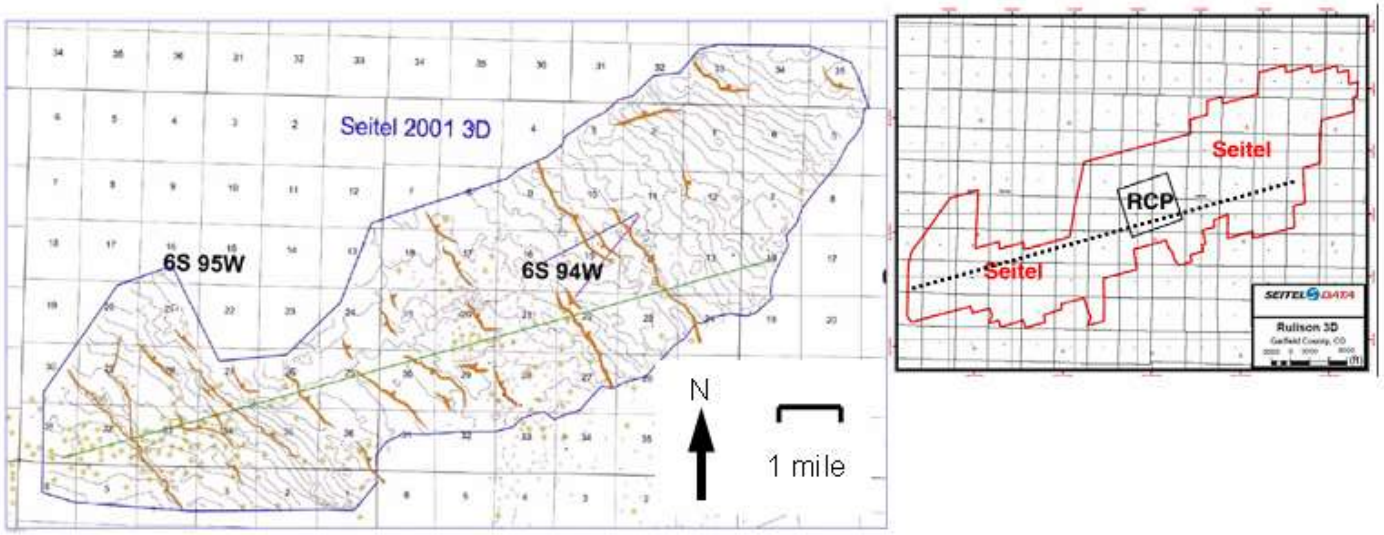

Figure. 7.32. Orientation of the fault surfaces after Cummella and Ostby (2003) on the time-structure map of the Rollins Sandstone. Faults strike N30^{o}W and have dip magnitude of 30-60^{o}. This orientation corresponds with one class of the faults interpreted in this study from borehole images. The right part of the figure shows the position of the RCP survey inside the Seitel survey.

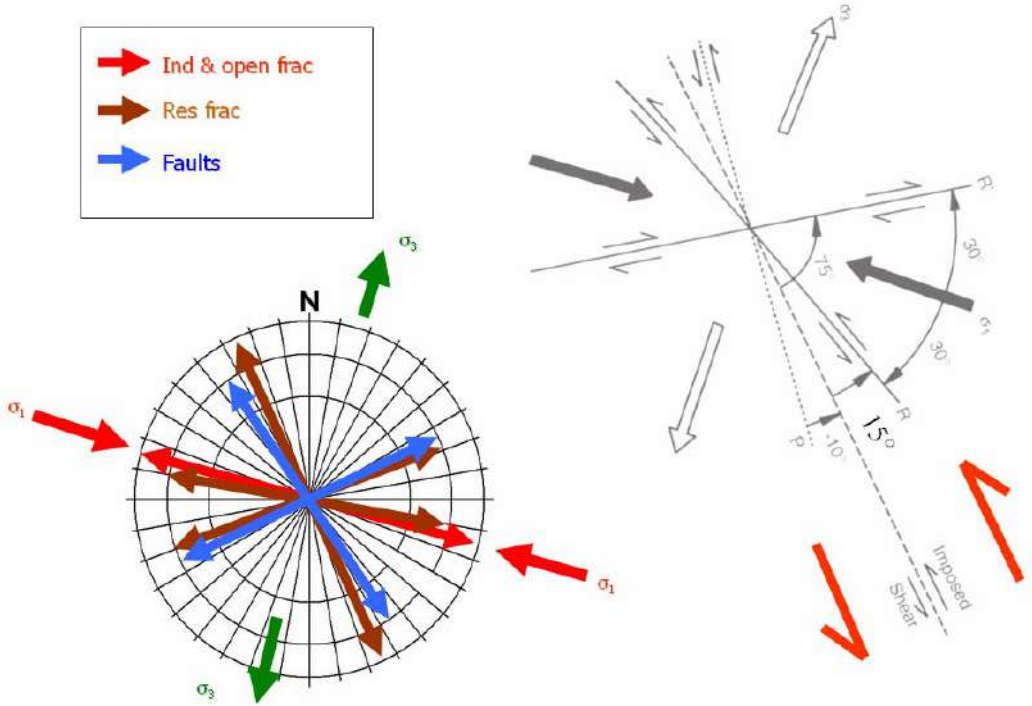

Figure 7.33. Left-lateral shear model. The arrows in the sketch represent the mean of interpreted structural features. Present-day stress orientation shows the same orientation of the stress axes as the proposed model (extension of the Piceance basin). Abbreviations: Ind frac=drilling induced fractures, Res frac= natural resistive fractures, and Open frac = natural open fractures.

orientation. Faults and two sets of resistive fractures could be explained as Riedel conjugate shear fractures.

Furthermore, the fracture orientations on small rock samples (Gomez et al. 2003) exhibit the same patterns. They also show a dominant west-northwest-trending set with subsidiary northwestward and northeastward fracture sets. The kinematic model on different scales of investigation is coherent.

The orientation of the fractures and faults displayed in Figure 7.33 is also consistent with the findings of Kuuskraa et al. (1997). They noticed a series of N30W and N60E fractures associated with larger-scale faults, joints, and fractures in Rulison field.

CHAPTER 8

INTEGRATION OF GEOLOGIC, SEISMIC AND PRODUCTION DATA

Faults and fractures have been proven to be one of the main controls on production in tight-gas sandstone reservoirs like Rulison. In order to optimize future development of the field, it is important to predict the location of the faulted and intensively fractured zones. The type of survey which can forecast those zones is multicomponent seismic characterization. Because structural features in these types of reservoirs are nearly undetectable with conventional p-wave seismic, multi-component seismic data has been acquired.

An unfortunate aspect of any seismic survey is that different geologic phenomena can have the same signature in the acquired data. For example, faults and lithology changes can have the same expression in the seismic data. For the purpose of increasing the level of confidence in the seismic interpretation, structures interpreted in the image logs were compared with multi-component data. The preliminary seismic interpretation by RCP student Elizabeth LaBarre (M.S. thesis, in progress) was used as the basis for the discussion in this chapter.

8.1. Methods

Figure 8.1 shows the fold in the area of the seismic data. This also shows why only the results from the RWF 542-20 image log were compared with the seismic data. The wells RWF 523-20 and RMV 60-17 are located in the low-fold seismic area. The Halliburton report does not document any faults for the RWF 441-20 well.

LaBarre (2006) described the seismic processing methods: "The 2003 post-stack migrated compressional (PP), fast shear (S11), and slow shear (S22) volumes were used. These volumes were chosen because they are the baseline survey volumes. The first step in this interpretation was to convert all of the volumes to depth so that all of the volumes could be analyzed together. Then a coherency type algorithm was run on the volumes."

8.2. Results

Figures 8.2 to 8.8 show derived maps and cross sections at different depth levels in the reservoir in the vicinity of the RWF 542-20 well. Only the depth slices, in which linear features are traceable, are shown. The linear features were interpreted as possible faults. Notice that the same linear features appear in different depth slices. This increases the confidence that these are throughgoing faults. The geometrical components such as

depth and strike of the image-log faults were compared with corresponding characteristics of seismic faults.

Depth slices below and above the Cameo horizon (Figures 8.2 to 8.6) show a possible fault. The succession starts 946 ft below the Cameo horizon encountered in RWF 542-20 well, and it ends up at 150 ft above the mentioned horizon. In a depth interval of approximately 1100 ft, it is possible to interpret a linear feature as a possible fault. The fault does not show dip. It is nearly vertical. The strike of the feature matches the fault strike mapped by Cumella and Ostby (2003) of roughly N30^{o}W.

In a vertical sense, it is not obvious or easy to interpret the same structural feature. By looking through the full survey it was possible to trace portions of the fault. Only the best examples are shown in Figures 8.7 and 8.8. An inline view of the slow-shear (S22) similarity volume through the RWF 542-20 well (Figure 8.7) shows anomalies at the locations of the faults picked in the image log. This might be an indicator of a structurally altered zone or a zone of enhanced permeability.

8.3. Discussion

The faults interpreted in the borehole images may not be the same features seen in the seismic data. Most likely they are sub-seismic features associated with the larger-scale fault. In my opinion, only the strikes and dips of the structural features on different

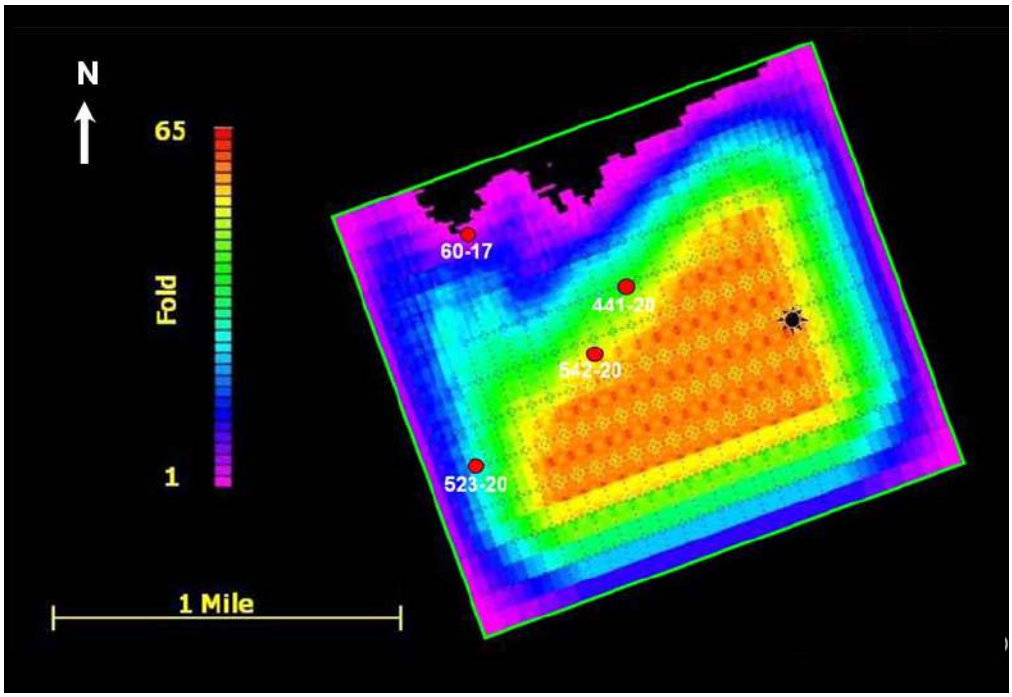

Figure 8.1. Map of the shear seismic usable fold with the locations of the image log wells (red dots). Well RMV 60-17 and RWF 523-20 are not included in this comparison because they are both located in areas of the survey with low usable fold. Only the RWF 542-20 well is included in the comparison in this chapter. Modified after Jansen (2005).

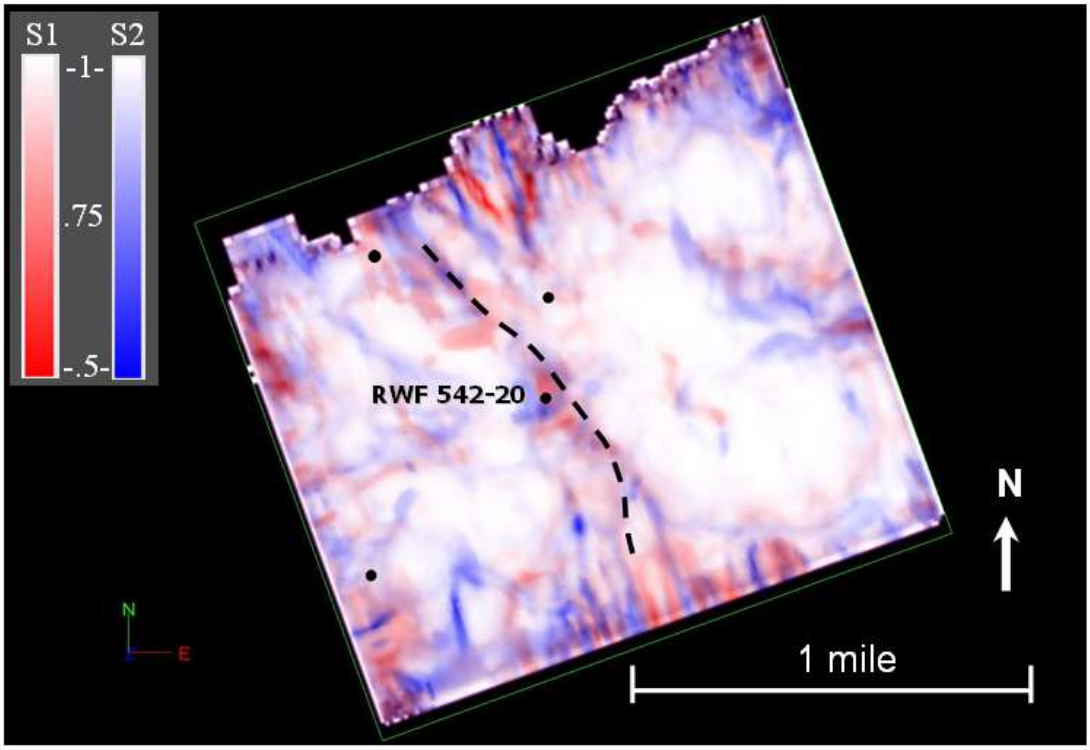

Figure 8.2. Co-rendered S11 (pure fast shear, in red) and S22 (pure slow shear, in blue) seismic trace similarity depth slice at 7946 ft of measured depth. Black dots represent the location of four imaged wells. The depth is 946 ft below the Cameo horizon. Use Figure 8.7 as a reference. Color bar: "1" means that there are no trace-to-trace differences. ".5" means that there is a 50% change in the wavelet shape from one trace to the next. Linear feature (possible fault) is interpreted with the dashed line. Interpreted from LaBarre (2006).

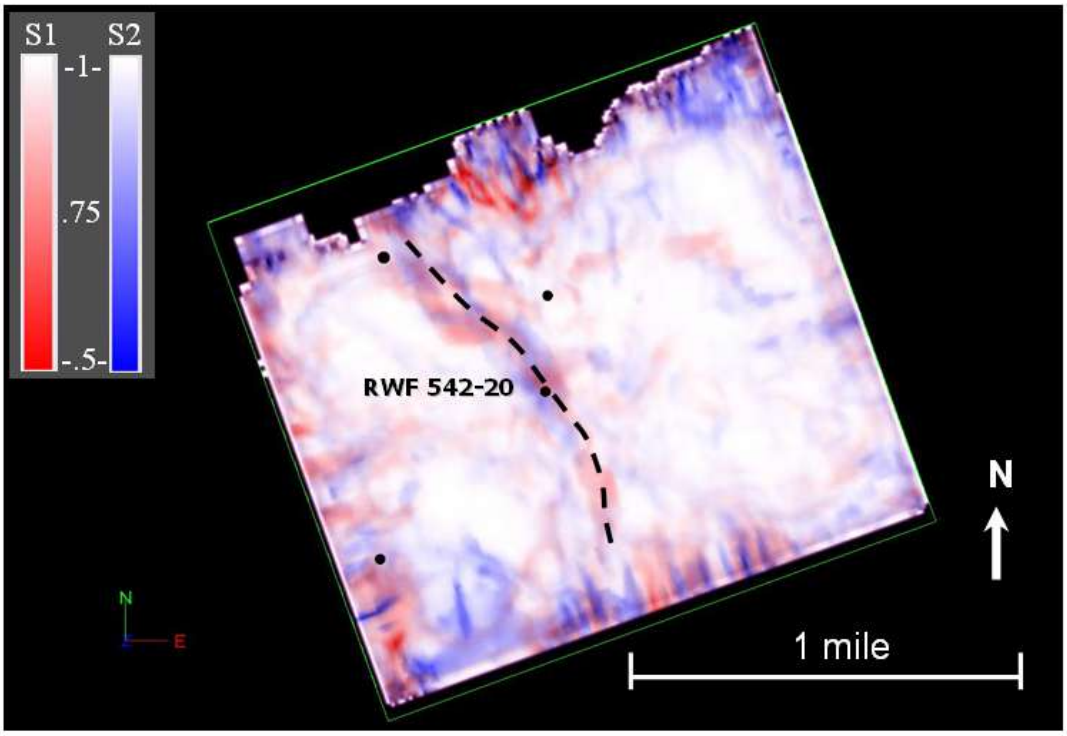

Figure 8.3. Co-rendered S11 (pure fast shear, in red) and S22 (pure slow shear, in blue) seismic trace similarity depth slice at 7755 ft of measured depth. The depth is 755 ft below the Cameo horizon. Use Figure 8.7 as a reference. Color bar: "1" means that there are no trace-to-trace differences. ".5" means that there is a 50% change in the wavelet shape from one trace to the next. Linear feature (possible fault) is interpreted with the dashed line. Interpreted from LaBarre (2006).

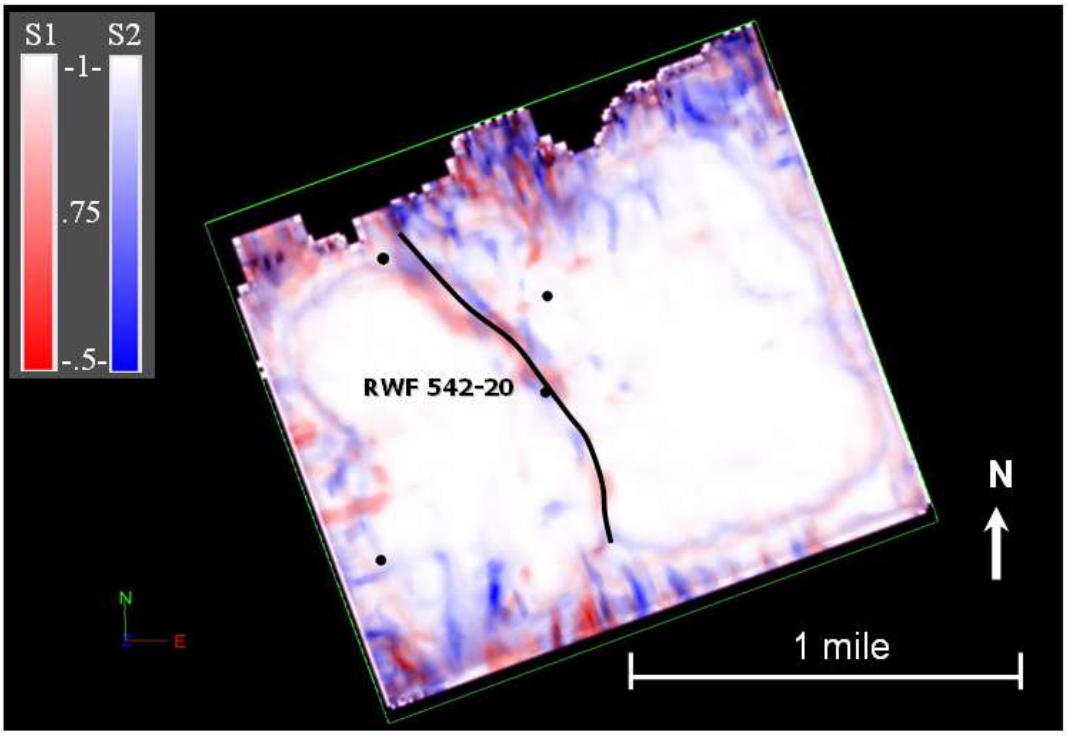

Figure 8.4. Co-rendered S11 (pure fast shear, in red) and S22 (pure slow shear, in blue) seismic trace similarity depth slice at 7325 ft of measured depth. The depth is 325 ft below the Cameo horizon. Use Figure 8.7 as a reference. Color bar: "1" means that there are no trace-to-trace differences. ".5" means that there is a 50% change in the wavelet shape from one trace to the next. Linear feature (possible fault) is interpreted with the solid line. Interpreted from LaBarre (2006).

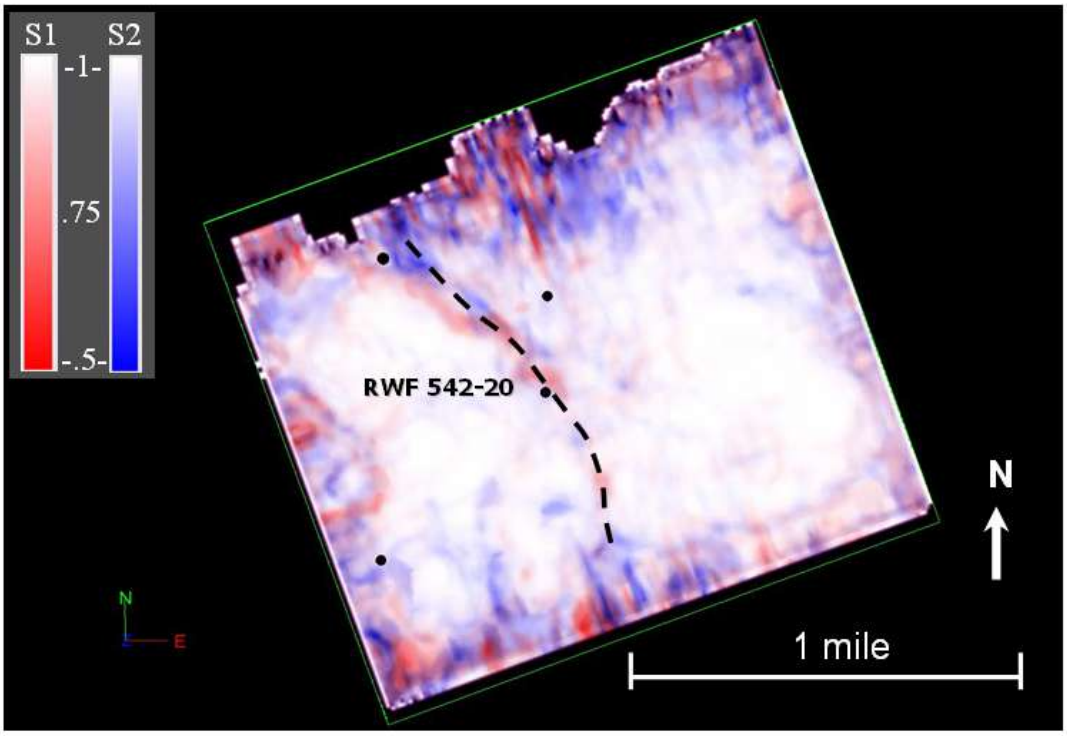

Figure 8.5. Co-rendered S11 (pure fast shear, in red) and S22 (pure slow shear, in blue) seismic trace similarity depth slice at 7080 ft of measured depth. The depth is 85 ft below the Cameo horizon. Use Figure 8.7 as a reference. Color bar: "1" means that there are no trace-to-trace differences. ".5" means that there is a 50% change in the wavelet shape from one trace to the next. Linear feature (possible fault) is interpreted with the dashed line. Interpreted from LaBarre (2006).

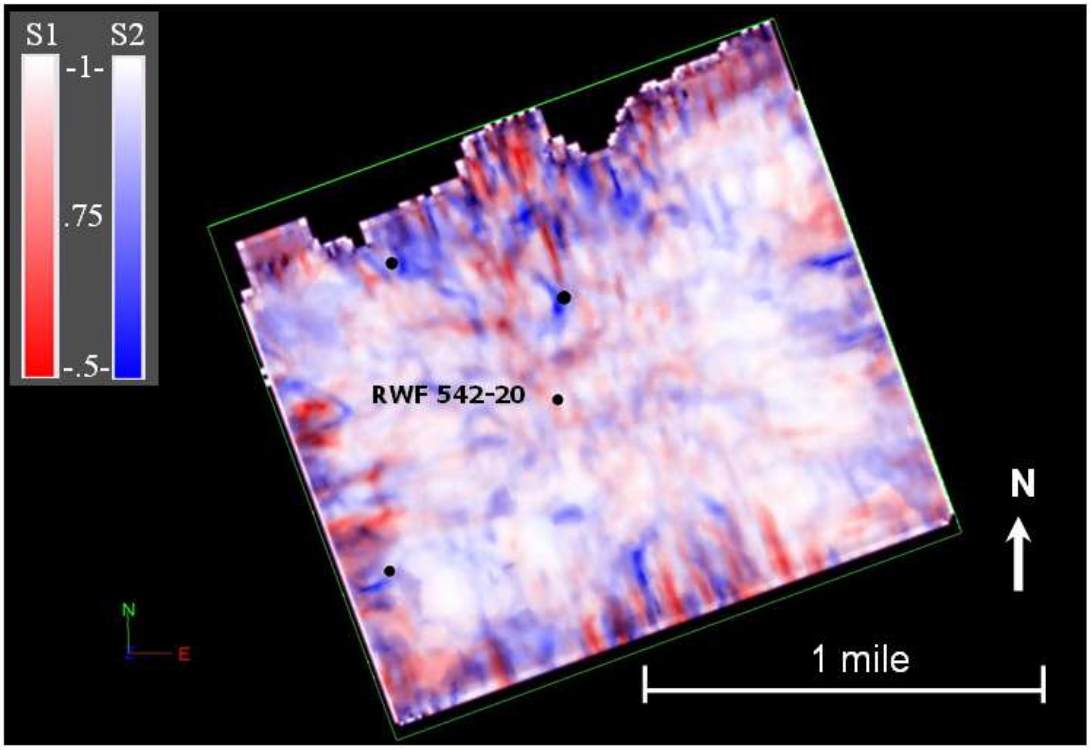

Figure 8.6. Co-rendered S11 (pure fast shear, in red) and S22 (pure slow shear, in blue) seismic trace similarity depth slice at 6850 ft of measured depth. The depth is 150 ft above the Cameo horizon. Use Figure 8.7 as a reference. Color bar: "1" means that there are no trace-to-trace differences. ".5" means that there is a 50% change in the wavelet shape from one trace to the next. Linear feature (possible fault) shown in previous figures is no longer traceable. Interpreted from LaBarre (2006).

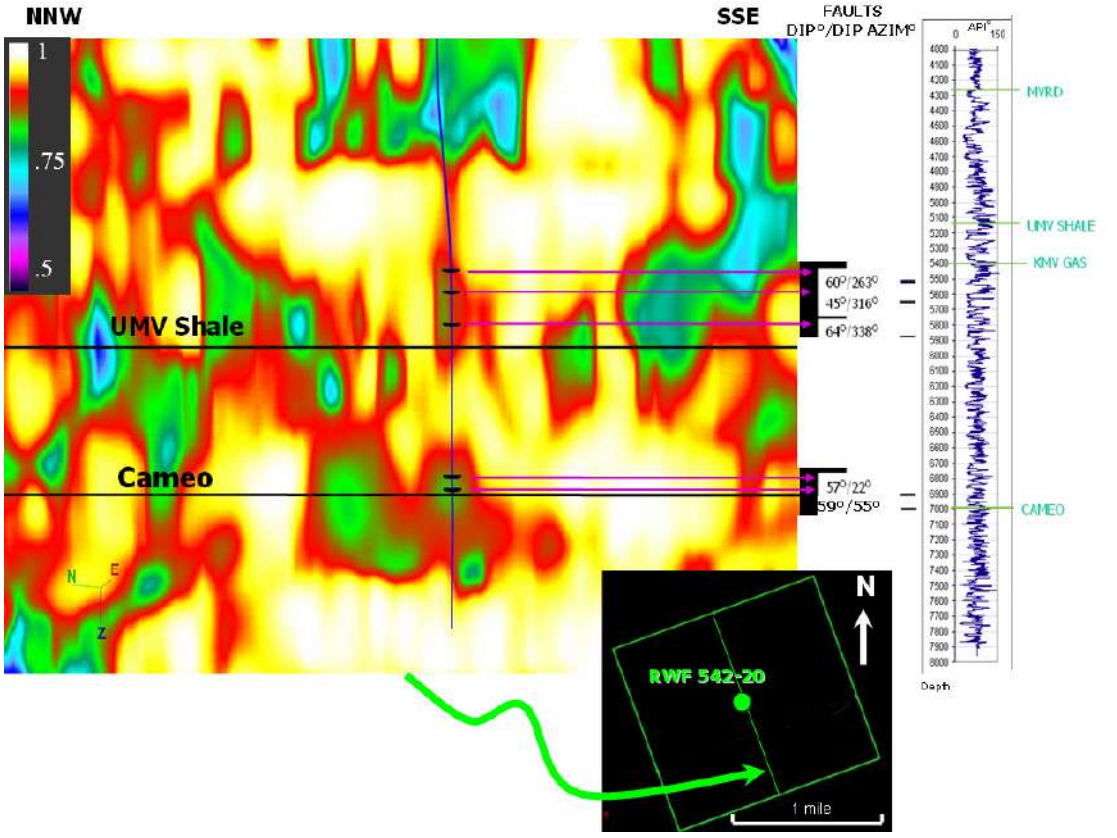

Figure 8.7. Depth-converted inline of the slow shear (S22) similarity volume through the RWF 542-20 well showing similarity anomalies at the locations of the faults picked in the image log from the RWF 542-20 well. On the right side, note the GR log of the imaged interval with depths, dip, and dip azimuth for the 5 interpreted faults. Color bar: "1" means that there are no trace-to-trace differences. ".5" means that there is a 50% change in the wavelet shape from one trace to the next. Notice the differences at depths of image log interpreted faults. Modified from LaBarre (2006).

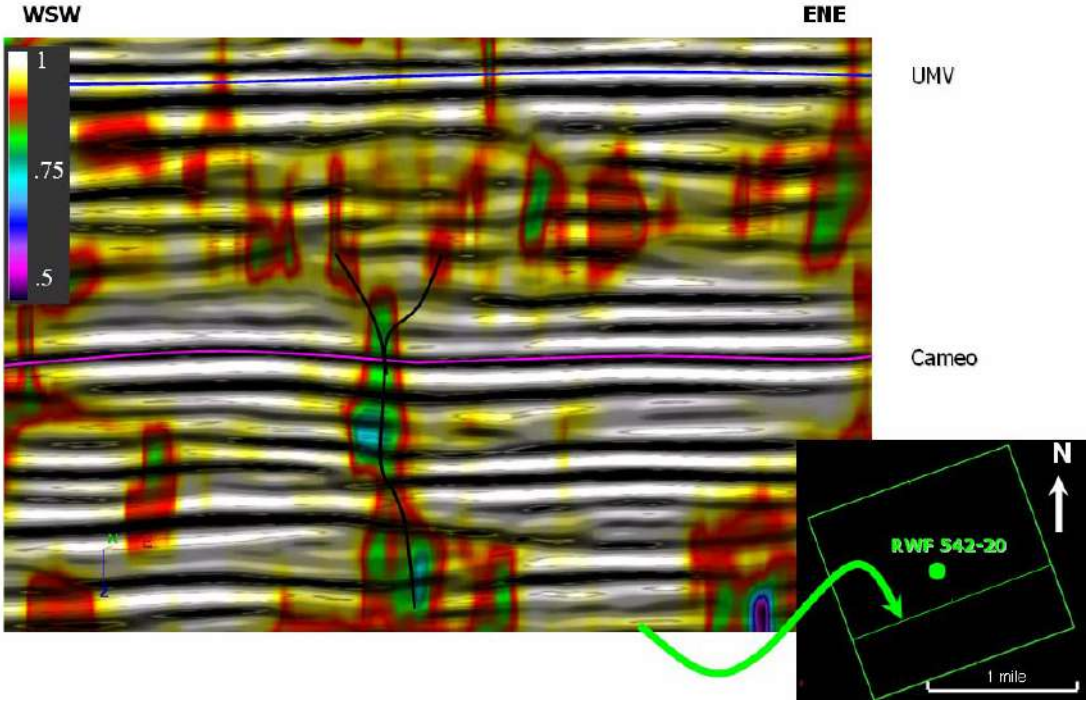

Figure 8.8. Depth-converted seismic section with the Cameo (pink) & UMV (light blue) horizons. Cross line shows fast shear (S11) basic amplitude seismic (black & white) co-rendered with the similarity (coherency) section (rainbow colors). Color bar: "1" means that there are no trace-to-trace differences. ".5" means that there is a 50% change in the wavelet shape from one trace to the next. The interpreted fault (black solid line) has a low similarity value at and below the Cameo level. The fault is probably splaying up into the Williams Fork reservoir. Cross line is in the vicinity of the RWF 542-20 well (approximately 300 ft to the southeast). Interpreted from LaBarre (2006).

scales of investigation are comparable. The lowermost image log interpreted fault (dip=59^{o}, strike=325^{o}) shows the same strike as the seismic-interpreted fault and it matches the geometrical characteristics interpreted by Cumella and Ostby (2003).

The best candidates that could be noticed on the seismic scale are two fault zones in well RWF 523-20 with corresponding measured depths of 6850 ft and 7400 ft. Unfortunately, this portion of the RCP survey is located at the edge of the survey in the low fold area. This work is still in progress.

Figure 8.9 shows the production data inside of the RCP survey area. The best wells (red dots) are regularly spaced away from the interpreted fault. The wells located directly on top of the fault have relatively lower production because of two possible reasons. First, wells might penetrate relatively small reservoir compartments, which quickly drained the gas. Second, the zones might have excessive permeability, which causes partial leakage of gas and relatively inferior gas production.

Another possibility for potential gas-prone areas in relation to the faults exists. Harding (1974) described that en-echelon anticlines as the basic trap associated with shear faults (Figure 8.10). If we assume that the interpreted seismic fault is a left-lateral shear structure, then potential sweet spots for drilling might be located in folded areas which would correspond to the location of the en-echelon folds. Tom Davis (personal communication) emphasized the existence of such structures in the wider area of Rulison field. He also noted that faults with relatively shallow dips (Figures 7.29, 7.30, and 7.31)

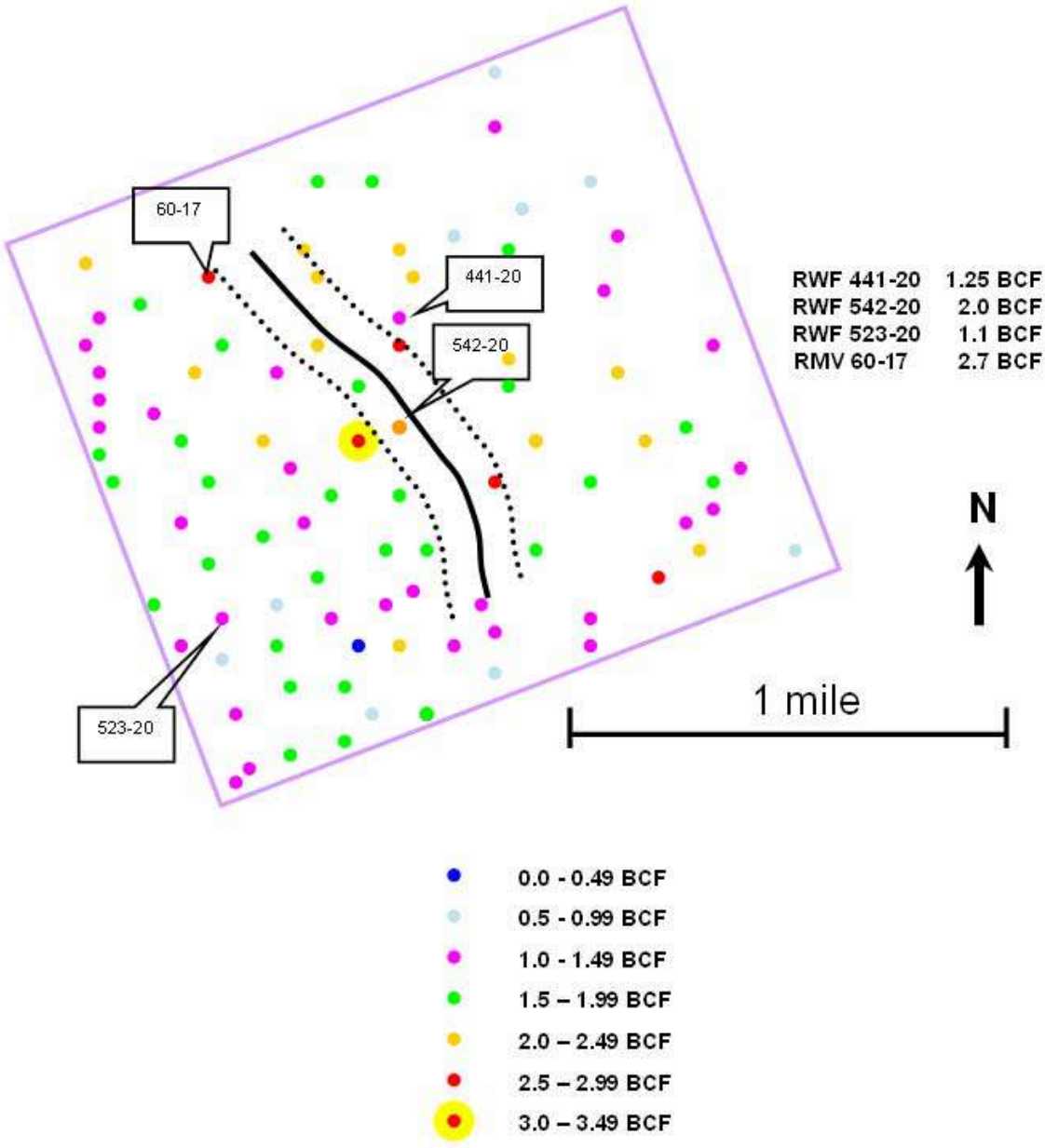

Figure 8.9. Estimated Ultimate Recovery (EUR) map of the wells inside of the RCP survey area. Note that the best producing wells are located at least 600 ft (margin of the dotted lines) from the interpreted fault.

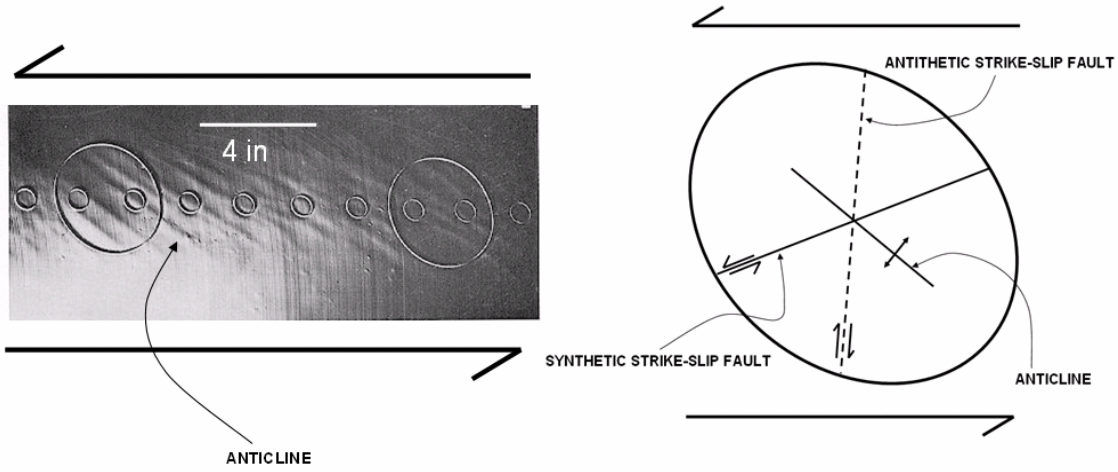

Figure 8.10. En echelon anticlines associated with left-lateral shear faults. The anticlines are the basic traps for the hydrocarbons. Left: Clay model of the parallel left-lateral shear fault. Right: Anticline that can result from the left lateral shear deformation shown schematically within the strain ellipse. Modified after Harding (1973).

tend to occur in the Cameo coal interval. This may be related to increased bedding-plane slip in this interval.

Furthermore, the RMV 60-17 and RWF 542-20 wells, as the relatively better producers of the image-log wells, show two sets of resistive fractures striking 65^{o} and 340^{o}, respectively (Figures 5.5 and 5.6). The RWF 523-20 well has the lowest production, and just one resistive fracture interpreted. The mud weight for all three wells has approximately similar values (Figures 7.29 to 7.31). One interesting fact is that the well with the lowest EUR (RWF 523-20) does not show the presence of gas seeps. Also, this well has 2 fault zones, and may be the most heavily faulted well.

The potential sweet spots for drilling might be located at same distance from seismic interpreted faults (approximately 600 ft, 200m). Also, the multicomponent seismic survey should show polarization in N30^{o}W or N65^{o}E directions due to the sub-seismic scale faults and associated fractures which correspond to the primary and secondary production trends.

CHAPTER 9

CONCLUSIONS AND RECOMMENDATIONS

9.1. Conclusions

The purpose of this study was to interpret structural and stratigraphic features in 3 borehole-image logs in the lower Williams Fork Formation at Rulison field, Piceance basin, Colorado, and to compare those results with seismic data. The study has reached the following conclusions:

1) The present-day in situ stress orientation (SHmax) determined from the borehole breakouts and drilling induced fractures at Rulison field is N70^{o}W with local variations.

2) Drilling induced fractures have the same orientation as natural open fractures. The open natural fractures are solely developed in the sandstones and this was the main criterion for their recognition. The dip of the open fractures averages about 75^{o}.

3) Two sets of resistive fractures are oriented N30^{o}W and N60^{o}E. The third, least numerous set of resistive fractures, is parallel to the orientation of SHmax, suggesting

that it was created in the same stress regime as the drilling induced or natural open fractures. Average dip of resistive fractures is 35^{o}.

4) Most of the imaged intervals in 2 out of 3 wells show the presence of gas seeps. There was no definitive relationship between faults, fractures, sandstone beds, and gas seeps. Higher mud weights in one well correspond to reduced gas-seep density. The quantity of gas seeps is a function of mud weight. Gas-seep interpretation has to be approached with caution, and used as a qualitative indicator of gas presence.

5) Two fault zones and 18 faults were interpreted in both dip-domain analyses and image logs for wells RWF 542-20, RWF 523-20 and RMV 60-17. Two sets of resistive fractures parallel the strike of the faults interpreted. This suggests that faulted zones of enhanced permeability are accompanied by fractures of the same orientation. All of the orientations of the structural elements such as stress, fractures, and faults show a good match with a left-lateral kinematic model. Faults and two sets of resistive fractures could be explained as Riedel conjugate-shear fractures.

6) In the vicinity of the RWF 542-20 well, there is a fault interpreted in seismic data. A succession of depth slices used in the interpretation starts 946 ft below the Cameo horizon encountered in the RWF 542-20 well, and it ends 150 ft above the mentioned horizon. The fault has a strike of $N30^{o}W$ and is nearly vertical. The slow-shear (S22) similarity volume through the RWF 542-20 well shows anomalies at the locations of the faults picked in the image log. This might be an indicator of a structurally altered zone or a zone of enhanced permeability. The seismic-scale fault is not visible in the image log.

Only the strikes and dips of structural features on different scales of investigation are comparable.

7) The best wells, in terms of estimated ultimate recovery (EUR), are regularly spaced away from the seismic-interpreted fault (approximately 600 ft, 200m). The wells located directly on top of the fault have relatively lower production because of two possible reasons. First, wells might penetrate relatively small reservoir compartments, which quickly drained the gas. Second, the zones might have excessive permeability, which causes partial leakage of gas and relatively inferior gas production. Furthermore, the RMV 60-17 and RWF 542-20 wells, as the relatively better producers of the image-log wells, show two sets of resistive fractures striking 65^{o} and 340^{o}, respectively. The RWF 523-20 well has the lowest EUR, absence of gas seeps, 2 fault zones and just one resistive fracture interpreted.

9.2. Recommendations

Work within the Williams Fork Formation on borehole images and seismic data will continue. The following recommendations will assist future workers in the assessment of the direction and focus of these efforts, and provide a basis for extending the findings of this study.

1) The potential sweet spots for drilling might be located in proximity of seismic interpreted faults (approximately 600 ft, 200m). The multicomponent seismic survey should show polarization in N30^{o}W or N65^{o}E directions due to the existence of sub-seismic scale faults and associated fractures which correspond to the primary and secondary production trends. Also, one has to bear in mind that the zones of enhanced permeability could serve both as zones for accumulation of gas, and escape. Furthermore, diagenessis must not be neglected. It is documented in this work that some of the structural features are mineral filled.

2) Run production logs. The gas-seep interpretation does not show us where gas is coming from and how it relates to faults and fractures.

3) Better calibrate seismic surveys by decreasing the scale of investigation. It is likely that critical processes are occuring on the subseismic level. Try to understand the play between migration (fractures, faults and their diagenesis) and fluid accumulation on a smaller scale by examining cores, and thin sections.

REFERENCES

Allen, D. T. F. Barber, C. Flaum, J.Hemingway, B. Anderson, S. des Ligneris, R. Everett, and C. Morris, 1988, Advances in high resolution logging: The Technical Review, v. 36, No. 2, p. 4-14.

Cole, R., and S. Cumella, 2003, Sand-body architecture in the Lower Williams Fork Formation, Coal Canyon, Colorado: The Mountain Geologist, v. 42, p. 85-107.

Cumella, S. P. and D. B. Ostby, 2003, Geology of the basin-centered gas accumulation, Piceance Basin, Colorado, *in* K. M. Peterson, T. M. Olsen, and D. S. Anderson, eds., Piceance Basin 2003 guidebook: Rocky Mountain Association of Geologists, p. 171 - 193.

Cumella, S. P., 2006, Overview of a giant basin-centered gas accumulation, Mesaverde Group, Piceance Basin, Colorado, *in* S.A. Sonnenberg, and E.D. Dolly, eds., The Mountain Geologist, A special theme issue on Rocky Mountain gas reservoirs revisited. Rocky Mountain Association of Geologists. v.43, No.3, p. 219-224.

Ellison, A. I., 2004, Numerical modeling of heterogeneity withina fluvial point-bar deposit using outcrop and lidar data: Williams Fork Formation, Piceance Basin, Colorado: Unpublished MS Thesis, Boulder, Colorado, University of Colorado, 235 p.

Gill, J. R., and W. A. Cobban, 1973, Stratigraphy and geologic history of the Montana Group and equivalent rocks, Montana, Wyoming, and North and South Dakota: U.S. Geological Survey Professional Paper 776, 37 p.

Gomez, L., J. F. W. Gale, S. E. Laubach, and S. Cumella, 2003, Quantifying fracture intensity: An example from the Piceance basin, *in* K.M. Peterson, T. M. Olsen, and D.S. Anderson, eds., Piceance basin 2003 guidebook: Rocky Mountain Association of Geologists, p. 96 -113.

Green, C., 2006, Hydraulic fracture model sensitivity analyses of massively stacked lenticular reservoirs in the Mesaverde formation, southern Piceance Basin, Colorado: Unpublished M.S. Thesis, Colorado School of Mines, Golden, Colorado, 204 p.

Grout, M. A., and E. R. Verbeek, 1992, Fracture history of the Divide Creek and Wolf Creek anticlines and its relation to Laramide basin-margin tectonism, southern Piceance Basin, northwestern Colorado: United States Geological Survey Bulletin 1787-Z, 32 p.

Harding, T. P., 1973, Petroleum traps associated with wrench faults: AAPG Bulletin, v. 58, p. 1290-1304.

Hettinger, R. D., and M. A. Kirschbaum, 2002, Stratigraphy of the Upper Cretaceous Mancos shale (upper part) and Mesaverde Group in the southern part of the Uinta and Piceance Basins, Utah and Colorado: United States Geological Survey Investigations Series I-2764, 21 p.

Higgins, S., 2006, Geomechanical modeling as a reservoir characterization tool at Rulison field, Piceance Basin, Colorado: Unpublished M.S. Thesis, Colorado School of Mines, Golden, Colorado, 135 p.

Hoak, T. E. and Klawitter, A. L., 1997, Prediction of fractured reservoir production trends and compartmentalization using an integrated analysis of basement structures in the Piceance Basin, western Colorado, *in* T. E. Hoak, A. L. Klawitter, and P. K. Blomquist, eds., Fractured reservoirs: characterization and modeling: Rocky Mountain Association of Geologists Guidebook, p. 67 - 102.

Höcker, C., K.M. Eastwood, J.C. Herweijer, and J.T. Adams, 1990, Use of dipmeter data in clastic sedimentological studies: AAPG Bulletin, v. 74, p. 105-118.

Hurley, N. F., 1994, Recognition of faults, unconformities, and sequence boundaries using cumulative dip plots: AAPG Bulletin, v. 78, p. 1173-1185.

Hurley, N.F., 2004, Borehole images, *in* G. Asquith and D. Krygowski, Basic well log analysis, 2nd Edition: AAPG Methods in Exploration 16, p. 151-163.

Jansen, K.J., 2005, Seismic investigation of wrench faulting and fracturing at Rulison field, Colorado: Unpublished M.S. Thesis, Colorado School of Mines, Golden, Colorado, 135 p.

Johnson, R. C. and T. M. Finn, 1986, Cretaceous through Holocene history of the Douglas Creek Arch, Colorado and Utah, *in* D. S. Stone and K. S. Johnson, eds., New interpretations of northwest Colorado geology: Rocky Mountain Association of Geologists, p. 77-95.

Johnson, R. C., 1989, Geologic history and hydrocarbon potential of Late Cretaceous-age, low-permeability reservoirs, Piceance Basin, western Colorado: United States Geological Survey Bulletin 1787-E, 51 p.

Keighley, D., 2006, M.S, P-wave time-lapse seismic data interpretation at Rulison field, Piceance Basin, Colorado: Unpublished M.S. Thesis, Colorado School of Mines, Golden, Colorado, 111 p.

Knight, C. N., 1999, Structural and stratigraphic controls on Mesaverde reservoir performance: North La Barge field, Sublette county, Wyoming: Unpublished PhD Dissertation, Colorado School of Mines, Golden, Colorado, 217 p.

Koepsell, R., S. P. Cumella and D. Uhl, 2003, Applications of borehole images in the Piceance Basin *in* K. M. Peterson, T. M. Olsen, and D. S. Anderson, eds., Piceance Basin 2003 guidebook: Rocky Mountain Association of Geologists, p. 233 - 251.

Kusuma, M., 2005, Analysis of time-lapse P-wave seismic data from Rulison Field, Colorado: Unpublished M.S. Thesis, Colorado School of Mines, Golden, Colorado, 194 p.

Kuuskraa, V. A., T. Barrett, R. Mueller, and J. Hansen, 1997, Reservoir characterization for development of Mesaverde Group sandstones of the Piceance Basin, Colorado, *in* E. B. Coalson, J. C. Osmond, and E. T. Williams, eds., Innovative applications of petroleum technology guidebook: Rocky Mountain Association of Geologists, p. 61 - 72.

Kuuskraa, V.A., D. Campagna, I. Drayton, F. Joyce, G. Koperna, J. Kuuskraa, and M. Marquis, 1999, Portfolio of emerging natural gas resources, Rocky Mountain Basins, Section 2. Piceance Basin: Advanced Resources International, Inc., 45 p.

LaBarre, E., 2006, Fault and fracture characterization from multicomponent seismic data, *in* Reservoir Characterization Project Spring Meeting Report, p. 57-66.

Law, B. E., 2002, Basin-centered gas systems: AAPG Bulletin, v. 86, p. 1891-1919.

Lorenz, J. C., and S. J. Finley, 1991, Regional fractures II: Fracturing of Mesaverde reservoirs in the Piceance basin, Colorado: AAPG Bulletin, v. 75, p. 1738 – 1757.

Lorenz, J. C., 2003, Fracture systems in the Piceance basin, overview and comparison with fractures in the San Juan and Green River basin, *in* K.M. Peterson, T. M. Olsen, and D.S. Anderson, eds., Piceance basin 2003 guidebook: Rocky Mountain Association of Geologists, p. 75 -94.

Lorenz, J. C., D. M. Heinze, J. A. Clark, and C. A. Searls, 1985, Determination of widths of meander-belt sandstone reservoirs from vertical downhole data, Mesaverde group, Piceance Creek Basin, Colorado: AAPG Bulletin, v. 69, p. 710-721.

Minton, G.E., 2002, Subsurface study of the Lewis Shale in Southern Washakie and Sand Wash Basin using borehole image, core, well log, and seismic data: Unpublished M.S. Thesis, Colorado School of Mines, Golden, Colorado, 219 p.

Panjaitan. H., 2006, Sand-body dimensions in outcrop and subsurface, Lower Williams Fork Formation, Piceance basin, Colorado: Unpublished MS Thesis, Colorado School of Mines, Golden, Colorado, 170 p.

Patterson, P. E., K. Kronmueller, and T. D. Davies, 2003, Sequence stratigraphy of the Mesaverde Group and Ohio Creek Conglomerate, northern Piceance Basin, Colorado, *in* K. M. Peterson, T. M. Olsen, and D. S. Anderson, eds., Piceance Basin 2003 guidebook: Rocky Mountain Association of Geologists, p. 115 - 129.

Payne, D. F., K. Tuncay, A. Park, J. B. Comer, and P. Ortoleva, 2000, A reaction transport-mechanical approach to modeling the interrelationships among gas generation, overpressuring, and fracturing: Implications for the Upper Cretaceous natural gas reservoirs of the Piceance Basin, Colorado: AAPG Bulletin, v. 84, p. 545 - 565.

Potential Gas Committee, 2003, Potential supply of natural gas in the United States: Report of the Potential Gas Committee (Dec. 31, 2002): Potential Gas Agency, Colorado School of Mines, Golden, CO, April 2003, 316 p. with accompanying CD-rom.

Reinecker, J., O. Heidbach, M. Tingay, B. Sperner, and B. Müller, 2005, The 2005 release of the World Stress Map (available online at www.world-stress-map.org).

Rider, M. H., 1996, The geologic interpretation of well logs: Gulf Publications, Houston, Texas, 2nd Edition, 280 p.

Rojas, E., 2005, Elastic rock properties of tight gas sandstones for reservoir characterization at Rulison Field, Colorado: Unpublished M.S. Thesis, Colorado School of Mines, Golden, Colorado, 144 p.

Rumon, M. D., 2006, Shear wave time-lapse seismic monitoring of a tight gas sandstone reservoir, Rulison Field, Colorado : Unpublished M.S. Thesis, Colorado School of Mines, Golden, Colorado, 140 p.

Spencer, C. W., 1989, Review of characteristics of low-permeability gas reservoirs in Western United States: AAPG Bulletin, v. 73, p. 613 - 629.

Springer, J., 1987, Stress orientations from wellbore breakouts in the Coalinga region: Tectonics, v. 6, p. 667-676.

Tweto, O., 1975, Laramide (the Cretaceous - early Tertiary) orogeny in southern Rocky Mountain, *in* Curtis B. F., ed., Cenozoic history of the southern Rocky Mountains: GSA Memoir 144, p. 1 - 44.

United States Geological Survey, 2003, Assessment of undiscovered oil and gas resources of the Uinta-Piceance Province of Utah and Colorado, United States Geological Survey Fact Sheet FS-157-02, 2 p.

Vargas, M. F., 2004, Characterization and modeling of fluvial sandstone distribution and static connectivity, Williams Fork Formation, Rulison field, Piceance Basin, Colorado: Unpublished MS Thesis, Department of Geological Sciences, University of Colorado, Boulder, Colorado, 136 p.

Yurewicz, D. A, K. M. Bohacs, J. D. Yeakel, and A. Kronmueller, 2003, Source rock analysis and hydrocarbon generation, Mesaverde Group and Mancos Shale, Northern Piceance Basin, Colorado, *in* K. M. Peterson, T. M. Olsen, and D.S. Anderson, eds., Piceance basin 2003 guidebook: Rocky Mountain Association of Geologists, p. 130-153.

Zheng, Z. J. Kemeny, and N. G. W. Cook, 1989, Analysis of borehole breakouts: Journal of Geophysical Research, v. 94, p. 7171-7182.